Polaronic Charge Carriers and their Optical Excitations in Insulating La_2CuO_{4+y}

by

Jens Petter Falck

M.Sc., Norwegian Institute of Technology (1987)

Submitted to the Department of Physics
in partial fulfillment of the requirements for the degree of

Doctor in Philosophy

at the

MASSACHUSETTS INSTITUTE OF TECHNOLOGY

June 1993

Author .....
Department of Physics
June 24, 1993

Certified by .....
Marc A. Kastner
Donner Professor of Science
Thesis Supervisor

Accepted by .....
George F. Koster
Chairman, Departmental Committee on Graduate Students

Polaronic Charge Carriers and their Optical Excitations in Insulating La_2CuO_{4+y}

by

Jens Petter Falck

Submitted to the Department of Physics
on June 24, 1993, in partial fulfillment of the
requirements for the degree of
Doctor in Philosophy

Abstract

The optical and infrared electronic excitations in undoped and lightly oxygen doped La_2CuO_{4+y} are studied by means of polarization and temperature dependent reflectivity and electroreflectance measurements. In particular, we demonstrate that both free and localized holes form large polarons.

The lowest energy electronic excitation in undoped La_2CuO_4 is the charge transfer excitation observed as a sharp peak in the imaginary part of the dielectric function $\epsilon_2(\omega)$ for light polarized parallel to the CuO_2 layers. A theory in which the final state consists of electron and hole polarons coupled to each other by a short range potential provides an excellent fit to the data at low temperatures and predicts the spectrum up to $\sim 400\,\mathrm{K}$ with no adjustable parameters[1].

Upon doping three electronic excitations appear within the charge transfer gap at 0.13, 0.5 and 1.5 eV, respectively. We show that spectral weight is transferred between free carrier conductivity and a photo-ionization band of impurity-bound carriers. The large difference between the optical 0.13 eV and thermal 0.035 eV ionization energy indicates that the impurity states are stabilized by a lattice distortion. We demonstrate that the line shape as well as the temperature dependence is consistent with absorption from polaronic impurities with parameters consistent with other experiments[2].

Electroreflectance spectra are measured in two different configurations. Depending on the electrode structure, the modulation results in addition of charge carriers or variation of the electric field in the space charge region. These two cases induce modulation of the mid-infrared absorption bands. By comparing the modulation data with reflectivity of doped and undoped La_2CuO_{4+y} we find that the 1.5 eV infrared

[1] J.P.Falck *et al.*, Phys.Rev.Lett. **69**, 1109 (1992)
[2] J.P.Falck *et al.*, Phys.Rev.B. **47**, (1993)

band responds to electric fields in ways consistent with a $d_{x^2-y^2} \rightarrow d_{xy}$ transition[3]. The energies and symmetries of the observed bands are in agreement with those of crystal-field excitations and magnon sidebands recently observed in a variety of undoped cuprates[4]

Thesis Supervisor: Marc A. Kastner
Title: Donner Professor of Science

[3]J.P.Falck *et al.*, Submitted to Phys.Rev.B
[4]J.D.Perkins *et al.*, Submitted to Phys,Rev.Lett.

Acknowledgments

When I entered MIT in August 1988 I wanted to be a solid state theorist. After five years in the making I now graduate as a solid state experimentalist. These five years have been filled with hard work and frustration but also joy and excitement. Needless to say, I have not been alone on the crooked path to graduation. The work of this thesis would not have been possible without contributions from many people. I am grateful to all of them.

It is a pleasure to thank my advisor Marc Kastner for superb guidance. Marc has always been available and shared his time with his students on almost a daily basis. His enthusiasm, physical intuition and high standards are all qualities from which I have benefitted immensely. In addition to Marc I have also profited from the guidance of Bob Birgeneau and lately, John Graybeal.

On the technical side I thank the members of the MIT Crystal Physics Laboratory, most especially Arlete Cassanho, for teaching me how to grow crystals. Thanks also to David Emin of Sandia National Laboratories for sharing his insights on the physics of polarons.

Most of my time I have spent with my fellow labmates. First of all, thanks to Norris Preyer and Chih-Yong Chen for introducing me to the lab and patiently helping me getting started; to John Scott-Thomas for introducing me to what ever existed of social life at MIT; to Udi Meirav for sharing his thoughts on wine and women. A special thanks to Ady Levy who thought me how to get the most done in the shortest amount of time while offending only a minimum number of people. Thanks also to

John Perkins for an exciting collaboration. Ethan Foxman has been my officemate since the very beginning and is my closest associate on the non-scientific aspects of MIT. I thank Ethan for his friendship. I must also mention Nathan and Paul Belk who by their very nature have made the daily routine even more enjoyable. As for the new generation of students in our group, Pam Blakeslee, David Abusch, and Nathan and Paul Belk, I wish you all the best of luck.

Some of the most pleasant memories from my years in Boston are associated with the social life I have been lucky enough to enjoy. Particularly, thanks to Gerd Fritsch, Håkon Lie, Bent Bakken, Per Lindell and Martha Corrente for their friendship.

Heartfelt thanks to my family, to my parents, my sister and brother for their support.

Most importantly, however, thanks to Bjørg Kim Frivold for her love and care during these most difficult years.

Contents

List of Figures

List of Tables

Chapter 1

Introduction

Seven years have past since the initial discovery of high temperature superconductivity[1]. An enormous amount of labour has gone toward investigating the superconducting cuprate materials, yet the materials are still surprisingly poorly understood. It is clear that as in the traditional BCS superconductors, the high T_c superconducting state is a pair condensate satisfying the pair wave-function description as established by flux quantization experiments[2]. These experiments show that the magnetic flux trapped in a high T_c superconducting ring is an integral multiple of the flux quantum $h\,c/2e$. The presence of the factor 2 in the denominator shows that the carriers are pairs. The pairing mechanism, however, is in all likelihood different. While BCS-type phonon mediated Cooper pairing is a time-retarded interaction which requires a superconducting state of s symmetry, the experimental situation seems to favor d symmetry[3]. Specifically, the magnetic penetration depth is found to vary linearly with temperature[4] consistent with predictions for electrons paired in a d wave. Direct observations of anisotropy in the superconducting gap is provided by angle-resolved photoemission[5]. A recent study shows nodes in the superconducting gap consistent with d-wave symmetry[6].

A superconducting state of d symmetry is favored by a large number of proposed pairing interactions. Before one can sort out the most important interactions one

probably needs to understand the rather unusual properties of the free quasi particle excitations of the normal state. Specifically, the resistivity increases linearly with temperature from just above the superconducting transition temperature to almost the melting temperature[7]. Moreover, the in-plane free carrier conductivity displays a strong frequency and temperature dependent effective mass and scattering rate[8, 9, 10]. Finally, the electronic excitations in the normal state are in effect two-dimensional. No low-energy electronic excitations are observed perpendicular to the CuO_2 planes before the system goes superconducting as clearly demonstrated by the dramatic onset of coherent charge-transport across the CuO_2 planes below T_c seen in far-infrared reflectivity spectra[11].

Presently, both the pairing mechanism as well as the nature of the normal state remains unresolved. The reason for this slow progress is mostly due to the complex nature of the copper oxides themselves. While the low-temperature BCS superconductors are conventional metals, the host materials for the high temperature superconductors are insulators due to strong electron-electron Coulomb repulsion. The localized electrons carry spin which are strongly coupled forming an antiferromagnetic ground state. Motion of oxygen ions give rise to large electric dipoles which couple electrostatically to added charge carriers. These an other properties of the undoped copper oxides may influence the nature of the quasi particles in the normal state as well as the superconductivity. We will in the following paragraphs introduce the insulating copper oxides and shortly discuss some of their most important properties. Specifically we will consider La_2CuO_4.

1.1 La_2CuO_{4+y} - a High-T_c Precursor

1.1.1 The Antiferromagnetic Charge-Transfer Insulator

In Fig. 1-1 we show the lamellar crystal structure of La_2CuO_4 with two-dimensional layers of CuO_2 separated by stabilizing units of LaO. The structural element common to all the superconducting copper oxides is the two-dimensional CuO_2 layer shown in detail in Fig. 1-2. The Cu ion in the layer form a square array with oxygen atoms midway between each pair of Cu atoms. The CuO_2 planes appear in both tetragonal and orthorhombic geometry. In the orthorhombic phase of $La_{2-x}Sr_xCuO_4$ the Cu-Cu spacings along $\hat{x}$ and $\hat{y}$ differ by 1.5% and the oxygen ions are slightly displaced normal to the planes. Whereas the CuO_2 layers are always the same in each of the high T_c compounds, the stabilizing unit is different for the different material. The main purpose of the stabilizing unit is to supply the CuO_2 planes with charge carriers. One of the benefits with studying La_2CuO_4 is that the stabilizing unit is one of the simplest among the high-T_c materials.

Before we can discuss the electronic structure we must know the formal charge on each ion. Lanthanum has three weakly bound valence electrons and prefers valence La^{+3} with a xenon-like electronic configuration. Oxygen has electron configuration $2p^4$ and prefers valence O^{-2} and fully occupied $2p$ orbitals. For overall charge neutrality copper has valence Cu^{+2} and one hole in the $3d$ orbitals.

Since only the copper ions have valence charges, it is sufficient to only consider the properties of the CuO_2 planes in understanding the electronic excitation spectrum of insulating La_2CuO_4. The fundamental building block is the CuO_6 cluster with four in-plane and two apical oxygen ions positioned around the central Cu ion in a tetragonal symmetry as indicated in Fig. 1-1. The single copper hole can occupy one of the five different $3d$ levels. The degeneracy of the d states is lifted by electric fields from the neighboring oxygen and copper ions. For a crystal with tetragonal symmetry, the d states are split into four different energy levels. Only the d_{yz}, d_{zx} states remain

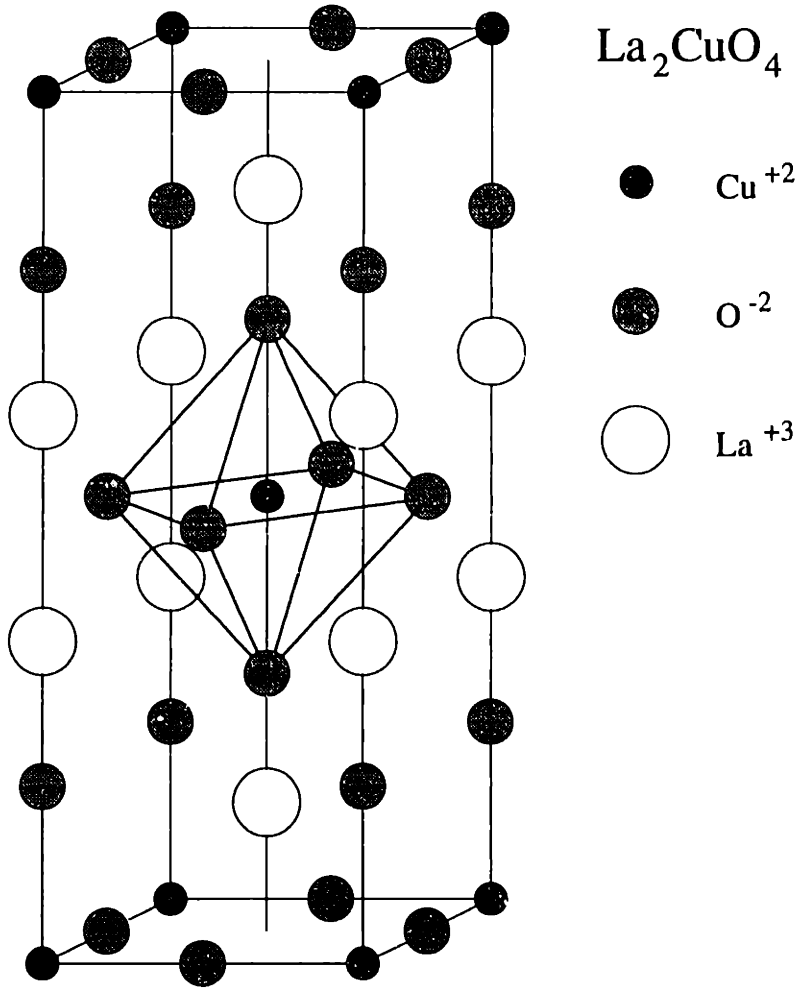

Figure 1-1: The unit cell of La_2CuO_4 in the tetragonal phase. Each copper ion is associated with a CuO_6 cluster identical to the one marked for the central copper ion.

degenerate. The $d_{x^2-y^2}$ orbital has the lowest hole energy due to the largest overlap with the negatively charged neighboring oxygen ions. In the level ordering favored by cluster calculations[12] the hole energy of the $d_{3z^2-r^2}$, d_{xy} and the d_{yz}, d_{zx} states are consecutively higher.

Since the O $2p$ orbitals are fully occupied, we can to zeroth order ignore the electrons on the oxygen ions in calculating the band structure. Within this approximation a tight binding calculation of the highest occupied band involves only $d_{x^2-y^2}$ orbitals on the copper ions. There is only one of these states per unit cell. Each orbital has two states due to spin degeneracy. Since there is only one electron per orbital, the

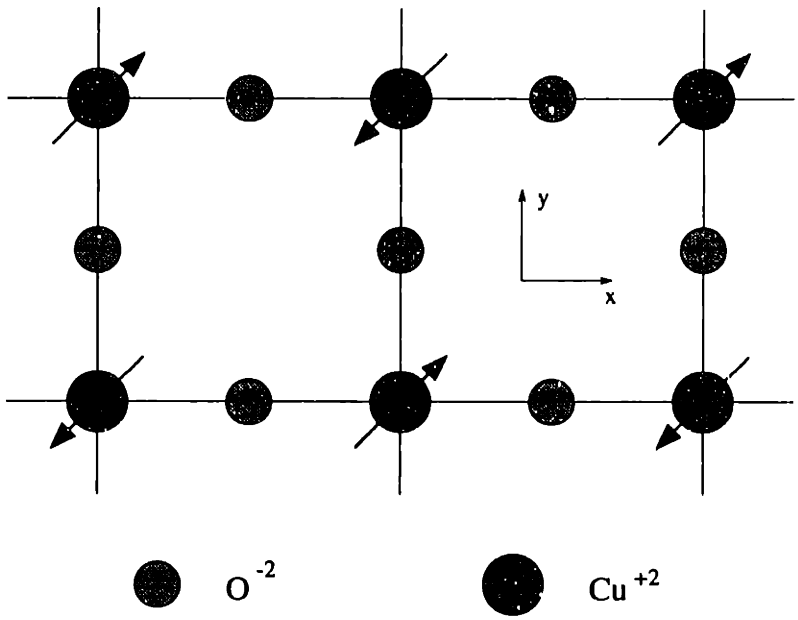

Figure 1-2: Crystal structure of the CuO_2 planes in the tetragonal phase. The arrows indicate the direction of the localized copper spins $S = \frac{1}{2}$ in the antiferromagnetic ground state.

band should be only half filled and La_2CuO_4 is predicted to be a metal. Indeed, traditional local-density band structure calculations predicts a metallic La_2CuO_4 ground state[13, 14]. Experimentally, however, by measuring the resistance, we know that undoped La_2CuO_4 is not a metal but an insulator.

This discrepancy between band theory and nature is not unique to the copper oxides. An insulating ground state is common among transition-metal oxides where the transition-metal ions have partially filled *d* shells and should according to band theory be metallic. The insulating state in these materials is understood as the result of correlated motion of electrons. These correlations, ignored in band theory, result from strong Coulomb repulsion between electrons. Such Coulomb interaction tends to keep the electrons localized on the transition-metal ions. This drive for localization is offset by the lowering of electronic energy by delocalizing the electrons throughout the crystal. This energy lowering comes both from a reduction of the kinetic energy because the electrons are less localized and from the increase in probability for find-

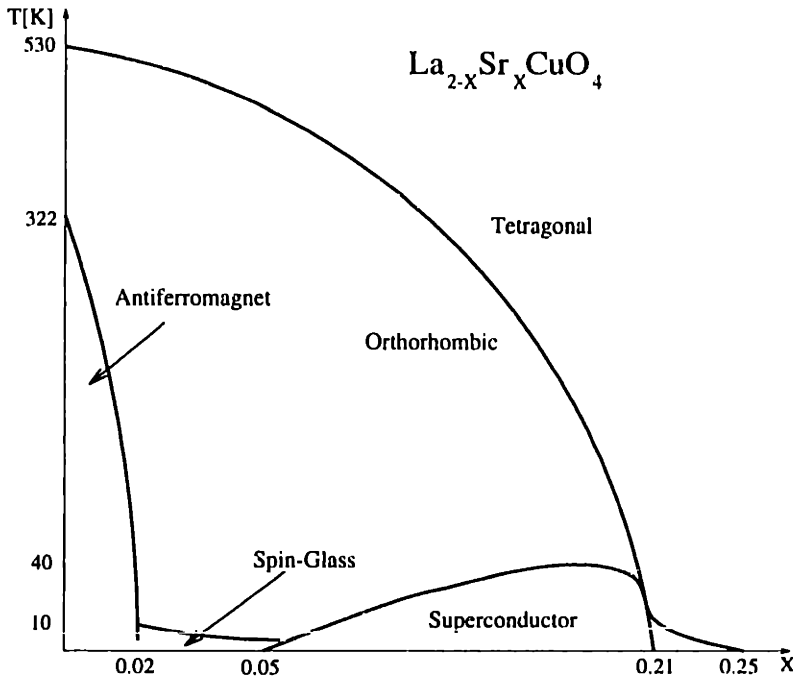

Figure 1-3: Schematic phase diagram of $La_{2-x}Sr_xCuO_4$ showing the antiferromagnetic, spin glass and superconducting regions. The diagram is not drawn to scale.

ing the electrons in the region between the atoms where the energy is lowered by the proximity of several nuclei. This chemical bond energy becomes smaller as the transition-metal ions are moved apart. Thus, depending on the relative strength of the chemical bond energy and the Coulomb repulsion, the ground state is either a metal or an insulator.

In the undoped copper oxides the copper ions in the two-dimensional CuO_2 layers are too far apart for the energy gained by delocalization to offset the energy cost of double occupancy. Indeed, an insulating ground state appears in Hartree-Fock electron-structure calculations where the electron-electron Coulomb repulsion is taken into account self-consistently [15]. Photoemission studies of $La_{2-x}Sr_xCuO_4$ and $YBa_2Cu_3O_{6+y}$ . . . that the holes are localized on the copper sites [16]. The Cu ions have configuration $3d^9$ giving each ion a spin $S = 1/2$. These localized copper spins interact through the bridging oxygen ions with a superexchange energy $J = 0.13\,\mathrm{eV}$[17] and create one of the best known physical realizations of a

two dimensional, $S = 1/2$, Heisenberg antiferromagnet[18]. The arrows in Fig. 1-2 indicate the spin-configuration in the ordered state. A truly two-dimensional antiferromagnet order first at $T = 0\,\mathrm{K}$. Weak interlayer coupling, however, causes the magnetic ground state to undergo a phase transition at the Néel temperature from true three-dimensional long-range order at low temperatures to a paramagnetic phase with long-range two-dimensional spin-correlations at high temperatures.

The superconducting phase is reached when La_2CuO_4 is doped with either Sr, Ba or excess oxygen. In Fig. 1-3 we show the phase diagram for $La_{2-x}Sr_xCuO_4$. The long-range antiferromagnetic order is very sensitive to the hole concentration in the CuO_2 planes and disappears already at 2% doping. Superconductivity appears at 5% doping with a maximum critical temperature of 40 K for the optimum composition $x = 0.15$. The superconducting phase then disappears for $x > 0.2$. We will in the next paragraphs discuss this development in some more detail, particularly with respect to the electronic excitations.

1.1.2 The Doped Semiconductor

In Fig. 1-4 we display the logarithm of the in-plane conductivity and the Hall coefficient as a function of $1/T$ for lightly doped La_2CuO_{4+y} as measured by Preyer *et al.*[19]. The different oxygen concentrations are labeled by their their respective Néel temperature. The conductivity and the Hall coefficient are both thermally activated at high temperatures with similar activation energies implying thermal activation of localized holes from acceptor states as the dominant conduction process. As the temperature decreases below 50 K, the temperature dependence of the conductivity becomes weaker with an activation energy decreasing monotonically with decreasing temperature. Such a temperature dependent activation energy is typical for variable-range hopping between localized states near the Fermi energy. The change of the dominant conduction process from simple activation to hopping at around 50 K is also manifested with a peak at $\sim$ 50 K in the temperature dependence of the Hall

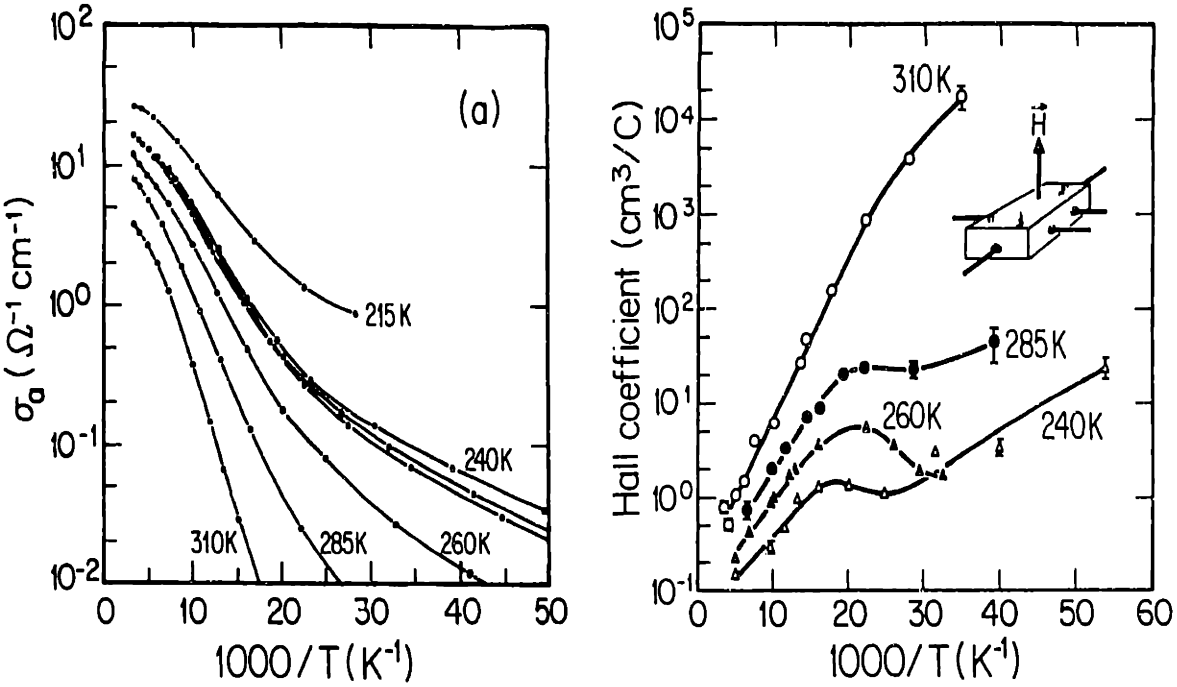

Figure 1-4: The in-plane conductivity **(a)** and Hall coefficient **(b)** as function of temperature for oxygen doped $La_2CuO_{4+y}$with y varied from 0% – 1.5%. The curves are labeled by T_N. The Hall coefficient was measured with an oscillating 0.6 Tesla field perpendicular to the CuO_2 planes with current in the planes. Inset shows five-probe geometry for Hall measurements (from Ref. [19]).

coefficient. Such peaks are observed in doped Si and Ge and result from a crossover in the dominant conduction process from one with relatively high mobility and strongly T-dependent conductivity at high temperatures to another with lower mobility and weaker T-dependent conductivity at lower temperatures. The presence of a crossover to variable-range hopping conductivity at low temperatures implies the presence of additional compensating impurities which pin the Fermi energy to the acceptor states at low temperatures.

The Hall coefficient is proportional to the inverse of the density of holes. In presence of compensation the density of thermally activated holes scales with temperatures like $\sim \exp[-E_b/k_BT]$ where E_b is the acceptor binding energy. For the most reduced sample Preyer *et al.* extract an activation energy of $E_b = 0.035(1)$ eV. The temperature dependence of the conductivity and Hall coefficient of lightly doped

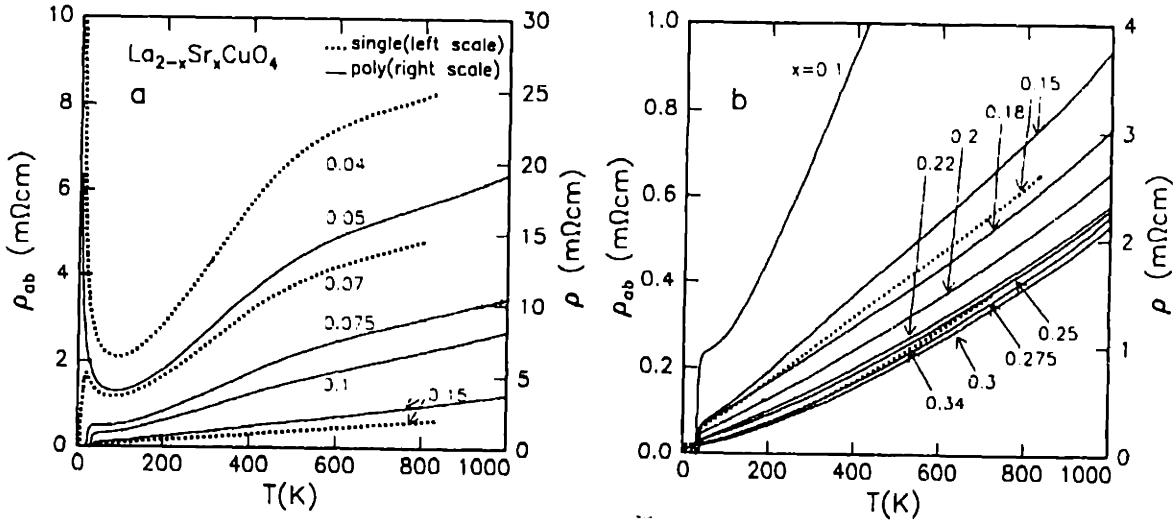

Figure 1-5: The temperature dependence of the resistivity for $La_{2-x}Sr_xCuO_4$ in the composition range (a) $0.4 \leq x \leq 0.15$ and (b) $0.1 \leq x \leq 0.34$. Dotted lines mark the in-plane resistivity (ρ_{ab}) of single-crystal films with (001) orientation. Solid lines mark the resistivity (ρ) of polycrystaline materials (from Ref. [7]).

$YBa_2Cu_3O_{6+y}$ show thermal activation with an activation energy of 0.030(1) eV[20]. The same behavior has recently been observed also for lightly Sr doped $La_{2-x}Sr_xCuO_4$ crystals[21] suggesting that compensated acceptor states $\sim$ 0.03 eV below the O $2p$ valence-band edge are a general feature among the hole-doped cuprates.

1.1.3 The Insulator-to-Metal Transition

The localization length of the impurity trapped holes growths with increased doping causing insulating $La_{2-x}Sr_xCuO_4$ to approach the insulator-to-metal transition[22]. At $\sim$ 2% doping, the resistivity increases with increasing temperature above $\sim$ 100 K reminiscent of metallic behavior[23]. The resistivity still diverges in the low-temperature limit indicating carrier localization. This low temperature localization is present until $La_{2-x}Sr_xCuO_4$ goes superconducting at $x \simeq 5\%$ as seen by the in-plane resistivity data in Fig. 1-5 from Takagi *et al.*[7]. In the superconducting regime the resistivity is linear from just above the superconducting transition temperature to almost the melting temperature. In the overdoped regime ($x > 0.2$) Takagi *et al.*

find that the in-plane resistivity scales with temperature as $\rho_{ab} \propto T^{1.5}$ over the entire temperature range with no sign of carrier localization at low temperatures. Neither of these power-law dependences are presently understood. It is clear, however, that at $T = 0\,\mathrm{K}$ $La_{2-x}Sr_xCuO_4$ display a novel doping dependence as it changes from an insulator to a superconductor to a metal with increasing carrier concentration.

Due to the two-dimensionality of the CuO_2 planes one does not expect a true insulator-to-metal phase transition, rather a gradual transition from insulating to metallic behavior[22]. Particularly in the underdoped and superconducting region it is controversial if models based on a doped insulator or a band like metal best describe the data. As an example, metallic conductivity at high temperatures and carrier localization at low temperatures are features qualitatively consistent with both heavily doped semiconductors and two-dimensional metals[24, 23]. The experimental situation is so far inconclusive. Doped copper oxides behaves as both doped insulators and metals depending on which probe is used. Specifically, by studying excitations of O $1s$ electrons into unoccupied states in $La_{2-x}Sr_xCuO_4$ using x-ray absorption Chen *et al.*[25] find that the evolution with doping in the range $0 \leq x \leq 0.15$ is consistent with a doped charge-transfer insulator. On the contrary, by measuring the Fermi surface on superconducting copper oxides using angle-resolved photo-emission spectroscopy, the Fermi surfaces are found to span almost the entire Brillouin zone with a volume 5-6 times larger than the corresponding doping concentration[5, 6, 26], inconsistent with a doped semiconductor picture. For both hole[27] and electron[26] superconductors, the measured Fermi surfaces are also found to be in good agreement with three-dimensional local-density band structure calculations. The very same calculations that fail so badly in describing the undoped copper oxides.

1.1.4 Interaction with Magnetic Excitations

The excess oxygen holes induce a spin on the in-plane oxygen sites. Since the in-plane oxygen ion is located in between the Cu ions, the excess oxygen spins frus-

trate the antiferromagnetic alignment of the Cu spins. At $\sim 2.0\,\%$ doping, the local spin-frustration is strong enough to destroy the 3D long range antiferromagnetic order as implied in Fig. 1-3. Still, fluctuating 2D antiferromagnetic correlations persist at higher doping levels[28, 29], even into the superconducting phase[30]. At low temperatures and $x \sim 0.02 - 0.05$ these fluctuating spins freeze into a spin-glass phase creating static internal magnetic fields as seen by nuclear quadrupole resonance[31]. A clear demonstration of a coupling between the spin-configuration and the charge transport is reported for insulating La_2CuO_4 where changes in the spin-configuration and changes in the hopping conductivity with applied magnetic field have been correlated[32]. In the metallic phase, spin fluctuation scattering is expected to contribute to the conductivity[33] in much the same way as in transition metals where the conducting *s* electrons scatter from the fluctuating spin-excitations in the *d* band. By measuring the generalized magnetic susceptibility using inelastic neutron scattering, Keimer *et al.*[34] show that such scattering in $La_{1.96}Sr_{0.04}CuO_4$ gives rise to a resistivity linear in temperature, possibly explaining the anomalous linear resistivity.

1.1.5 Interaction with Vibrational Excitations

Insulating copper oxides are strongly ionic. As in most ionic insulators some of the optical phonon modes have large dipole moments as seen from the large difference between the static dielectric constant $\epsilon_s \simeq 30$[22] and the optical frequency value $\epsilon_\infty = 5$[35]. With such a large difference we expect added charge carriers to lower their energy by polarizing the lattice, forming quasi particles known as polarons. One of our main results is the demonstration of such polaron formation in insulating La_2CuO_{4+y}. In addition we demonstrate that the intermediate-strength electron-phonon coupling persists in lightly oxygen La_2CuO_{4+y}. This electrostatic phonon interaction is expected to weaken with increased doping as a higher concentration of mobile carries more effectively can screen the phonon-induced electric dipole

field. Several experiments, however, indicate that the carriers are strongly coupled to some vibrational excitations in the metallic phase. Specifically, the strong absorption structure observed in the in-plane optical conductivity of the superconducting cuprates is found to be correlated with the dielectric loss function for the optical phonon modes[36]. Moreover, pulsed neutron diffraction measurements detect a local structural change at T_c for $Tl_2Ba_2CaCu_2O_8$[37]. In this experiment short-range correlated displacements of O and Cu perpendicular to the CuO_2 plane are observed where the the arrangement of the O atoms is different above and below T_c. Finally, it has been argued that the disappearance of superconductivity in overdoped $La_{2-x}Sr_xCuO_4$ is associated with the orthorhombic to tetragonal structural phase transition[38] near $x = 0.20$ as shown in Fig. 1-3, suggesting a relationship between superconductivity and subtle structural change.

1.1.6 The Scope of this Thesis

From the phase-diagram in Fig. 1-3 we see that the normal state of the superconductor and the paramagnetic state of the insulator are connected without any intermediate phase boundary. This suggests that their respective properties are strongly related. Since everything we know about the undoped copper oxides is consistent with the physics of antiferromagnetic charge-transfer insulators, the fundamental issue to understand is what happens when excess carriers are added to such strongly correlated insulators. Theoretically, this problem is attacked from both the insulating and the metallic limit considering both doped Hubbard models[39] and Fermi Liquid theories[27]. The basic ingredient in most of these models is the on-site Coulomb repulsion. As we have seen, a growing amount of evidence suggests that the conducting holes interact strongly with both magnetic and vibrational excitations, not generally included in standard Fermi liquid and Hubbard models. To sort out the contribution from these and other effects to the the nature of the low-energy electronic excitations in metallic copper oxides is a formidable task. An extensive understanding of the low-

lying electronic excitations in the insulating phase will certainly be a valuable guide in such an effort. The overall goal of this work is to give a substantial contribution to our understanding of the insulating copper oxides. By building on previous results from a variety of experimental probes we will use optical spectroscopy to study the low-lying electronic excitations in La_2CuO_{4+y} as we develop a consistent picture of their nature and origin.

1.2 Electronic Excitations in Insulating La_2CuO_{4+y}

In understanding the electronic excitation spectrum of undoped La_2CuO_{4+y} it is sufficient to only consider the CuO_6 cluster, including only the Cu $3d$ and O $2p$ orbitals. In the ground state the hole is localized in the Cu $3d_{x^2-y^2}$ orbital. In Fig. 1-6 we have sketched the relative position of the oxygen p and copper d bands as given by the CuO_6 cluster calculations[12]. We have also included the the contributions from both the acceptor states and the compensating impurities as determined by the conductivity and Hall coefficient data in Fig. 1-4.

We distinguish between two types of excitation; charged excitations which change the local charge distribution and neutral excitations which do not change the local distribution of charge. For the copper oxides the neutral excited states are the excited states of the $3d^9$ Cu ion. Transition from the $d_{x^2-y^2}$ ground state to any other excited state corresponds to a charged excitation. The main difference between charged and neutral excitations is that the latter do not represent empty states that can be occupied by excess holes as in a traditional semiconductor. Excess holes change the local charge distribution and can consequently only occupy charged excited states. Thus the neutral excited states in Fig. 1-6 do not fill up by the addition of excess holes.

An other difference between the charged and neutral excitations are the band width. The band width reflects the ability for excitations to move between clusters.

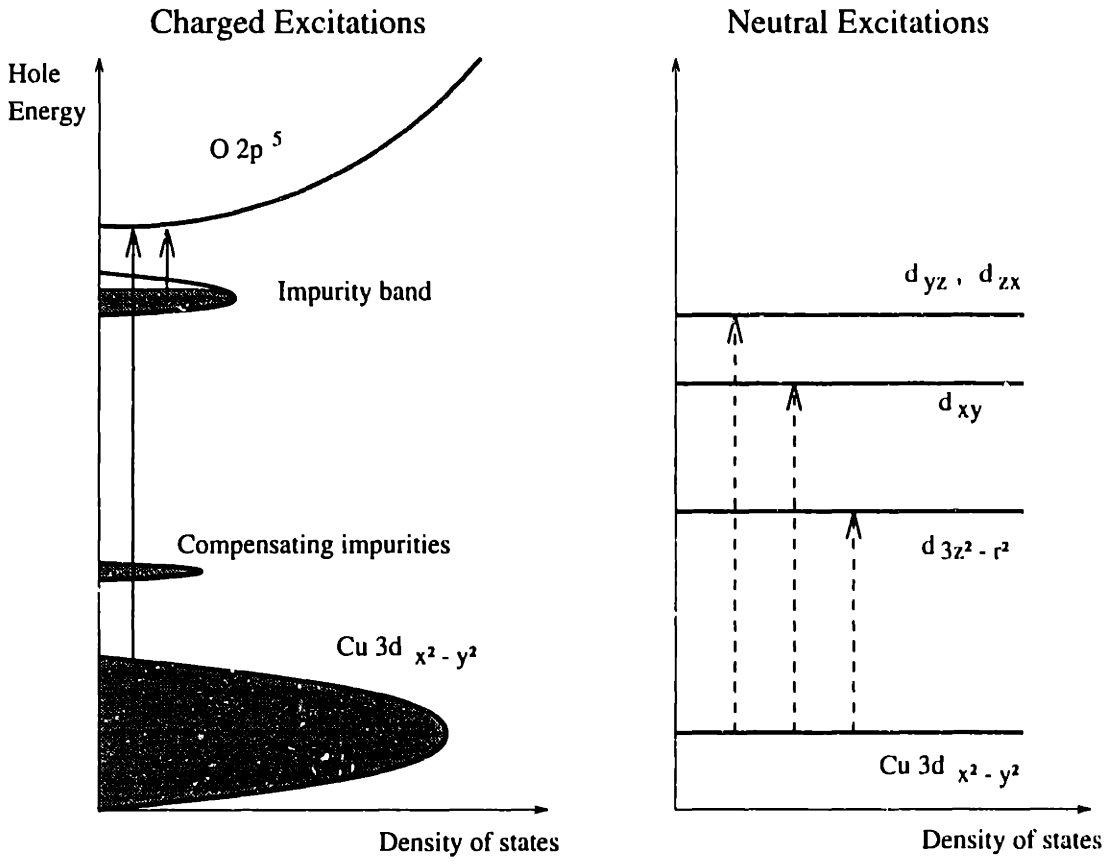

Figure 1-6: A schematic of the charged and neutral excited states with one hole per CuO_6 cluster. The arrows represent electric dipole allowed (solid arrows) and electric dipole forbidden transitions (broken arrows).

The charged excitations excite the localized hole from one Cu site to neighboring Cu or O ions and leave the original Cu ion with one excess electron in a $3d^{10}$ configuration. This *excess* Cu electron can move between Cu sites without overcoming any additional Coulomb repulsion. Thus the excess Cu electron form an energy band width of order the Cu-to-Cu hopping energy ~ 1 eV. The final state of the neutral excitation, on the other hand, are excited states of the original $3d^9$ configuration. Since the local charge distribution is preserved, the neutral excitations must overcome the on-site Coulomb repulsion in order to move between sites and the corresponding band widths are order of magnitudes smaller.

The energy gap for electronic excitations is determined by the lowest energy

electric-dipole allowed transition. Non of the neutral excited states qualify as final states for an electric-dipole allowed transition since both the initial and final state have the same parity relative to the same Cu ion. Possible candidates for the gap excitation are transfer of a hole from one Cu ion to the next at the energy cost of double occupancy U as in a Mott insulator, $2\,d^9 + U \rightarrow d^8 + d^{10}$, or transfer of holes from the Cu ion to the neighboring O ions, $p^6 + d^9 + \Delta \rightarrow p^5 + d^{10}$. The latter transition is known as a charge transfer excitation where the excitation energy is determined by the energy difference Δ between the O $2\,p^5$ and the Cu $3\,d^9$ state. Depending on which of these two transitions that apply, the hole in the final state of the gap excitation has either Cu or O character. Direct evidence for holes on the O site is provided by spectroscopic probes with chemical specificity studying excitations of O $1s$ electrons into the unoccupied states. Electron energy-loss spectroscopy[40] and x-ray absorption[41] both find the strength of the $O1s \rightarrow O2p$ transitions to grow with doping at a rate corresponding to the dopant concentration. Thus the O $2p^5$ band is positioned in between the Coulomb split Cu $3d$ bands and the lowest energy electronic excitation of undoped La_2CuO_4 corresponds to a transfer of hole from the Cu 3d band to the O 2p band as indicated in Fig. 1-6 where $\Delta \sim 2\,\mathrm{eV}$ equals the charge transfer energy.

In Fig. 1-7(a) we display the reflectivity of undoped ($y = 0$) and lightly oxygen doped ($y = 0.014$) La_2CuO_{4+y} crystals at $T = 10\,\mathrm{K}$ with the electric field polarized parallel to the CuO_2 layers. Thus, the spectra reveal electronic excitations within the copper oxygen layer. In Fig. 1-7(b) we display the imaginary part of the dielectric function for the undoped and doped crystals at 10 K extracted from the reflectivity spectra in panel (a) using the Kramer-Kronig relations. For completeness we show in panel (c) the same data displayed as optical conductivity and absorption coefficient respectively. For the undoped crystal the lowest energy excitations are the charge-transfer excitation with a characteristic peak at 2.2 eV and a much weaker unidentified absorption band at 1.75 eV. Upon doping, three mid-infrared bands appear below the

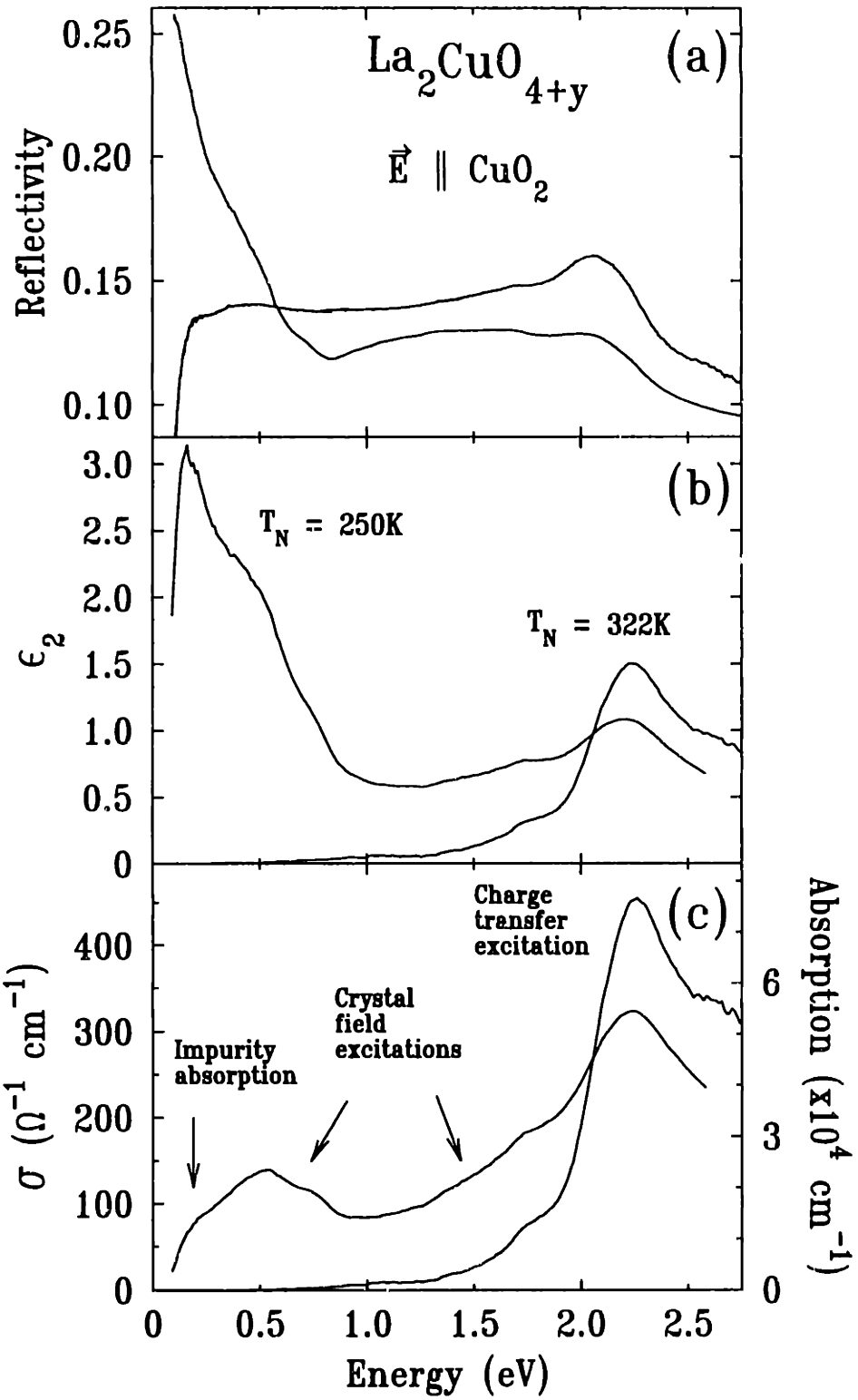

Figure 1-7: **(a)** In-plane reflectivity spectra of La_2CuO_{4+y} with $y = 0$ and $y = 0.014$ at 10 K. **(b)** The in-plane $\epsilon_2(\omega)$ spectra extracted from the reflectivity spectra shown in (a). **(c)** The same spectra as in (b) but displayed as conductivity and absorption coefficient respectively.

charge transfer edge, two broad bands near 1.5 eV and 0.5 eV respectively and a band near 0.13 eV which is stronger in $\epsilon_2(\omega)$ but weaker in $\sigma(\omega)$. Three bands with similar energies appear in photo-induced absorption spectra[42, 43] suggesting that the photo-induced and doping induced carriers have the same effect on the optical spectra. In chapter 5 we will demonstrate this effect with space charges induced in La_2CuO_{4+y} by electric fields. Together these experiments show that the observed enhancement of the absorption bands upon chemical doping is primarily caused by the excess holes in the CuO_2 planes and not by the increased impurity or defect concentration that induce them.

In this thesis we will study both the charge transfer excitation and the doping enhanced mid-infrared bands. One of the main results from this work is the clear demonstration that the 0.13 eV excitation is due to photo-ionization of impurity bound holes. Furthermore, we will show that the two remaining absorption bands at 0.5 eV and 1.5 eV can be accounted for as charge-carrier induced crystal field excitations. Thus, the entire low-energy electronic excitation spectrum can be understood using the diagram illustrated in Fig. 1-6.

To ease the introduction to this topic we will in the following sections discuss each of these absorption bands in more detail. We will give a short review of the history of their interpretation, discuss our contribution and present the current understanding of the interactions involved.

1.2.1 The charge transfer excitation

We can picture the charge-transfer excitation in La_2CuO_4 much the same way as we view photoexcitation of an electron across the band gap in an semiconductor. The fact that the energy gap is a consequence of Coulomb correlations will not make any difference for the absorption spectrum. Due to the lamellar structure of the copper oxides, the oxygen band is strongly anisotropic and is almost without dispersion normal to the CuO_2 planes as shown by Hartree-Fock electron-structure calculations[15].

The corresponding joint density of states increases sharply at the charge-transfer edge emulating a step function typical for 2D electronic systems. The observed absorption spectrum, however, does not reflect the joint density of states but is dominated by a sharp peak near the band edge as seen in Fig. 1-7(c). Such structure is reminiscent of excitonic absorption, and several early studies suggested that it arises from creation of bound exciton[35, 44]. Such an interpretation was contradicted by the observation of photoconductivity in the same spectral region[45], demonstrating that the excitations result in separated electrons and holes. A detailed understanding of the charge-transfer excitation was first provided by our reflectivity measurements of the charge-transfer excitation spectrum and its temperature dependence[46]. These measurements are reviewed in chapter 3. We find that the excitation spectrum and its temperature dependence can be understood if both polaron coupling and electron-hole correlations are taken into account. The most important result from this discussion is the clear demonstration of an intermediate-strength coupling between the photo-excited charge carriers and certain longitudinal optical phonon modes.

1.2.2 The mid-infrared bands - impurity absorption

Both the impurity binding energy $\sim 0.03\,\mathrm{eV}$ and the the impurity density $x \sim 0.02$ necessary to induce the insulator-to-metal transition are a factor ten smaller than expected from purely electronic screening $\epsilon_\infty \simeq 5$ of the hole-impurity Coulomb attraction. The static dielectric constant $\epsilon_o = 30$ is six times larger suggesting that the small values could result from additional screening by the optical phonons. Since charge carriers injected into La_2CuO_4 by photoexcitation form polarons, one also expects impurity-induced carriers to form polarons, at least at low doping concentrations where the electrostatic electron-phonon interaction is not screened by the free carriers. Thomas *et al.* [47] pointed out that the electron-phonon coupling is strong enough to make the optical ionization energy of impurities much larger than the thermal ionization energy. While the lattice has time to relax its deformation

during a thermal excitation, the lattice cannot respond on the time scale of an optical excitation. Thus to ionize, the impurity trapped hole must be supplied the binding energy to both the impurity and the lattice. Thomas *et al.* proposed that the 0.5 eV band results from this optical ionization and that the 0.13 eV band arises from magnetic excitations. The latter idea was studied theoretically by Millis *et al.* [48] who calculated the optical absorption of a spin-$\frac{1}{2}$ carrier bound to a defect site in an insulating antiferromagnet. They found that the interaction of the carrier with the antiferromagnetic background leads to a low frequency absorption feature near the zone boundary magnon energy ($\simeq 2J = 0.26$ eV). They conclude that this feature is neither consistent in peak position nor total oscillator strength with the observed 0.13 eV absorption band and suggest that the feature is due to electron-phonon coupling. This conclusion is supported by photo-induced absorption measurements which find a correlation between the temperature dependence of the 0.13 eV band and that of the carrier induced changes in the optical phonon spectra, indicative of such a coupling[43, 49, 50]. A complete picture of the nature of the 0.13 eV band was provided by our resent study of the mid-infrared reflectivity spectrum and its temperature dependence in lightly doped La_2CuO_{4+y} [51]. These measurements are discussed in chapter 4. We find that oscillator strength is transferred from the ~ 0.13 eV absorption band into the free carrier conductivity with increasing temperature. This shows that the 0.13 eV band, rather than the one at ~ 0.5 eV, results from photo-ionization of holes bound to oxygen acceptors. Moreover, both the position and the width of the 0.13 eV absorption spectrum are shown to be consistent with localized holes coupled to optical phonon modes. Thus, in addition to resolve questions concerning the nature and origin of the lowest energy mid-infrared band we clearly demonstrate that in insulating La_2CuO_{4+y}, localized as well as free holes form polarons.

1.2.3 The mid-infrared bands - crystal-field excitations

While the 0.13 eV band can be identified through its temperature dependence, the interpretation of the the higher energy infrared bands is complicated by the paucity of spectral features and the absence of strong temperature dependence. As a consequence, a large number of possible mechanisms have been proposed as the origin. We will not discuss all the different ideas here. A complete review can be found in Ref. [52]. Instead, let us proceed by eliminating some candidates. Since the 0.13 eV absorption band is due to photoexcitation of shallow impurities, the 0.5 and 1.5 eV must have a different origin. One cannot rule out impurity absorption in general. One could envision excess holes localized in both deep and shallow impurity states where the strongly localized carriers do not thermally ionize below room temperature. If the 0.5 eV and 1.5 eV bands represent excitations of such deep impurities, possibly coupled to vibrational and magnetic excitations, the corresponding oscillator strength should reflect the density of such states. The effective number of carriers $N^*_{eff}(\omega)$ involved in transitions with excitation energy less than $\hbar\omega$ is defines as

$$N^*_{eff}(\omega) = \frac{2m^*}{\pi e^2}\int_0^{\omega} d\omega'\,\sigma(\omega'), \tag{1.1}$$

where e is the electronic charge, m^* the effective mass and $\sigma(\omega)$ the optical conductivity. By integrating the optical conductivity spectra in Fig. 1-7(c) over the energy range $0.1 - 1.5$ eV, the strength of doping induced mid-infrared excitation is determined to be $N^*_{eff}\, m_o/m^* \simeq 0.045$ per Cu ion. We will in chapter 4 argue that the appropriate effective mass is $m^* = 2m_o$. With an impurity concentration of ~ 0.008 per Cu ion for $T_N = 250$ K, estimated from Hall coefficient data in Fig. 1-4, the effective number of carriers involved in the mid-infrared excitations is an order of magnitude larger than the impurity concentration. Similar results are also demonstrated for Sr doping. By integrating the spectral weight of the optical conductivity in the lightly doped limit over the the range $0.004 - 1.5$ eV, Uchida *et al.*[35] finds that

in $La_{2-x}Sr_xCuO_4$ the total number of carriers involved in the mid-infrared excitations equals several times the doping concentration. Such an overabundance of oscillator strength is inconsistent with a simple deep impurity picture. Moreover, Uchida *et al.* also find that the total oscillator strength for excitation below $\sim 3\,eV$ is almost independent of doping. Since we know that the strength of the 0.13 eV band comes from free carrier conductivity, this behavior suggests a transfer of oscillator strength from the charge-transfer band into the 0.5 eV and 1.5 eV bands with doping. This behavior is also found in electron-doped copper oxides and was first observed by Cooper *et al.*[53] in $Pr_{2-x}Ce_xCuO_4$. The effect is seen in the $\sigma(\omega)$ spectra of oxygen doped La_2CuO_{4+y} displayed in Fig. 1-7(c).

A potential breakthrough in the understanding of the 0.5 end 1.5 eV infrared bands was recently provided by Perkins *et al.*[54]. By measuring the transmission through $\sim 100\,\mu m$ thick undoped single crystals of various copper oxides, a common absorption feature near $0.5eV$ was observed. By studying its polarization dependence, the structure was demonstrated to arise from weakly electric-dipole allowed excitations. The features were ascribed to a crystal-field exciton near 0.4 eV with multimagnon and phonon sidebands. The exciton was identified as resulting from transitions between the $d_{x^2-y^2}$ and d_{z^2} crystal-field split states. A second band near 1.5 eV was assigned to the $d_{x^2-y^2} \rightarrow d_{xy}$ transitions.

The only way $d-d$ transitions can be electric-dipole allowed is through mixing odd-parity states with the even parity d states. If we assume that the effect of induced carriers in the CuO_2 plane is to increase the hybridization between p and d symmetry states, this will not only explain the mid-infrared band but also explain why the growth of these bands is accompanied by transfer of spectral weight from the charge-transfer excitation. Of course, a connection between the two mid-infrared bands induced by doping and the weak crystal-field excitations remains to be proven. In an effort to investigate if the 0.5 eV and 1.5 eV infrared bands have the symmetry of the appropriate crystal field excitations, we have studied the electroreflectance

spectra of undoped and doped La_2CuO_{4+y}[55]. These measurements are discussed in chapter 5. By breaking the spatial inversion symmetry of the Cu sites with an in-plane electric field, the crystal field transitions become weakly dipole allowed. Depending on the symmetry of the perturbing electric field, different sets of crystal-field excitations become possible. We show that the response of the 1.5 eV infrared band to a perturbing electric fields is consistent with a $d_{x^2-y^2} \rightarrow d_{xy}$ transition, both in polarization and strength. The 0.5 eV band is found to be inconsistent with transitions to either d_{xy} or d_{yz}, d_{zx} symmetry states, supporting the interpretation that it arises from the $d_{x^2-y^2} \rightarrow d_{z^2}$ transition. Both the excitation energies and the symmetries are in agreement with those of the crystal-field excitations and magnon sidebands in the undoped material[54]. Hence, these excitations emerge as strong candidates for the 0.5 eV and 1.5 eV infrared bands in insulating lightly doped copper oxides.

Chapter 2

Experimental Details

2.1 Sample Preparation and Characterization

The La_2CuO_{4+y} single crystals studied in this thesis were grown by myself in collaboration with MIT Crystal Physics Laboratory by the top-seeded solution growth method using CuO flux[58]. The crystals were grown with a large (100) tetragonal surface to allow for polarization of the light parallel and perpendicular to the CuO_2 layers. A Laue backscattering device was used to orient the crystals. The crystals were cut with area $\sim 5\,\mathrm{mm}^2$ and thickness $\sim 2\,\mathrm{mm}$.

The magnetic ground state in La_2CuO_{4+y} undergoes a phase transition at the Néel temperature from true 3D long-range order at low temperatures to a paramagnetic phase with long-range 2D spin-correlations at high temperatures. In La_2CuO_{4+y} this phase-transition can be easily seen because of a sharp peak in the magnetic susceptibility, $\chi(T)$, at T_N. The Néel temperature is very sensitive to hole concentration in the CuO_2 planes, as is evident from the phase diagram in Fig. 1-3, and is used by our group as a probe of the doping level. As-grown, the crystals contain a density of $\sim 4 \times 10^{19}\,\mathrm{cm}^{-3}$ holes due to doping by oxygen acceptors, sufficient to reduce the Néel temperature to $T_N = 240\,\mathrm{K}$. The crystals were reduced by annealing at 1170 K for 30 minutes in a vacuum of $\sim 2 \times 10^6$ torr increasing the Néel temperature to 322 K.

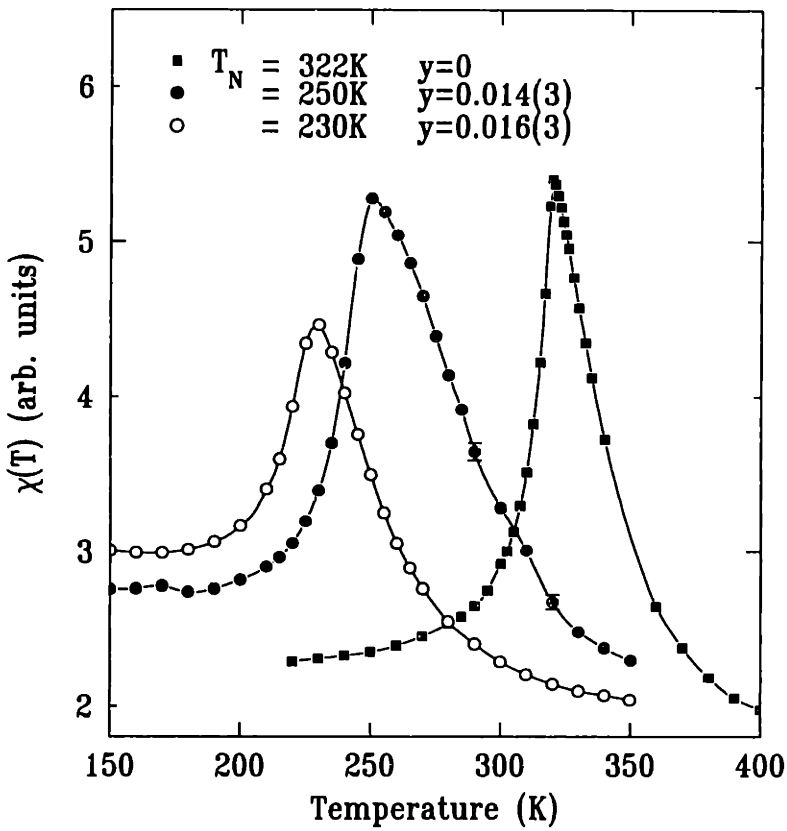

Figure 2-1: Magnetic susceptibility for La_2CuO_{4+y} for the different doping levels used in the study. The conversion from Néel temperature to exact oxygen concentration is taken from Ref.[59].

To add extra oxygen, the crystals were annealed in an oxygen rich atmosphere. This resulted in crystals with measured Néel temperatures of $T_N = 230K$ and 250 K corresponding to excess oxygen concentrations of $y = 0.016(3)$ and $0.0014(3)$, respectively. In Fig. 2-1 we display typical magnetic susceptibility data for the crystals studied in the thesis. The data were taken with a 1 Tesla field normal to the CuO_2 planes using a Quantum Design SQUID system. The sharp peak in the magnetic susceptibility indicates that the oxygen is distributed homogeneously at all doping levels. The corresponding excess oxygen concentration is determined by previous experiments[59]. Note that the oxygen concentration has a large uncertainty. The Néel temperature, however, is known to within ± 2 K.

The annealing process is known to deplete the surface of copper to a depth of

roughly $2\,\mu$m[60]. We also expect as-grown surfaces to be depleted of copper since new-grown crystals are cooled in air from $\sim 1300\,$K to room temperature, effectively annealing the crystals. Therefore, several micrometers were ground off before polishing, and the surfaces were subsequently etched for 20 minutes in a solution of 1% Br in methanol. This careful treatment of the surface is of crucial importance to obtain high-quality data. The 2 eV in-plane reflectivity peak in undoped La_2CuO_4, for example, was found to become sharper the longer the crystal was etched saturating at roughly 20 minutes.

2.2 Reflectivity Measurements

The reflectivity was measured on a tetragonal (100) surface allowing polarization of the light parallel and perpendicular to the CuO_2 layers. The spectra were measured at $\sim 10°$ incidence in the energy range 0.1-3.1eV using a 218 McPherson grating monochromator. The energy resolution changes from 0.0008 eV at 0.1 eV to 0.015 eV at 3.0 eV. The reflectivity was normalized to that of an Al mirror, whose absolute reflectivity was measured by removing it and placing the detector in the incident beam. The reflectivity spectrum of the Al reference mirror has temperature dependent structure above 0.9 eV. Thus, for $T \neq 295K$ we normalized the in-plane spectrum to the out-of-plane spectrum which has neither structure nor strong temperature dependence. The true in-plane reflectivity was then obtained by multiplying this ratio with the out-of-plane reflectivity at $T = 295\,$K. The possible errors induced by this procedure were estimated by careful measurements of the temperature dependence in the out-of-plane reflectivity. By first measuring the spectrum of the Al reference at $T = 295\,$K and then, without changing the system, measuring the out-of-plane spectrum for La_2CuO_4 at different temperatures, we found the relative change in the out-of-plane reflectivity to be less than 0.003 for $\hbar\omega < 2.8\,$eV in the temperature range 10 K to 295 K. The accuracy of the absolute reflectivity depends on the quality

of the Al reference and the crystal surface and is estimated to ~ 0.02.

A Glan-Thomson prism polarizer with an average extinction ratio of $\sim 1 \times 10^5$ was used above 0.5 eV. In the infrared we used a double BaF_2 wire-grid polarizer with an average combined extinction ratio of $\sim 1 \times 10^4$. A table of the filter, grating and detector combinations used in the entire energy range is supplied in appendix A

The reflectivity data were transformed to give the complex dielectric function using the Kramers-Kronig relations displayed in Appendix B. This procedure requires extrapolation of the reflectivity at low and high energies. At high energies ($\hbar\omega >$ 3.0 eV) we matched published ultraviolet single crystal reflectivity data[35] to our spectra. Variations of the high-energy extrapolation had no measurable impact on the dielectric spectrum below 1.5eV. The results in the 0.1−0.2 eV range are somewhat dependent on the low-energy extrapolation. Because the spectrum is dominated by phonon excitations for $\hbar\omega \leq 0.09$ eV, reflectivity measurements at lower energies would not improve the accuracy of the electronic absorption spectrum. Instead, we assumed a constant reflectivity at low energies for the undoped samples (y=0). For the doped sample (y=0.014) we used a calculated reflectivity spectrum for a Lorentzian absorption band centered at 0.13 eV. This is a natural low-energy extrapolation of the data as is apparent from the $\epsilon_2(\omega)$ spectra in Fig. 1-7(b). A detailed account of the modeling of the 0.13 eV excitation is found in Chapter 4. We estimate the uncertainty in ϵ_2 at 0.15 eV to be of order 5%.

2.3 Modulation Reflectivity Measurements

The modulation reflectivity was measured on a tetragonal (100) surface allowing polarization of the light parallel and perpendicular to the CuO_2 layers. The surface was prepared as described in section 2.1.

The modulation experiment was performed in two different configurations as illustrated in Fig. 5-2. In configuration (a) we used a transparent metal-insulator structure

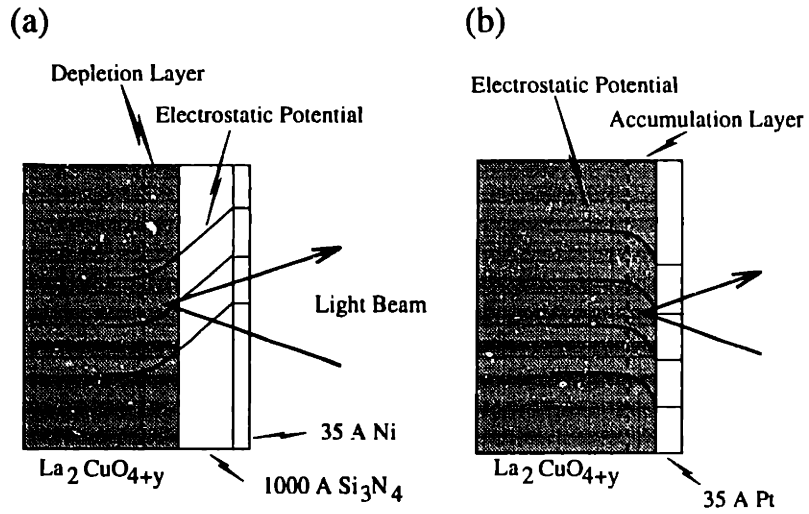

Figure 2-2: **(a)** The metal-insulator-semiconductor configuration used to modulate the electric field in a natural depletion layer. **(b)** The metal-semiconductor configuration used to modulate the hole concentration in a natural accumulation layer. The displayed ideal electrostatic potential equals the hole potential.

on top of the La_2CuO_{4+y} single crystal. The structure was fabricated by depositing 1000 Å of Si_3N_4 using Plasma Enhanced Chemical Vapor Deposition. During the deposition the structure was annealed at 473 K in vacuum. Auger electron energy depth profiles was taken on test samples to characterize the $La_2CuO_{4+y} - Si_3N_4$ interface. In Fig. 2-3 we display a typical AES profile. A sharp clean interface is observed with no chemical inhomogeneities. 35 Å of Ni was evaporated on top of the Si_3N_4 as a transparent electrode. The Ni films were tested to have metallic T-dependence of their resistance down to 77 K. The transmission of the Ni film was measured to be ~ 0.85 in the entire energy range ($\hbar\omega < 3\,\mathrm{eV}$). In configuration (b) the transparent metal electrode was evaporated directly on the La_2CuO_{4+y} surface. We used a 35Å Pt film to avoid chemical reaction between the metal electrode and the La_2CuO_{4+y}. Like Ni, the Pt film showed metallic behavior.

The modulation reflectivity spectra were measured at $\sim 10°$ incidence in the energy range 0.5-3.1eV. A 20 Volt peak-to-peak 287 Hz signal was applied between the metal-electrode and the La_2CuO_{4+y}. The ac component was extracted from the

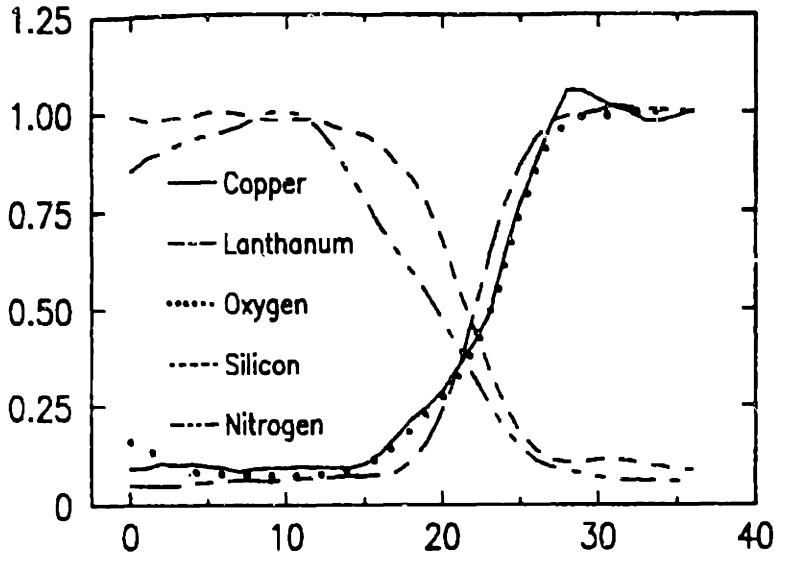

Figure 2-3: AES atomic concentration (arbitrary units) as a function of ion-milling cycle number of the $Si_3N_4 - La_2CuO_{4+y}$ interface after annealing at 473 K. The milling rate was determined to 70 Å/cycle for Si_3N_4 and 25 Å/cycle for La_2CuO_{4+y}(from Ref. [60]).

total photodetector signal by a lock-in amplifier and then divided by the dc component giving $\Delta R/R$ directly. The $\Delta R/R$ data were transformed to give the change in the complex dielectric function using a modified version of the Kramers-Kronig relations discussed in Appendix B. Again, extrapolations are necessary. At the high energy end of the spectrum the modulation signal levels off to a small and constant value. By measuring $\Delta R/R$ up to 4.5 eV at a few accessible photon energies this trend was found to continue, allowing us to substitute $\Delta R/R$ at high energies ($\hbar\omega > 3.1eV$) with a constant. The low-energy extrapolation is not so simple. In addition to the 0.5 eV band, photo-ionization of localized polarons gives rise to the strong absorption band at 0.13 eV. However, by trying a variety of functional forms for the extrapolation, we estimate the uncertainty in $\Delta\epsilon_2$ at 0.6 eV to be of order 5%. For the modulation data shown in chapter 5, we have used a Lorentzian absorption band centered at 0.5 eV to extrapolate $\Delta R/R$ below 0.5 eV.

Chapter 3

The Charge-Transfer Excitation

The charge-transfer excitation in the copper oxides is unusual in the sense that it combines the character of an ionic insulator with that of a two-dimensional band edge. In ionic insulators, i.e. Alkali Halides, the dipole moments associated with the optical phonon modes induce strong electron-phonon coupling. For a 2D band edge, the electron-hole interaction induces absorption edge resonances stronger than for a 3D band edge due to more available $\vec{k}$-space near the band edge. We will in this chapter show that both the charge-transfer spectrum and its temperature dependence can be explained if the reduced dimensionality and electron-phonon coupling are taken into account. We start out in section 3.1 by discussing the effect of long- and short-range electron-hole interactions on a two-dimensional band edge. Only a short-range electron-hole interaction is found to be consistent with the charge-transfer spectrum. In section 3.2 we show that the temperature dependence of the charge-transfer reflectivity peak arises from polaronic coupling to optical phonons. We discuss the polarons in more detail in section 3.3 and calculate their self-energy and lifetime. In section 3.4 we demonstrate that a theory in which the final state consists of electron and hole polarons coupled to each other by a short range potential provides an excellent fit to the optical data at low temperatures and predicts the spectrum up to $\sim 400\,\mathrm{K}$ with no adjustable parameters. We close this chapter by discussing the

nature and origin of the short range electron-hole interaction.

3.1 Exciton Effects

In Fig. 3-1(a) we show spectra of the optical reflectivity at 122K and 447K for polarization parallel and perpendicular to the CuO_2 sheets. The prominent charge-transfer feature near 2.0 eV is observed only for the in-plane spectrum. The out-of-plane spectrum shows no structure in this energy region demonstrating the 2D nature of the excitations. The charge-transfer peak is seen to sharpen and move to higher energies upon cooling. At $T \sim 120$ K this evolution saturates and further cooling alters neither the position nor the width of the peak. In addition to the charge-transfer peak, a kink in the reflectivity near 1.75 eV is observed in the in-plane spectrum. This feature, which is only resolved at low temperatures, is observed in both doped and undoped samples as is evident from Fig. 1-7(b).

The imaginary part of the dielectric function, ϵ_2, at 122 K for the in-plane spectrum is shown in Fig. 3-1(b), together with the photoconductivity at 132K for an identically prepared crystal[45]. The peak in ϵ_2, at 2.25 eV, has a total width of only ~ 0.4 eV. The photoconductivity has a threshold that coincides with that of ϵ_2, indicating that the absorption is associated with the creation of free electrons and holes. The plateau on the low energy side of the 2.0 eV absorption edge results from the kink in the reflectivity (Fig. 3-1a). This second excitation, centered at 1.75eV, has no associated photoconductivity indicating that the absorption results in the creation of excitons.

Even though the absorption above 2 eV leads to separated electron-hole pairs, the narrowness of the peak at 2.25 eV indicates that the interaction between the electron and hole is important in the interband transitions as well as in those of the bound exciton. It is well known that the electron-hole interaction enhances matrix elements for interband transitions just above threshold. Even though the electron and hole are free, they are still correlated. These correlation effects transfer spectral weight from

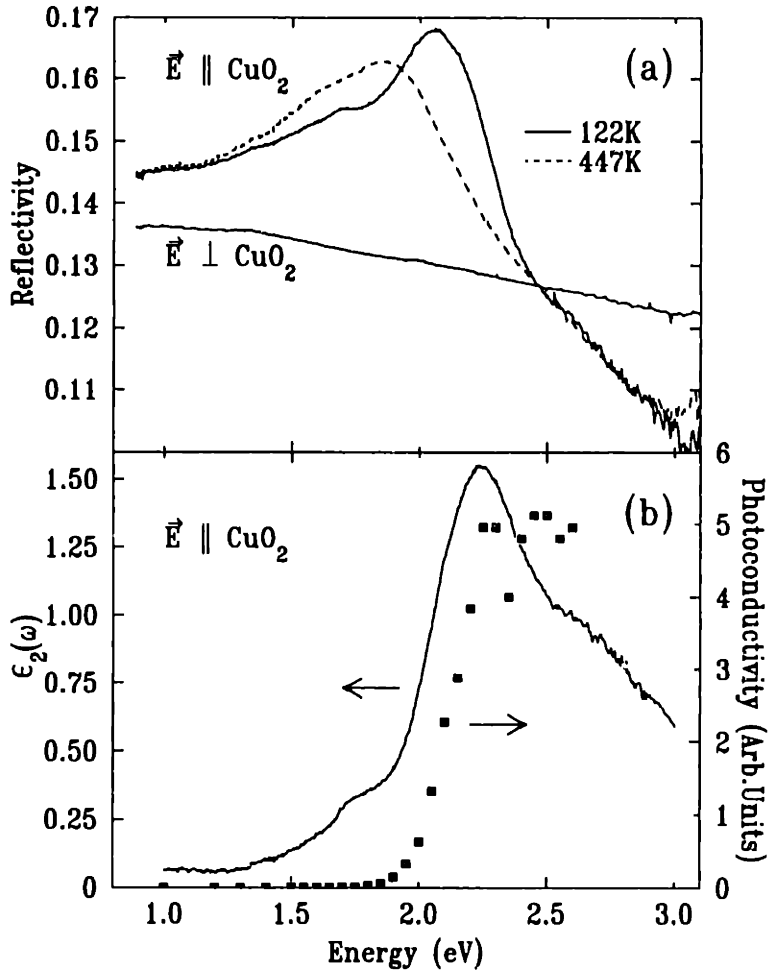

Figure 3-1: **(a)** Reflectivity spectra of La_2CuO_4 at T=122K and 447K. **(b)** In-plane $\epsilon_2(\omega)$ at T=122K together with the photoconductivity at $T = 132\,\mathrm{K}$ on an identically prepared sample. (Photoconductivity data from Ref.[45]).

the continuum to the absorption edge where the kinetic energies of the free electron and hole are small and they better can satisfy their need to stay close together. This increase in the transition probability near the band edge is weighted by the number of available states to give the final absorption spectrum. While a 2D band edge has a flat energy-independent density of states, the density of states at a 3D band edge goes to zero as $\sqrt{\hbar\omega - E_g}$ reflecting less available $\vec{k}$-space for the continuum transitions near $k = 0$. Consequently, the enhancement of the absorption edge is more dramatic in 2D than in 3D. In Fig. 3-2 we display the calculated $\epsilon_2(\omega)$ for a two-dimensional band

edge including the electron-hole interaction. We have considered both long- and short-range interactions representing Mott-Wannier and Frenkel excitons, respectively. The exact absorption spectrum for a 3D band edge with a long-range Coulombic electron-hole interaction potential was first calculated by Elliott[65]. The two-dimensional case was considered later[64]. A detailed discussion of the Mott-Wannier excitonic band edge in both two and three dimensions can be found in [66]. Here we leave out the mathematical manipulations and just present the final $\epsilon_2(\omega)$ spectrum for a 2D band-edge under the influence of a Coulombic electron-hole interaction; that is

$$\epsilon_2(\omega) \propto \sum_{n=1}^{\infty} \frac{2}{(n-\frac{1}{2})^3}\,\delta[E+(n+\tfrac{1}{2})^{-2}] + \frac{\Theta(E)}{1+\exp(-2\pi/\sqrt{E})}, \qquad (3.1)$$

where $E = (\hbar\omega - E_g)/E_R$, $E_R = (\mu/\epsilon^2)Ry$ and $\Theta(E)$ is the step function. The strength of the interaction is determined by the effective dielectric constant ϵ and the reduced effective mass μ of the electron and hole. Consistent with the observed phonon screening of the impurity binding energy we use the static dielectric constant, $\epsilon = \epsilon_0 = 30$. In chapter 4 we argue that the effective hole mass is $m_h^* \simeq 2m_o$ where m_o is the electronic rest mass in vacuum. If we assume that the electron and hole have the same mass we find $\mu = m_h^*/2 \simeq m_o$. The exciton resonance is broadened by convoluting Eq. (3.1) with a Lorentzian distribution function with half-width 0.2 eV consistent with the observed data. In Fig. 3-2 we see the Wannier absorption spectrum does not have a sharp edge resonance above the band edge. Instead, the Coulombic interaction potential leads to enhanced absorption over a range of energies corresponding to ~ 10 times the exciton binding energy. A smaller half-width or a larger binding energy will not change this picture but rather create a well-defined bound-exciton resonance *below* the band edge. In short, a Coulombic interaction potential cannot account for the free electron-hole edge resonance we observe.

By assuming a short range interaction between electrons and holes we find a

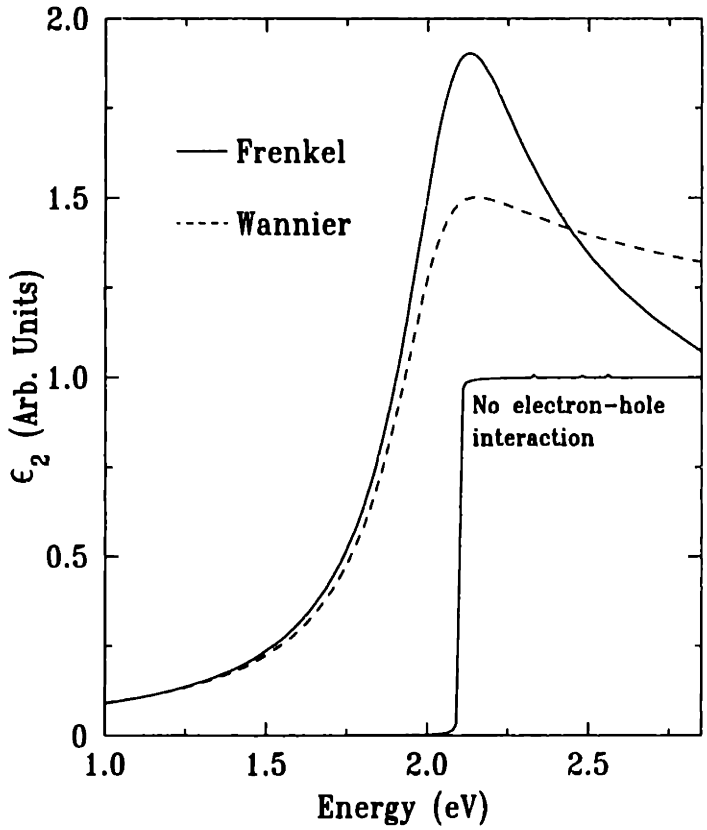

Figure 3-2: Calculated $\epsilon_2(\omega)$ spectra for a direct transition in 2D including Wannier[66] and Frenkel[64] exciton effects.

consistent description of the peak in ϵ_2. Such an interaction is appropriate for Frenkel excitons, like those in solid rare gases and molecular crystals, rather than for the Mott-Wannier variety which are spread out over many unit cells, as in conventional semiconductors. For the simplest model $V(\vec{r}) = -g\,\delta(\vec{r})$, where $\vec{r}$ is the separation of the electron and hole, the problem can be solved exactly[64]. The resulting dielectric function is

$$\epsilon_2(\omega) \propto |1 - g\,F(\omega)|^{-2}\, Im\, F(\omega), \tag{3.2}$$

where

$$F(\omega) = -\lim_{\eta \to 0} \int_0^\infty \frac{D(\omega')\,d\omega'}{\omega - \omega' + i\eta}\,. \tag{3.3}$$

Here $D(\omega)$ is the joint density of states, which in two-dimensions is $(\mu/\pi\,\hbar^2)$ above

the band gap. In the limit of $g = 0$ the dielectric function in Eq. (3.2) reduces to the usual result for interband transitions. The effect of the short range electron-hole interaction is to enhance the matrix elements near threshold. Equation (3.2) yields sharp resonances when $|1 - g\,F(\omega)|^2 \ll 1$.

In Fig. 3-2 we display the Frenkel excitonic band edge for a resonance with interaction strength $(\mu/m_o)g = 5.0\,\mathrm{eV\AA^2eV}$ and half-width $\eta = 0.2\,\mathrm{eV}$. This specific interaction strength is chosen since it provides a good fit to the data as we will find in Section 3.4. In contrast to the Coulombic potential, the short range interaction induces a sharp resonance *above* the band edge. This resonance can be understood as follows: In the limit of an extreme short-range electron-hole potential, most of the oscillator strength is exhausted by the transitions to the bound exciton. In two-dimensions the exciton binding energy for the δ-function potential is exponentially dependent on the inverse of the interaction strength, $\propto \exp[-\pi\hbar^2/g\,\mu]$. For the parameters used in Fig. 3-2, the binding energy is of order $\sim 0.02\,\mathrm{eV}$. With a lifetime broadening of order 10 times the binding energy, the oscillator strength of the bound exciton is transferred to an excitonic resonance state above the band gap. Such resonances have been previously seen in the continuum spectrum of solid rare gases[67]. In those systems sharp resonances are formed near the saddle points in the band dispersion where the density of states of the M_1 critical point emulates a 2D band edge. In La_2CuO_4 such a resonance appears just above the band edge due to the two-dimensionality of the charge-transfer excitation.

An obvious question concerns the nature and origin of a short range electron-hole interaction in La_2CuO_4. This will be the topic of Section 3.4.2.

3.2 The Temperature Dependent Edge Shift

We saw in Fig. 3-1 that the charge-transfer excitation peak in the in plane reflectivity spectrum broadens and shifts to lower energies with increasing temperature. A

detailed measurement of this behavior is displayed in Fig. 3-3 where we have plotted the shift of the in-plane reflectivity peak as a function of temperature. The peak position and the error bar are determined by fitting the corresponding reflectivity peak to a parabolic function. Cooling from 450K, the peak position increases linearly with decreasing temperature at a rate of 6.8×10^{-4} eV/K before it saturates at $T \sim 120$ K. This evolution is similar to that reported for $YBa_2Cu_3O_6$ powder samples[44]. We will in Section 3.4 show that the shift in the reflectivity peak translates directly to a shift of the absorption edge in the $\epsilon_2(\omega)$ spectrum. Thus the behavior reflects the temperature dependence of the effective charge-transfer excitation energy.

A softening of the effective band gap with increasing temperature is observed in covalent as well as ionic semiconductors. The dominant contribution in both systems comes from the electron-phonon coupling. An intuitive way of picturing such a mechanism is to first consider the valence electrons in the semiconductor as free. By introducing a periodic lattice potential $V(\vec{r})$ with periodicity $\vec{R}$ a gap opens up in the free-electron energy dispersion at the zone boundary $\vec{K} = 2\pi\vec{R}/R^2$. The size of the energy gap scales with the strength of the ionic potential, or more specifically with its Fourier components, $E_g \propto |\mathcal{V}(\vec{K})|^2$. The effect of the phonons is to introduce thermal vibrations of the ions around their equilibrium position. The effect of these thermal vibrations on the Fourier components is entirely contained in the Debye-Waller factor e^{-2W} where $2W$ is the average square displacement of the ion, $2W = <[\vec{K}\cdot\vec{u}]^2>$. Here $\vec{K}$ is the reciprocal-lattice vector. The thermal displacement must be much smaller than the lattice constant for most temperatures, $2W < 1$, and we can approximate the Debye-Waller factor by expanding the exponential to first order in the argument; that is

$$E_g \propto |\mathcal{V}(\vec{K})|^2 (1 - <[\vec{K}\cdot\vec{u}]^2>). \tag{3.4}$$

In an harmonic displacement potential the mean square ionic displacement $<u^2>$ is a linear function of the number of thermally excited phonon modes. For a phonon mode $\vec{q}$ with excitation energy $\hbar\omega_q$, the occupation number is given by the Bose-Einstein

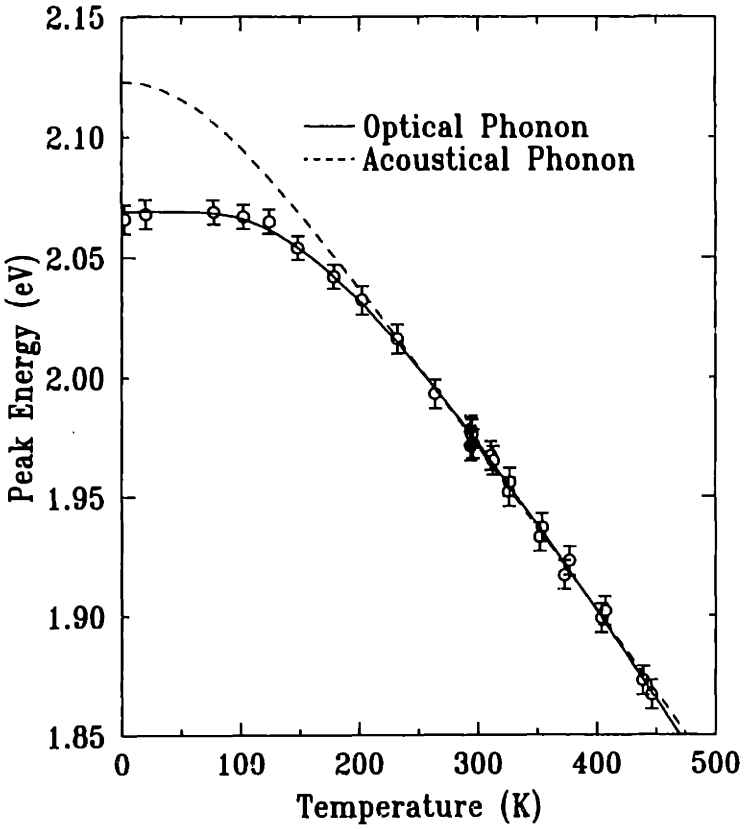

Figure 3-3: The temperature dependence of the charge transfer reflectivity peak. The solid and broken lines represent the best fits to an edge shift induced by optical and acoustic phonons, respectively.

distribution

$$n(\hbar\omega_q/k_BT) = \frac{1}{e^{\hbar\omega_q/k_BT} - 1}. \tag{3.5}$$

The sum goes then over all the phonon modes. If the edge shift is driven by the acoustical phonon modes, the phonon dispersion must be taken into account. By applying the Debye approximation for the phonon density of states, the acoustical contribution to the mean square lattice displacement can be solved exactly. The exact solution[74] can be found in appendix C. The temperature dependence is determined by the Debye temperature. At temperatures approaching the Debye temperature all acoustical phonon modes will be thermally excited with an occupation number increasing linearly with temperature as seen by expanding the exponential in Eq.

(3.5) to first order in $\hbar\omega_q/k_BT$. Thus at high temperatures this model yields a linear shift of the energy gap as observed for La_2CuO_4. In Fig. 3-3 we display the best fit for the exact solution found in appendix C using the Debye temperature of $\sim 400\,K$ extracted from heat capacity measurements in Ref. [75].

While this model[68] is successfully applied to covalent semiconductors for temperatures down to a few Kelvin, i.e. Si[69], the model is not able to describe the low temperature saturation observed in La_2CuO_4. The gradual saturation at low temperatures, preferred by the model, reflects the continuum of acoustical phonon modes below the Debye energy. The sharp saturation observed for La_2CuO_4 is typical for ionic insulators where the electron-phonon coupling is dominated by the optical phonons. These have little dispersion with an average excitation energy $\hbar\omega_0$. The edge shift in such a system will follow the Bose-Einstein distribution $n(\hbar\omega_0/k_BT)$. The best fit to the data, shown as a solid curve in Fig. 3-3, yields $\hbar\omega_0 = 0.043 \pm 0.004$eV. The absence of temperature dependence at low temperatures then reflects the freeze-out of the optical phonons. This scenario is supported by the large difference between the static dielectric constant $\epsilon_s \simeq 30$ and the optical frequency value $\epsilon_\infty = 5$ in La_2CuO_4[22] which implies that the electric dipole moment of some of the optical phonons is large enough for the optical phonons to dominate the electron-phonon interaction. The temperature dependent shift of the absorption edge, however, is the first direct evidence of the presence of such a coupling.

The above discussion is ill suited for ionic systems and serves only to distinguish between a dominant acoustical or optical phonon coupling. We will in the next section discuss the interaction between the charge carriers and the optical phonons in its proper contents - as formation of polarons.

3.3 Large Polarons - Their Self Energy and Lifetime

Excitation of an electron-hole pair in an ionic insulator is fundamentally different from that in covalent systems since the charge carrier polarizes and thereby distorts the neighboring ions. The induced polarization from the lattice distortion, in turn, acts like an electric field on the original charge carrier and lowers its energy; thus the charge carrier possesses a self-energy in the field. This self-energy is temperature dependent which, considering photoexcitation of an electron-hole pair, is reflected in a temperature dependent excitation energy. As the electron moves through the crystal, it carries along the distortion of the lattice. The electron together with the self-consistent polarization field can be thought of as a quasi particle, a polaron. Like any quasi particle, the polaron is associated with a quasi particle energy as well as a quasi particle lifetime. Mathematically these two different measures are treated as the real and imaginary part of a more general complex quasi particle energy dispersion, describing an electron dressed with a cloud of phonons through virtual emission and absorption processes. Physically it is often more intuitive to view the polaron as a "real" particle with an infinite lifetime which independently scatter from the optical phonons. It is important to realize, however, that the phonons which induce the polarization field and lower the energy of the electron are the same phonons that scatter the polaron.

The model describing a polaron depends on wheter the distortion of the lattice is limited to the immediate vicinity of the electron (*small polaron*) or wheter it extends over several lattice constants (*large polarons*). In Fig. 3-4 we have illustrated the lattice displacement associated with a large polaron. The main difference between small and large polarons is associated with the mass enhancement due to the accompanying lattice distortion. Translation of a small polaron between two neighboring lattice sites requires translation of the entire lattice distortion and the effective polaronic mass

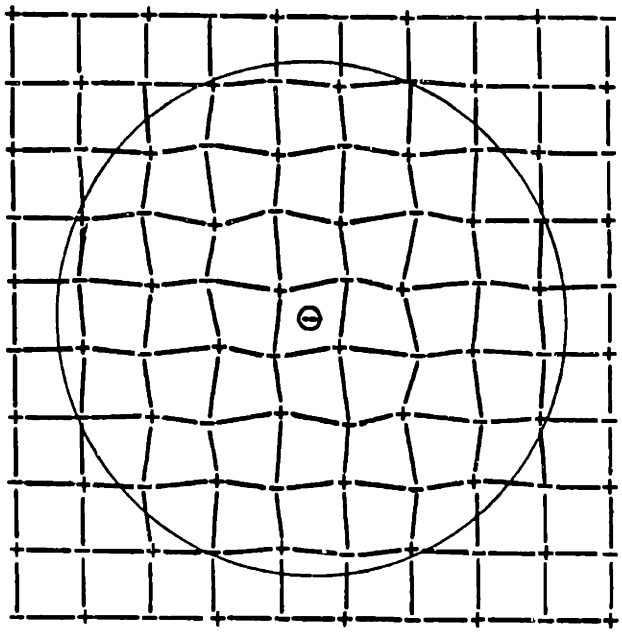

Figure 3-4: Schematic of a large polaron in an ionic lattice. The electron polarizes its surroundings by Coulomb interaction. The electron and the lattice deformation together constitute a quasi-particle.

becomes that of the ion[82]. With such a large mass, the width of the small-polaron band can become so small that it is physically more meaningful to consider the polaron as localized in the same sense that the core electrons in a crystal are localized. Thus small polarons are also referred to as self-trapped polarons. Translation of a large polaron between adjacent sites, on the other hand, requires only minor adjustments of the lattice distortion and large polarons behave as free particles scattered by optical phonons.

We will in this section only consider large polarons. Specifically we will calculate the polaronic self-energy and the scattering frequency. Since the lattice distortion spans an area larger than the lattice constant, the dielectric function is a good measure of the dielectric response of the lattice and we can view the lattice as a continuous dielectric medium rather than charged lattice points. We will later show that polaronic formation in La_2CuO_4 satisfies this approximation. Small polarons will be discussed in section 4.2.

3.3.1 The Polaronic Self-Energy

The mathematical treatment of the polaron problem is formulated as a quantum field theory where the induced polarization field interacts with the electron. The Hamiltonian has the general structure

$$\mathcal{H} = \mathcal{H}_{el} + \mathcal{H}_{lat} + \mathcal{H}_{int} \tag{3.6}$$

where $\mathcal{H}_{el}$ is the electronic component, $\mathcal{H}_{lat}$ the lattice component and $\mathcal{H}_{int}$ the electron lattice interaction. The basic problem in dealing with this Hamiltonian is that for ionic lattices the polarization field induced by the charge carrier is often too large to be ignored in calculating the eigenstates of $\mathcal{H}$ and should be considered in zeroth order. In the weak coupling limit the interaction is treated as a perturbation. For intermediate and strong coupling, variational methods are used. A solution covering the entire coupling range was developed by Feynman applying his path integral method[70]. A detailed discussion of any of these calculations are beyond the scope of this thesis. The interested reader is referred to a thorough review of polaron theories by J.Appel[71]. Instead we will try to motivate the final solutions by some illustrative back-of-the-envelope calculations.

The total polarization $\vec{P}(\vec{r})$ in an ionic lattice consists of two parts,

$$\vec{P}(\vec{r}) = \vec{P}_{ir}(\vec{r}) + \vec{P}_{opt}(\vec{r}), \tag{3.7}$$

the infrared component describing the displacement polarization of the ions, and the optical component reflecting the polarization of the electrons around each ion. The polarization field of interest for the electron-lattice interaction is the displacement polarization $\vec{P}_{ir}(\vec{r})$. If we can find an expression for $\vec{P}_{ir}(\vec{r})$ we can easily estimate the self-energy of the charge carrier in the dielectric medium and consequently the strength of the electron-phonon interaction. The simplest way to go about this is

to first find a relation between $\vec{P}_{ir}(\vec{r})$ and the electric displacement field $\vec{D}(\vec{r})$. The displacement field is convenient since it reflects the electric field from the true free electric charge and does not include contributions from the polarization induced charge distribution. To simplify the argument we will first consider the interaction between the dielectric medium and a static classical point charge e confined to a fixed position $\vec{r_o}$. In the static limit the electric displacement field is defined as

$$\vec{D}(\vec{r}) = \epsilon_o \vec{E}(\vec{r}) = \vec{E}(\vec{r}) + 4\pi \vec{P}(\vec{r}) \tag{3.8}$$

where $\vec{E}(\vec{r})$is the electric field vector and ϵ_o the static dielectric constant. By manipulating the definition of $\vec{D}(\vec{r})$ we can express the polarization vector $\vec{P}(\vec{r})$ as

$$4\pi \vec{P}(\vec{r}) = \left(1 - \frac{1}{\epsilon_o}\right) \vec{D}(\vec{r}). \tag{3.9}$$

Now consider the case where the point charge is oscillating around its center position $\vec{r_o}$ with a frequency much larger than the resonance frequency of the lattice displacement. In this case only the optical polarization will adiabatically follow the excess charge and the above relation is valid only for $\vec{P}_{opt}(\vec{r})$, thus

$$4\pi \vec{P}_{opt}(\vec{r}) = \left(1 - \frac{1}{\epsilon_\infty}\right) \vec{D}(\vec{r}) \tag{3.10}$$

where ϵ_∞ is the optical dielectric constant. In both of these limits the electric displacement field $\vec{D}(\vec{r})$ is identical reflecting the same free charge distribution. By subtracting $\vec{P}_{opt}(\vec{r})$ from $\vec{P}(\vec{r})$ we can now express the displacement polarization $\vec{P}_{ir}(\vec{r})$ as a function of the electric displacement field,

$$4\pi \vec{P}_{ir}(\vec{r}) = \left(\frac{1}{\epsilon_\infty} - \frac{1}{\epsilon_o}\right) \vec{D}(\vec{r}). \tag{3.11}$$

In order to calculate the displacement polarization $\vec{P}_{ir}(\vec{r})$ we are now only left with

deriving an expression for $\vec{D}(\vec{r})$. This is trivial since $\vec{D}(\vec{r})$ represents the electric field from a free point charge e at $\vec{r_o}$ and can be expressed as

$$\vec{D}(\vec{r}) = -\nabla \frac{e}{|\vec{r} - \vec{r_o}|} . \tag{3.12}$$

Since the lattice polarization does not make any contribution to $\vec{D}(\vec{r})$, it follows from Eq. (3.8) that $-4\pi\vec{P}_{ir}(\vec{r})$ represents the electric field established by the displaced ions. By combining Eqs. (3.11) and (3.12) we can now express the displacement electric field in terms of an electrostatic potential as $-4\pi\vec{P}_{ir}(\vec{r}) = -\nabla\,\Phi(\vec{r})$ where

$$\Phi(\vec{r}) = -\left(\frac{1}{\epsilon_\infty} - \frac{1}{\epsilon_o}\right)\frac{e}{|\vec{r} - \vec{r_o}|}. \tag{3.13}$$

Here $\Phi\ \vec{r})$ represent the electrostatic potential at a position $\vec{r}$ due to the point charge induced lattice displacement. We see that the induced electric field corresponds to that of an image point charge of opposite sign at position $\vec{r_o}$. The point charge and the image point charge interact creating a negative self energy. To find the total electrostatic potential experienced by the surroundings we must add the contribution from the free charge $e/(\epsilon_\infty|\vec{r} - \vec{r_o}|)$. This yields a total electrostatic potential of $e/(\epsilon_o|\vec{r} - \vec{r_o}|)$ as expected.

Now consider a point charge moving through the lattice with a fixed velocity v. An ion is displaced as in the static case only if its distance from the approaching point charge is sufficiently larger than v/ω_o. The reason is that it takes a time of order $1/\omega_o$ to displace an ion. Below this distance the point charge passes so quickly that its action on the ion can be considered as a shock, exciting oscillations after it has past. In this case the electrostatic potential at the position of the moving point charge is of the order

$$\sim -\left(\frac{1}{\epsilon_\infty} - \frac{1}{\epsilon_o}\right)\frac{e\,\omega_o}{v} \tag{3.14}$$

where v/ω_o corresponds to the minimum distance between the point charge and a

displaced ion.

In a real system we operate with electrons and not classical point charges. A quantum particle satisfies Heisenberg's uncertainty principle where the uncertainty in spatial position δr and in wave-vector δk_{el} is related through $\delta r\, \delta k_{el} \geq 1$. For traditional Bloch electrons the wave-vector is a good quantum number. Consequently the electronic state is extended over the entire system. For a polaronic quasi particle the electron interacts with the self-consistent displacement field by emitting phonons. For each emission of a phonon $\vec{q}$, the electron recoils to $\vec{k}_{el} - \vec{q}$. The wave vector of the electron is associated with an uncertainty $\delta k_{el} \sim q$ and is not any longer well defined. Conservation of energy requires that $k_{el}^2 = (\vec{k}_{el} - \vec{q})^2 + 2m_h^* \omega_o/\hbar$ which yields $q \geq \sqrt{2m^* \omega_o/\hbar}$. This uncertainty in the wave vector confines the quasiparticle in real space with a spatial smearing of order

$$\delta k_{el}^{-1} \sim \sqrt{\frac{\hbar}{2m_h^* \omega_o}} \equiv a_p. \tag{3.15}$$

The quantity a_p is referred to as the polaron radius and is a measure of the spatial smearing of the electronic charge as well as the size of the lattice distortion. We will in chapter 4 argue that the rigid band mass for the hole is $m_h^* \sim 2\, m_o$. With an average phonon excitation energy of $\hbar\omega_0 = 0.043\,\mathrm{eV}$ we find a polaron radius of $a_p \sim 7\,\text{Å}$. This is 1.5 times the Cu spacing and justifies the dielectric approximation.

At distances much larger than both a_p and v/ω_o the induced displacement potential is given by the classical expression (3.13). At short distances, however, there are now two competitive effects which prevent the potential from falling below a certain value: the uncertainty in the position, and the minimum distance to a displaced ion due to the effect of velocity. We will expect that the mechanism which leads to the larger critical distance decides the order of magnitude of the potential inside the displaced region. For fast moving electrons where $v/\omega_o \gg a_p$, the strength of the interaction potential is determined by v/ω_o. In the limit of slow moving electrons,

however, the two competing effects are related since the velocity of the electron is determined by $\delta v = \hbar\,\delta k_{el}/m_h^*$ yielding $v/\omega_o \sim \hbar\,\delta k_{el}/m^*\omega_o \sim 2\,a_p$. Thus, both effects yield an effective cut-off length of order the polaronic radius. For slow moving polarons the electron-lattice interaction energy is then given by multiplying $\Phi(\vec{r})$ with e and replacing $|\vec{r} - \vec{r_o}|$ with a_p. This gives us an interaction energy of order

$$\mathcal{H}_{int} \sim -\left(\frac{1}{\epsilon_\infty} - \frac{1}{\epsilon_o}\right)\frac{e^2}{a_p}. \tag{3.16}$$

To obtain the net interaction energy we must add the energy required to polarize the lattice as well as the change in the kinetic energy of the electron. We will not discuss these terms but rather state that the exact net polaron self energy is half of the above value. The quasi particle energy $E(\vec{k})$ at zero temperature for an electron with effective mass m^* and polaronic wave vector $\vec{k}$ is, to second order in k, given as

$$E(\vec{k}) = E^o(0) - \alpha_p\,\hbar\omega_0 + \frac{\hbar^2\,k^2}{2\,m^{**}} \tag{3.17}$$

where $m^{**} = (1 + \alpha_p/6)m^*$ with the polaron coupling constant defined as

$$\alpha_p \equiv \frac{1}{2}\left(\frac{1}{\epsilon_\infty} - \frac{1}{\epsilon_o}\right)\frac{e^2}{a_p\,\hbar\omega_0} = \frac{1}{2}\frac{e^2}{\hbar\omega_0}\left(\frac{1}{\epsilon_\infty} - \frac{1}{\epsilon_s}\right)\sqrt{\frac{2\,m\,\omega_0}{\hbar}}. \tag{3.18}$$

The polaron constant is the ratio of the self-energy to the phonon energy or, approximately, the number of phonons associated with the lattice distortion. From the quasi-particle energy dispersion it is evident that the polaron behaves like a free particle with an increased mass m^{**} and a creation energy reduced by $\alpha_p\,\hbar\omega_0$. The wave vector $\vec{k}$ must not be confused with the electronic wave-vector. The wave vector of the electron is not any longer a good quantum number. Here, $\hbar\vec{k}$ represents the momentum of the polaronic center-off-mass.

The energy dispersion in Eq. (3.17) is found to be valid for electron-phonon interactions of both weak ($\alpha_p < 1$) and intermediate ($1 < \alpha_p < 7 - 8$) strength, applying

both perturbative and variational methods. In the language of second order perturbation theory the binding energy $\alpha_p \hbar\omega_0$ reflects the effect of emitting α_p phonons. The matrix element for creating a phonon with wavenumber q is $<n_q|n_q+1>=\sqrt{n_q+1}$, where n_q, given in Eq. (3.5), is the number of thermally excited phonons with energy $\hbar\omega_q = \hbar\omega_0$. The probability for phonon emission scales with the square of the matrix element. Thus, within second order perturbation theory the temperature dependent polaron self-energy energy is expressed as[72]

$$E(0) - E^o(0) = -\alpha_p \hbar\omega_0 (n(\hbar\omega_0/k_B T) + 1). \tag{3.19}$$

We can now derive the minimum energy required to create an electron-hole pair across the band gap by subtracting the maximum energy of a hole polaron in the valence band from the minimum energy of an electron polaron in the conduction band. For simplicity, we assume that the electron and the hole have the same mass and hence the same α_p; thus we find

$$E_g(T) = E_g^0 - 2\,\hbar\omega_0\,\alpha_p\,(n(\hbar\omega_0/k_B T) + 1), \tag{3.20}$$

where $E_g^o = E_c^o(0) - E_v^o(0)$ is the rigid band gap. The shift of the band edge is due to the polaronic binding energy and scales with the occupation number of the interacting phonon modes in agreement with our discussion in the Section 3.2.

3.3.2 Polar Optical Scattering

The polaron is not only characterized by a quasi particle energy but also by a quasi particle lifetime. At zero temperature the electron is dressed by α_p phonons of frequency ω_o. The scattering frequency is then $1/\tau_o \sim \alpha_p\omega_o$. While this is true for slow moving polarons, this expression must be modified for fast moving polarons with $v/\omega_o \gg a_p$. In this limit the polaronic self-energy is not determined by the

polaronic radius, but by the effect of velocity effectively freezing all ions within a radius v/ω_o of the electron. Since the polaronic coupling constant is inversely proportional to the polaronic radius, the effective polaronic coupling constant for fast moving electrons scales like $\alpha_p(a_p\omega_o/v)$. The average scattering frequency is then $1/\tau_o \sim \alpha_p\omega_o(a_p\omega_o/v) = \alpha_p\omega_o\sqrt{\hbar\omega_0/E_{kin}}$, where E_{kin} is the kinetic energy of the moving polaron. Slow moving polarons with a kinetic energy $E_{kin} = \hbar^2 k^2/2m^* \ll \hbar\omega_0$ can only absorb a phonon and the scattering frequency scales like $n(\hbar\omega_0/k_BT)$. Fast moving polarons with $E_{kin} \gg \hbar\omega_0$, on the other hand, can both absorb and emit phonons and scales like $(2\,n(\hbar\omega_0/k_BT)+1)$. Within some numerical factors we have now derived the temperature and energy dependence of the scattering frequency. A proper perturbative treatment[73] yields

$$\begin{aligned} \frac{1}{\tau} &= \frac{2}{3}\alpha_p\,\omega_o\,n(\hbar\omega_0/k_BT) && E_{kin} \ll \hbar\omega_0 \\ \frac{1}{\tau} &= \alpha_p\,\omega_o\sqrt{\frac{\hbar\omega_0}{E_{kin}}}\,(2\,n(\hbar\omega_0/k_BT)+1) && E_{kin} \gg \hbar\omega_0. \end{aligned} \tag{3.21}$$

In the neighborhood of the resonance $E_{kin} \sim \hbar\omega_0$ the situation is more complicated and perturbation theory fails.

In describing the behavior of the charge-transfer band edge we are interested in the decay rate $\gamma(T)$ for the correlated electron and hole pair in the continuum. We assume that this decay rate is the sum of the individual polaron relaxation rates. This gives

$$\gamma(T) = 2^{3/2}\,\omega_0\,\alpha_p\sqrt{\frac{\hbar\omega_0}{2E_{kin}}}\,(2\,n(\hbar\omega_0/k_BT)+1) \tag{3.22}$$

where $2E_{kin}$ denotes the total kinetic energy of the electron and hole, that is, $\hbar\omega - E_g(T)$. This expression is only valid for $E_{kin} > \hbar\omega_0$. However, the total oscillator strength of the undressed ϵ_2 spectrum within $2\,\hbar\omega_0 \simeq 0.09\,\mathrm{eV}$ of the band edge is

small enough that this restriction is unimportant.

3.4 Modeling the Charge-Transfer Spectrum

In Figure 3-5 we display the experimental in-plane dielectric function for four temperatures together with the predictions of our model, Eq. (3.2). We emulate the effect of the electron-phonon interaction phenomenologically by introducing the lifetime broadening into the dielectric function, replacing η in Eq. (3.3) with $\gamma(T)/2$, Eq. (3.22), and shifting the band edge according to $E_g(T)$, Eq. (3.20). With $\hbar\omega_0$ fixed at 0.043 eV, the model has four adjustable parameters: $(\mu/m_o)\,g$, α_p, E_g^0 and the overall scale factor. Only two of these parameters, $(\mu/m_o)\,g$ and α_p, control the shape of $\epsilon_2(\omega)$ including its temperature dependence. To test the model, we first fit $\epsilon_2(\omega)$ at the lowest temperature, T=122K, with all four parameters adjustable. The best fit for T=122K gives $(\mu/m_o)\,g = 5.0\,\mathrm{eV\AA}^2$, $\alpha_p = 5.7$ and $E_g^0 = 2.6\,\mathrm{eV}$. As seen in Fig. 3-5, the model describes the measured $\epsilon_2(\omega)$ at T=122K quite well. The dashed lines for T=295K, 378K and 447K in Fig. 3-5 are calculated from our model with the parameters fixed at their T=122K values. With the polaron coupling constant determined by the broadening at T=122K the theory predicts the change of the peak shape and its position as well as its overall strength all the way up to T=447K. Clearly, the theory works very well, indeed much better than one might reasonably expect given the simple form and the small number of adjustable parameters.

We find, consistent with earlier workers, that $\epsilon_\infty \simeq 5$ for photon energies below $\sim 1.5\,\mathrm{eV}$. With $\alpha_p = 5.7$ and $\epsilon_s = 30$[22] one finds from Eq. (3.18) a bare mass of $\sim 3.6\,m_e$. By including the polaron enhancement of ~ 2 we find a total mass of $\sim 7\,m_e$. The bare mass is almost a factor of two larger than the value Chen *et al.*[22] extract from the binding energy and the localization length of doping induced carriers as will be discussed in chapter 4. A proper 2D treatment of the electron-phonon coupling and inclusion of other contributions to the zero temperature line-width such

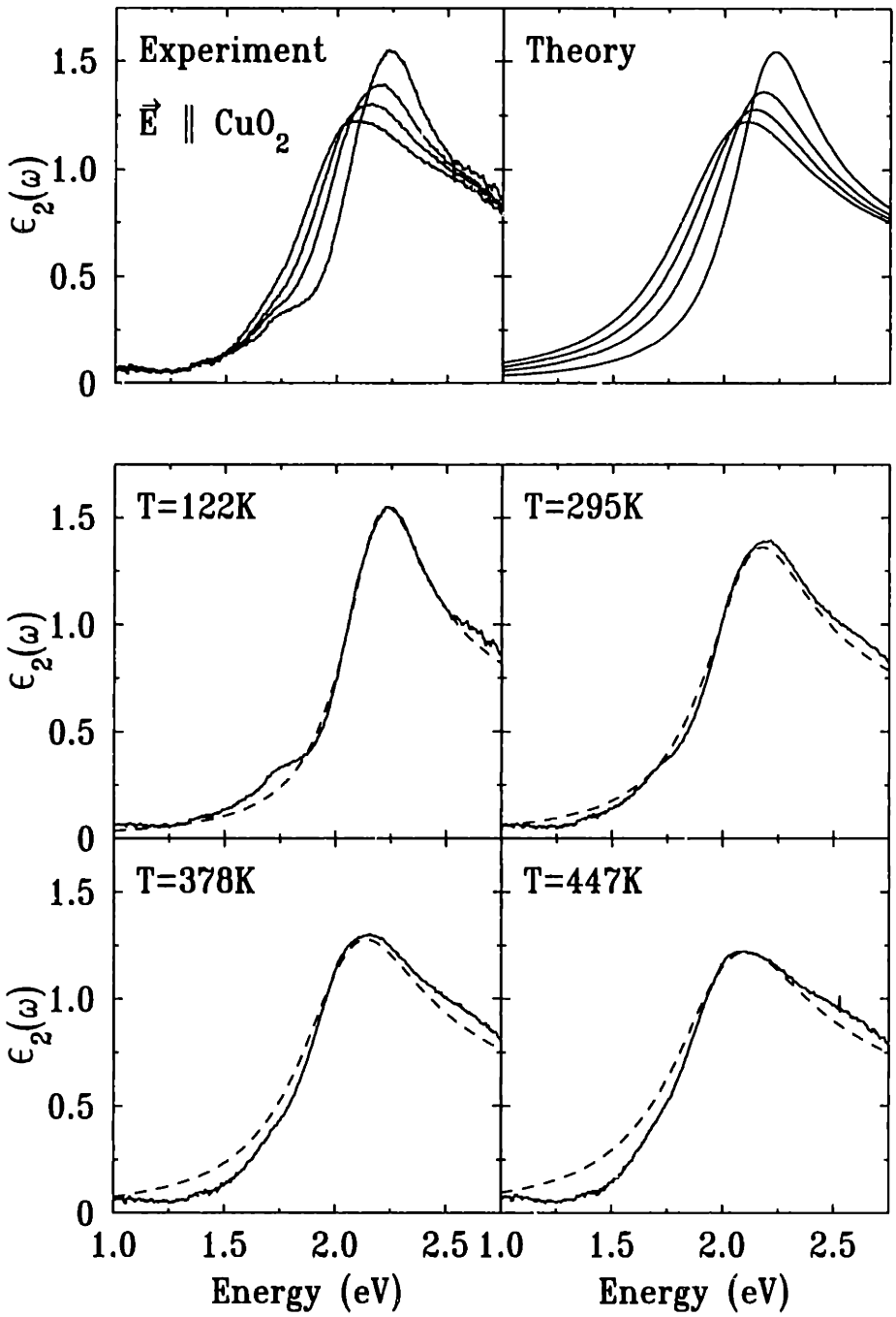

Figure 3-5: The in-plane $\epsilon_2(\omega)$ for four different temperatures together with the best fit to the data using the model and the parameters discussed in the text. All four temperatures are shown in the upper panel; theory and experiment are compared for individual temperatures in the lower panel.

as elastic scattering may reduce this discrepancy. 3D effects are not expected to contribute to the broadening because of the absence of any charge-transfer feature in the out-of-plane spectrum (see Fig. 3-1).

The parameter $E_g^0 = 2.6\,\mathrm{eV}$ represents the bare band gap. The effective band gap differs from E_g^0 by the total electron and hole polaron self energy. Inserting the appropriate quantities into Eq. (3.20) at $T = 0\,\mathrm{K}$ gives an energy gap for creating electron and hole polarons of $E_g(0) = 2.1\,\mathrm{eV}$, in excellent agreement with the value $2.0 \pm 0.1\,\mathrm{eV}$ from the photoconductivity[45].

3.4.1 The electron-phonon coupling

An optical mode in an ionic crystal is accompanied by electric dipoles due to oscillating ions within each of the N unit cells. The dipole moment $\vec{P}(\vec{r}_n)$ for the nth unit cell at position $\vec{r}_n$ is proportional to $e\,\vec{u}(\vec{r}_n)$ where e is the electronic charge and $\vec{u}(\vec{r}_n)$ is the ionic displacement associated with the vibrational excitation. Each oscillating dipole gives rise to a dipolar potential for an electron at position $\vec{r}$. The corresponding interaction potential energy is given as

$$\mathcal{H}_{int}(\vec{r}) \propto \sum_n \frac{e\,\vec{u}(\vec{r}_n)\cdot(\vec{r}_n - \vec{r})}{|\vec{r}_n - \vec{r}|^3} \tag{3.23}$$

where the sum goes over all the N unit cells. The lattice displacement $\vec{u}(\vec{r}_n)$ can be Fourier-expanded in terms of the generalized coordinate $\vec{u}_{\vec{q}}$ for a vibrational mode with wave-vector $\vec{q}$:

$$\vec{u}(\vec{r}_n) = N^{-1/2} \sum_{\vec{q}} \vec{u}_{\vec{q}}\, e^{i\vec{q}\cdot\vec{r}_n}. \tag{3.24}$$

By Fourier-expanding Eq. (3.23), the interaction potential $\mathcal{H}_{int}$ can be expressed as

$$\mathcal{H}_{int}(\vec{r}) \propto \sum_{\vec{q}} \frac{e\,\vec{u}_{\vec{q}}\cdot\vec{q}}{q^2}\, e^{i\vec{q}\cdot\vec{r}} \tag{3.25}$$

where the sum goes over the N phonon modes.

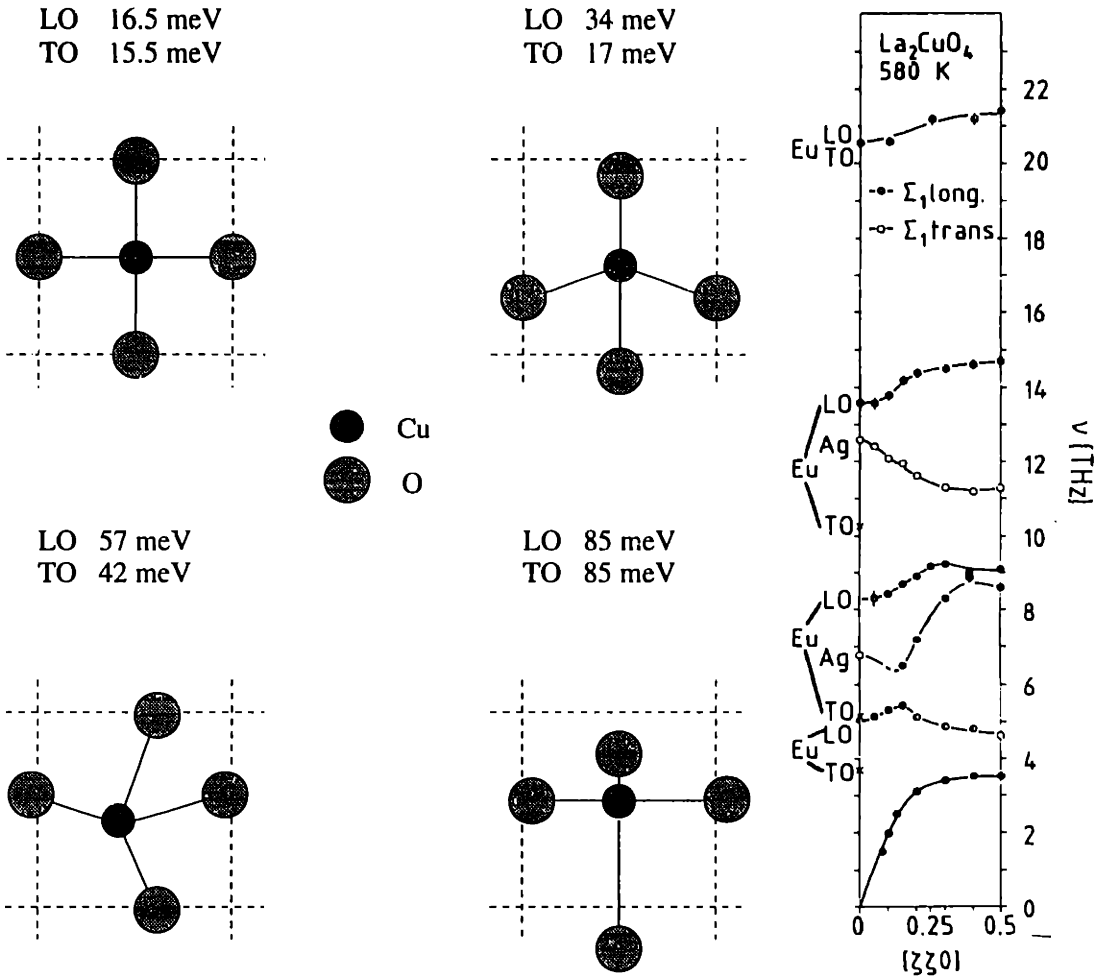

Figure 3-6: **(a)** The lattice displacement for the zone-center E_u modes calculated for tetragonal La_2CuO_4[76]. **(b)** Experimental phonon dispersion curves of Σ_1 phonons for tetragonal La_2CuO_4 determined by inelastic neutron scattering[77]. The excitation energies in panel (a) correspond to the zone-center values in panel (b).

The the electron-phonon interaction potential in Eq. (3.25) is zero if the dipole moment $\vec{u}_{\vec{q}}$ and the phonon wave-vector $\vec{q}$ are perpendicular. Thus only longitudinal phonon modes $\vec{u}_{\vec{q}} \propto \vec{q}/q$ couple to the charge carriers with a strength proportional to $1/q$. Since the photoexcited electron and holes are confined to the CuO_2 plane, they can only interact with LO phonons propagating parallel to the planes, that is the LO E_u modes. In tetragonal La_2CuO_4 only four optical phonon modes have E_u symmetry. In Fig. 3-6 we show the lattice displacement for the zone-center E_u modes as calculated by Cohen *et al.*[76]. We also display the experimental phonon dispersion

curves of LO E_u phonons for tetragonal La_2CuO_4 measured by Pintschovius *et al.*[77] using inelastic neutron scattering. The lowest energy mode involves in-plane sliding of the La and apical O with negligible displacement of atoms in the CuO_2 plane. The highest energy mode is a Cu-O bond-stretching mode while the remaining two are both Cu-O bond-bending modes.

The phonon dispersion curves reveal a large LO-TO splitting at the zone center for both bond bending modes. Such splittings are typical for ionic insulators where the longitudinal excitation must overcome the electrostatic restoring force induced by the ionic displacement as well as the elastic component. Thus, the size of the splitting is a measure of the strength of the induced dipole moment. An other way to reach the same conclusion is through the Lyddane-Sachs-Teller relation $(\epsilon_l/\epsilon_h) = (\omega_{lo}/\omega_{to})^2$. Here ϵ_h and ϵ_l are the high and low frequency limits of the dielectric resonance associated with a specific phonon mode. The difference between these values is directly proportional to the polarizability of the lattice vibration. Thus the Lyddane-Sachs-Teller relation relates the strength of the polarizability to the difference between the longitudinal ω_{lo} and transverse ω_{to} optical phonon frequencies at the zone center.

The measured LO-TO splittings indicate that the charge carriers primarily couple to the two Cu-O bond-bending modes at 0.034 eV and 0.057 eV respectively. Our measured $\hbar\omega_0 = 0.043\,\text{eV}$ is consistent with a weighted average of these two frequencies. Indeed, by describing the shift of the reflectivity peak in Fig. 3-3 as a contribution from two phonon bands with energies 0.034 and 0.057 eV, respectively, the best fit to the data is obtained with the two bands carrying approximately equal weight. This fit is indistinguishable from the best one-component fit shown in Fig. 3-3. As we have demonstrated above, a description assuming coupling to this one effective phonon mode provides an excellent fit to all the data.

Complimentary evidence for a Fröhlich coupling between the E_u symmetry phonon modes and the charge carriers is provided by Heyen *et al.*[78]. In a resonant Raman

study on insulating $YBa_2Cu_3O_6$ they find that when the laser energy is tuned to the charge-transfer energy, four of the total of six infrared-active LO phonons of E_u symmetry become Raman active. Both the strength and the selection rules are consistent with forbidden Raman scattering due to Fröhlich electron-phonon interaction. The Fröhlich interaction between LO E_u phonons and photoexcited electron and holes hybridizes even symmetry components into the odd symmetry phonon wavefunction, making the E_u phonons weakly Raman active. Heyen *et al.* point out that the same effect is observed in La_2CuO_4 by Ohana *et al.*[79] but was neither noticed nor interpreted.

Additional information about the electron-phonon interaction is provided by photo-induced optical absorption measurements. Photo-induced absorption and bleaching of infrared active phonon modes is observed in both La_2CuO_4[49, 50, 43], Nd_2CuO_4[43] and $YBa_2Cu_3O_6$[50, 80]. Such behavior implies the existence of structural deformation around the photoexcited carriers, indicative of an electron-phonon coupling. Ye *et al.*[80] have reported the most comprehensive study where all the photo-induced vibrational excitations in $YBa_2Cu_3O_6$ are identified by comparison with direct transmission and Raman spectra. The observed bleaching modes correspond to E_u infrared modes, while the photo-induced absorption modes correspond to Raman modes in $YBa_2Cu_3O_6$ and infrared modes in $YBa_2Cu_3O_7$. Thus, of the infrared active phonons in $YBa_2Cu_3O_6$, only modes of E_u symmetry are found to be sensitive to photoexcitation. Moreover, all six E_u modes display photo-induced bleaching. Ye *et al.* suggest that photoexcited holes form mobile polarons within the CuO_2 layer, screening the E_u vibrations.

3.4.2 The short-range electron-hole interaction

To understand the origin of the short range electron-hole interaction we describe the charge-transfer from copper to oxygen using the language of the extended Hubbard model. The effective Hamiltonian for the latter model[39] includes two kinds of

interaction between a hole on a Cu site and one on a neighboring O site. The first is the Coulomb interaction V, and the second is the exchange energy $K_{eff}\,\vec{s}\cdot\vec{S}$ where $\vec{s}$ and $\vec{S}$ are the spins of the holes on the oxygen and copper sites, respectively, and K_{eff} is the effective antiferromagnetic exchange. The fundamental difference between a nearest neighbor transfer and a transfer to an oxygen site farther away is that in the latter case the hole on the oxygen site has two neighboring copper holes while for the nearest neighbor transfer it has only one. Thus, to first order, the energy difference between a long range and a nearest neighbor charge transfer equals the difference in the total interaction energy between the neighboring Cu and O holes, i.e. $V + K_{eff}$. The effective interaction potential of an electron and hole can therefore be approximated by a potential well centered around the central copper ion with a depth of $\sim V + K_{eff}$ and a radius of order the Cu-O spacing. With an effective radius of $\sim 2\,\text{Å}$ and a depth of $\sim 1.5\,\text{eV}$ (see Ref. [39]) we estimate the integrated potential to be $\sim 18\,\text{eV}\text{Å}^2$, the same order of magnitude as the value of $(\mu/m_e)\,g$ needed to fit the charge transfer line shape. The observation of a bound exciton at $\sim 1.75\,\text{eV}$ is consistent with this picture. A 2D potential well of radius $\sim 2\,\text{Å}$ and depth $1.5\,\text{eV}$ supports a bound state with a binding energy of $\sim 0.2\,\text{eV}$. Of course, the energy of the exciton is sensitive to the details of the potential.

Chapter 4

Photo-Ionization of Polaronic Impurities

From transport measurements on lightly oxygen doped La_2CuO_{4+y}[22, 19] we know that the excess holes are localized in shallow impurity states. The presence of such impurity states requires a photo-ionization band in the absorption spectrum with a strength determined by the impurity density. In Chapter 3 we saw that photo-induced electrons and holes are coupled with intermediate strength to optical phonon modes and form large polarons. The electron-phonon interaction does not discriminate between localized and free carriers and we expect the doping induced localized holes to form polarons as well. We will in this chapter demonstrate that the excitation spectrum and temperature dependence of the lowest-energy mid-infrared absorption band is consistent with photo-ionization of such a large polaronic impurity state. We start out in Section 4.1 reviewing the evidence for impurity absorption: transfer of spectral weight between free carrier conductivity and a photo-ionization band of impurity-bound carriers. The large difference between the optical 0.13 eV and thermal 0.035 eV ionization energy indicates that the impurity states are stabilized by a lattice distortion. In Section 4.2 we discuss the effect of localization on the electron-phonon coupling and show that in La_2CuO_{4+y} the localized polarons are still large.

In section 4.3 we discuss photo-ionization of localized polarons in detail and develop a model for the 0.13 eV absorption band. We apply this model to the reflectivity spectra in section 4.4 and show that the line shape as well as the temperature dependence is consistent with absorption from a polaronic impurity state. We close in section 4.5 by discussing if this mechanism can explain the $0.1 - 0.2\,\mathrm{eV}$ mid-infrared band observed in both absorption and photo-induced absorption spectra for a variety of lightly oxygen doped copper oxides.

4.1 Evidence for Impurity Absorption

In Fig. 4-1(a) we display the reflectivity spectra for undoped and lightly doped La_2CuO_{4+y}. The out-of-plane spectrum shows no structure except a sharp reduction in the reflectivity for $\hbar\omega \leq 0.19\,\mathrm{eV}$. The decreasing reflectivity reflects the decreasing real dielectric function associated with infrared active optical phonons near 0.08 eV[35]. The in-plane reflectivity spectrum for the undoped crystal is almost identical to the out-of-plane spectrum. For the doped crystal, however, the in-plane reflectivity spectrum is enhanced throughout the region from 0.1 to 0.75 eV with a maximum at 0.1 eV. The strength of the 0.1 eV reflectivity peak decreases rapidly as the temperature increases. The mid-infrared absorption processes are clearly connected with the introduction of doping-induced carriers. Furthermore, only the in-plane reflectivity spectrum changes with doping. Thus, the mid-infrared absorption processes are confined to the CuO_2 sheets.

The reflectivity data were transformed to give the complex dielectric function using the Kramers-Kronig relations as discussed in section 2.2. In Fig. 4-1(b) we display the imaginary part of the dielectric function, $\epsilon_2(\omega)$. Two separate absorption peaks are clearly distinguished, a broad feature centered at $\sim 0.5\,\mathrm{eV}$ and a more narrow one at $\sim 0.13\,\mathrm{eV}$. It is evident that only the 0.13 eV absorption band is strongly T-dependent. In this chapter we will only consider the low-energy absorption band.

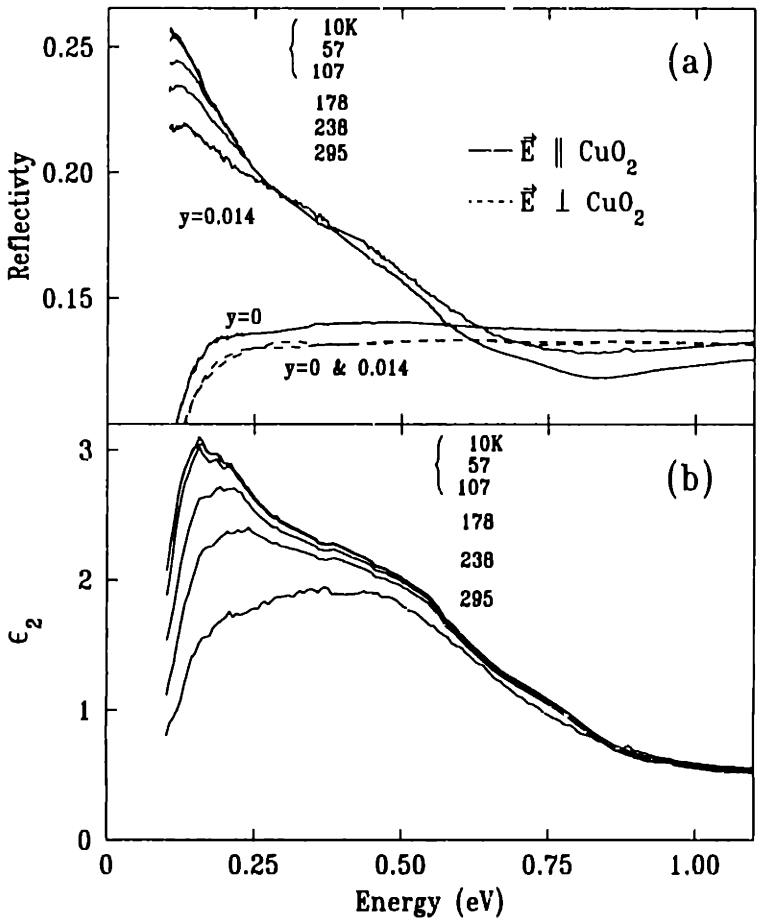

Figure 4-1: (a) Reflectivity spectra of undoped and oxygen doped La_2CuO_{4+y} crystals with $T_N = 322\,K$ and $250\,K$ respectively. The in-plane spectra for the doped sample are indistinguishable below $\sim 100\,K$. Above $0.3\,eV$ they are only displayed at $10\,K$ and $295\,K$ with the latter having the higher reflectivity. (b) In-plane $\epsilon_2(\omega)$ for the oxygen doped sample.

The $0.5\,eV$ excitation will be discussed in chapter 5.

The decrease of the oscillator strength in the $0.13\,eV$ band between 100 and $300\,K$ coincides with an increase of the free carrier density as evinced by the temperature dependence of the Hall coefficient displayed in Fig. 1-4. For a sample with $T_N = 250\,K$ the number of free carriers reaches 0.004(1) per Cu ion at $300\,K$. Because of a large contribution from hopping conductivity, it is not possible to determine the binding energy of the impurities accurately for this sample. However, a sample with $T_N = 310\,K$ has negligible hopping conductivity. For the latter, the Hall density increases with

T as $\exp[-E_b/k_BT]$ for $40 < T < 300\,\mathrm{K}$, giving the binding energy $E_b = 0.035\,\mathrm{eV}$. By calculating the oscillator strength as given by Eq. (1.1) at 10 K and 295 K we find that the effective number of carriers involved in the 0.13 eV absorption decreases by $N^*_{eff}m_o/m^* = 0.0023(5)$. Before we can compare this value with the increase in the Hall density we must first determine the appropriate effective mass. The polaronic mass enhancement only applies to excitations involving translation of the polaron center-of-mass, the Drude conductivity. For any other electronic excitations the bare band mass applies. Uchida *et al.*[35] show that total number of carriers involved in the entire charge-transfer excitation in undoped La_2CuO_4 is $N^*_{eff} \simeq 1$ per Cu ion when $m^* \simeq 2m_o$. This mass is also consistent with a Coulombic potential model of the bound state[22]. Thus the decrease in the spectral weight of the 0.13 eV band, $N^*_{eff} \simeq 0.045(10)$ per Cu ion, is the same as the increase in spectral weight of the dc conductivity. Moreover, we will in the next section show that the detailed temperature dependence of the 0.13 eV band is predicted by that of the Hall density. Together this provides strong evidence that the 0.13 eV band results from photo-ionization of the impurities.

The optical excitation energy $\sim 0.13\,\mathrm{eV}$ is almost a factor 4 larger than the thermal activation energy $E_b = 0.035\,\mathrm{eV}$ measured from the Hall effect. This situation is quite common in insulators in which the charge carrier, bound to the impurity, is strongly coupled to the optical phonons, causing a lattice distortion around the impurity site. During optical ionization of the impurity, the lattice is usually assumed to be frozen, obeying the Frank-Condon principle. Thus, the charge carrier must overcome its polaronic binding energy in addition to the impurity binding energy in order to delocalize. During thermal activation, by contrast, the lattice has time to relax, so only the impurity binding energy must be overcome.

We will in the next three sections discuss these ideas in much more detail and specifically consider the absorption spectrum associated with photo-ionization of a localized polaron.

4.2 Localization and the Electron-Phonon Coupling

To discuss the effect of localization on the electron-phonon coupling it is important to consider not only the long-range Fröhlich interaction with the optical phonons but also the additional contribution from the short-range deformation interaction with the acoustical phonons. The short-range interaction is important since it may cause the localized charge carriers to form small polarons.

In Fig. 4-2 we show the phase diagram for polaron formation of charge carriers under influence of both long- and short-range electron-phonon coupling as presented in Ref. [81]. The strength of the long (short) range interaction is expressed in terms of the coupling constants $g_{l(s)} = E_{pol}^{l(s)}/B$ where B is electronic band width and $E_{pol}^{l(s)}$ is the polaronic binding energy associated with the long (short) range electron-phonon interaction. The large and self-trapped polaronic states are denoted by F and T, respectively. The solid line, across which the stable state changes discontinuously from F to T to, starts from the g_s-axis and terminates at a critical point without reaching the g_l-axis. The only trigger for the F-T discontinuity is the short range interaction with the acoustical phonons while the long-range interaction with optical phonons dominates in the T-state.

It should be noted that the large Fröhlich polaronic state of the weak and intermediate ($\alpha_p < 3\pi$) through strong ($\alpha_p > 3\pi$) coupling regime, corresponds to the F state of the phase diagram along the g_l axis. Both the weak and strong coupling large polaron should be well distinguished from the T-state. The latter wants to be as small as possible while the former has an optimum radius which is usually much larger than the the lattice constant. In other words, the small polaron is not simply the strong coupling limit of the Fröhlich polaron. The real T-state, which is well distinguished from and can coexist with the F-state, is triggered by the short-range interaction with acoustical phonons, although the optical phonons also make a

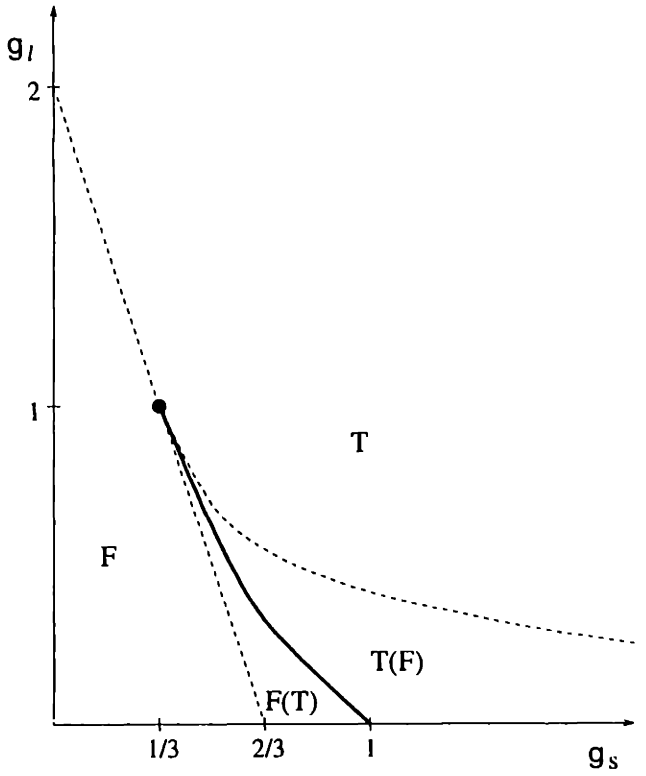

Figure 4-2: Phase diagram for the stable and metastable (in parentheses) states where g_s and g_l denote the strength of the short and long range electron-phonon interaction, respectively. Large polarons are denoted by F and small polarons by T(from Ref. [81]).

comparable contribution to this state.

The polaronic phase diagram in Fig. 4-2 applies to free as well as impurity trapped charge carriers. The only difference between the free and localized case is the effective coupling strength. It turns out that both the long- and short-range lattice interaction increases with localization. This effect can be understood as follows: The charge carriers can only couple to phonon modes with wavelengths equal to or longer than the effective radius of the charge carrier. The smaller the radius, the larger the number of accessible phonon modes and the stronger the electron-phonon coupling. For the long-range interaction this effect is seen directly in the definition of the polaron constant in Eq. (3.18) where α_p is inversely proportional to the polaron radius. In this expression the important measure is the effective confinement radius and not the mechanism that imposes it. This effective confinement radius is not necessarily the

polaron radius. With the localization length either larger or smaller than the free polaron radius, the coupling strength experienced by the localized carriers is either comparable to or stronger than that of the free carriers.

With an increased short- and long-range electron-phonon interaction it is evident from the phase diagram in Fig. 4-2 that the stable configuration may change discontinuously from a large to a small polaronic state upon impurity localization. Thus, opposite to normal behavior, doping may cause the system to become *more* insulating[82]. In La_2CuO_{4+y}, however, the localization length of the impurity state is measured to be 8 Å[22] for lightly oxygen doped crystals. This is substantially larger than a single unit cell implying that the localized polarons are still large. The localization length is of the same size as the polaronic radius $a_p \simeq 7$ Å suggesting that the electron-phonon coupling experienced by the free and the localized holes are of comparable strengths.

4.3 Absorption by Localized Polarons

To qualitatively discuss the spectral features induced by a strong electron-phonon interactions it will be helpful to consider the configuration coordinate diagram drawn in Fig. 4-3. For this we will initially assume excitation of a small polaron where the electron interacts with only one lattice coordinate Q. The diagram is then simply a graphical representation of the total energy of the electron and the lattice for various excited states of interest. In Fig. 4-3 we have considered a two-level system where $E_g(Q)$ represent the ground-state energy and $E_e(Q)$ the excited state. The lattice coordinates Q_g and Q_e represent the stable configuration for the ground state and the excited state respectively. These energies are the potential energies for nuclear motion. Near each minimum we can use the harmonic approximation so that the vibrational states are harmonic oscillators of energies $(n_g + 1/2)\hbar\omega_0$ for the ground state and $(n_e + 1/2)\hbar\omega_0$ for the excited state. The low-lying vibrational states are indicated in

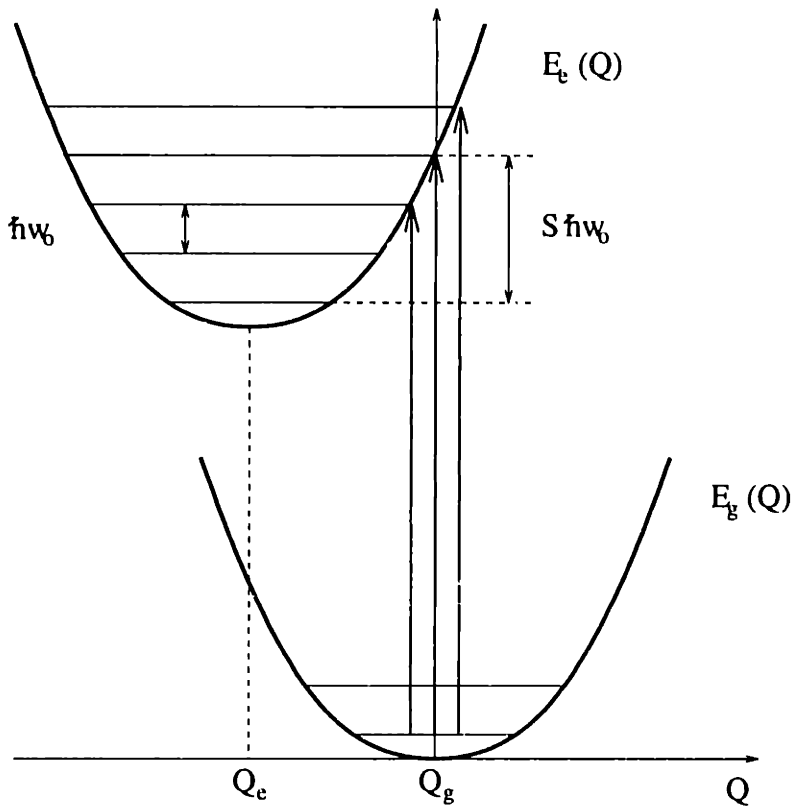

Figure 4-3: Configuration coordinate diagram showing transitions for absorption from the ground state g to phonon states of the excited state e.

Fig. 4-3. The change in the optimum lattice coordinate for the two states reflects a difference in the strength of the coupling to the lattice. We express this difference in terms of the Huang-Rhys factor S defined in Fig. 4-3 where $|Q_g - Q_e| \propto \sqrt{S}$. At low temperatures only the ground state of energy $E_g(Q_g) + \hbar\omega_0/2$ is populated. Optical excitation can occur between this state and all phonon states of the excited configuration of energy $E_e(Q_e) + (n + 1/2)\hbar\omega_0$. In this model the absorption will then consist of sharp lines of frequencies $\hbar\omega = E_e(Q_e) - E_g(Q_g) + n\,\hbar\omega_0$ where n is the number of phonons involved in the transition. Thus the electron-phonon coupling both broadens and blue-shifts the absorption spectrum. Applying the Frank-Condon principle only vertical transitions are allowed. In the strong coupling limit with $S \gg 1$ the stable lattice configuration in the initial state is strongly displaced relative to the final configuration and only excited final states have a non-vanishing overlap with the

initial configuration. In this limit the absorption spectrum approaches a Gaussian distribution function centered at $E_e(Q_e) - E_g(Q_g) + S\,\hbar\omega_0$ with a width of $\sqrt{S}\hbar\omega_0$.

The impurity trapped holes in La_2CuO_{4+y} form large polarons, not small. Thus, instead of interacting with only one localized lattice mode, the holes couple to a continuum of lattice modes. These lattice modes are completely delocalized over the crystal volume, i.e., their amplitude on each lattice site is of order $1/\sqrt{N}$, N being the number of atoms in the crystal. By Fourier-expanding the lattice displacement in terms of the generalized coordinates $\vec{u}_{\vec{q}}$ as defined in Eq. (3.24), the extended lattice modes are reduced to localized harmonic excitations in $\vec{q}$-space centered around an equilibrium position. The interaction between an electron and a phonon mode with wave-vector $\vec{q}$ can be described by a configuration coordinate diagram as shown in Fig. 4-3, but as a function of the corresponding generalized coordinate $\vec{u}_{\vec{q}}$ where the Huang-Rhys factor $S_{\vec{q}}$ is now of the order of $1/N$. Each phonon mode will contribute with a displacement of order $\propto \sqrt{S_{\vec{q}}} \propto 1/\sqrt{N}$ to every lattice point. The total displacement of the lattice is a superposition of the contribution from the all the phonon modes and is confined to lattice points near the interacting charge carrier. Thus, the continuum model produces a confined lattice distortion, a large polaron as we discussed in Chapter 3 with an effective coupling strength equal to the Huang-Rhys factor $S = \sum_{\vec{q}} S_{\vec{q}}$.

As with coupling to a single localized lattice mode, coupling to a continuum of modes in $\vec{q}$-space broadens and blue-shifts the absorption spectrum. We will in the following assume that the carriers are strongly enough coupled to optical modes for the lattice to be frozen during an optical excitation. This is a valid assumption for both large and small polarons when the excitation energy E_{ex} is larger than the phonon energy $\hbar\omega_0$. In this case the electronic transition time $\sim \hbar/E_{ex}$ is shorter than the responds time $\sim 1/\omega_o$ for the lattice distortion leaving the lattice no time to react during the optical excitation. The Frank-Condon approximation is exact in the strong coupling limit ($S \gg 1$) where the polaronic excitation energy $S\hbar\omega_0$ is much

larger than the phonon energy.

Within the Random Phase Approximation, the contribution from inter-band transitions to the imaginary part of the dielectric constant is expressed as

$$\epsilon_2(\omega) = \frac{4\pi^2 e^2}{3\hbar V} \sum_{i f} |<f|\vec{r}|i>|^2 \delta(\omega - (E_f - E_i)/\hbar). \tag{4.1}$$

Here V is the volume of the sample, $E_{i(f)}$ is the total energy and $|i(f)>$ the wavefunction of the initial (final) state. Only electric dipole allowed transitions are included. Following Ref. [83] we apply the Born-Oppenheimer approximation and write the total wave function for the final and initial state, $|f>$ and $|i>$, as a product of an electronic and lattice part, $|l>= |\psi_l \chi_l>$ for $l = \{f, i\}$ respectively. Since phonons are Bosons, the lattice wave function $|\chi_l>$ can be expressed as a product over all the harmonic lattice modes, $|\chi_l>= \Pi_{\vec{q}} |\chi_{l,n_{\vec{q}}}>$ where $|\chi_{l,n_{\vec{q}}}>$ represents an harmonic oscillator eigenstate with wave vector $\vec{q}$ and quantum number $n_{\vec{q}}$. We enforce the Frank-Condon principle by applying the Condon approximation in which we neglect any possible dependence of the electronic matrix element $<\psi_f|\vec{r}|\psi_i>$ on the lattice configuration. Thus the electric dipole transition matrix can be factorized into an electronic and harmonic part,

$$|<f|\vec{r}|i>|^2 = |<\psi_f \chi_f|\vec{r}|\psi_i \chi_i>|^2 = |<\psi_f|\vec{r}|\psi_i>|^2 \, |<\chi_f|\chi_i>|^2. \tag{4.2}$$

Both in the initial and the final state, the lattice wave function represents a continuum of phonon modes throughout the first Brillouin zone all with excitation energy $\hbar\omega_0$. The total energy in the initial and final state can then generally be expressed as $E_l = \varepsilon_l + (n_l + 1/2)\hbar\omega_0$ where ε_l is the electron energy and n_l the number of excited phonons. Thus the difference in energy between the final and initial state $E_f - E_i = \varepsilon_f - \varepsilon_i + n\hbar\omega_0$ is only a function of the difference $n = n_f - n_i$ in the number of excited phonons. By inserting the factorized expression for the transition matrix, Eq. (4.2), into the general expression for $\epsilon_2(\omega)$, Eq. (4.1), the imaginary part of the phonon

dressed dielectric function can be written as

$$\epsilon_2(\omega) = \sum_{n=-\infty}^{\infty} W_n \, \epsilon_2^o(\omega - n\,\omega_o). \tag{4.3}$$

Here $\epsilon_2{}^o$ is the response of the system in the absence of electron-phonon coupling and W_n is the probability that the transition occurs with the creation of n phonons. The latter is expressed as $W_n = \sum_{g(n)} | < \chi_f | \chi_i > |^2$ where the sum goes over all $g(n)$ combinations of initial and final lattice configurations that differ by n phonons. Calculating the explicit expression for W_n is a straightforward but rather tedious exercise in quantum mechanics and will not be reproduced here. A detailed derivation is found in Ref. [83]. The final result is

$$W_n = \exp[n\,z \; - \; S\coth(z)] \;\; I_n[S\,\mathrm{csch}(z)], \tag{4.4}$$

where $z = \hbar\omega_o/2\,k_BT$, $I_n(x)$ is the modified Bessel function and $S = \sum_{\vec{q}} S_{\vec{q}}$ is the Huang-Rhys factor. To verify this expression consider the limits of weak and strong coupling. In the strong coupling limit ($S \gg 1$) W_n approaches a Gaussian distribution centered around S with a temperature dependent standard deviation $\sqrt{S\,\coth(z)}$. This is the spectral shape as we expected. In the opposite limit, $S \rightarrow 0$, the phonon coupling vanishes and $W_n \rightarrow \delta_{n,0}$ as expected.

In order to calculate $\epsilon_2{}^o$ we must first incorporate the temperature dependence into the general expression in Eq. (4.1). The temperature dependence is given by the number of occupied and available states in the initial and final configurations, respectively. The average number of holes occupying an acceptor state with binding energy E_b is expressed as

$$p_a(E_b) = \frac{2}{\exp\beta(\mu - E_b) + 2} \tag{4.5}$$

where $\beta = 1/k_BT$, μ is the chemical potential and the top of the valence band is

defined as zero energy. The factor two in numerator and denominator ensures that due to the Coulomb repulsion there is no double occupancy for the localized state. The extended states in the valence band, however, can be doubly occupied and the probability of a hole occupying a state k with energy ε_k is given by the Fermi-Dirac distribution function,

$$p_v(\varepsilon_k) = \frac{1}{\exp\beta(\mu - \varepsilon_k) + 1}. \tag{4.6}$$

At high temperatures, when the fraction of thermally ionized holes becomes substantial, induced photo emission will offset the absorption process. Both the absorption and induced emission processes have the same transition probability. Their strengths only differ by the respective number of available states. By subtracting the induced emission process from the absorption process, the effective joint density of states for exciting a hole from the acceptor band to a state k in the valence band is given by

$$\begin{aligned} & N_A\, p_a(E_b)\,[1 - p_v(\varepsilon_k)] - N_A\,[1 - p_a(E_b)]\; p_v(\varepsilon_k) \\ \Rightarrow\quad & N_A\,[p_a(E_b) - p_v(\varepsilon_k)] \end{aligned} \tag{4.7}$$

where N_A is the density of acceptor states. The first term represents absorption and the second term induced emission.

It is convenient to express the dielectric function in terms of the oscillator strength rather than the transition matrices. The oscillator strength for the $a \rightarrow k$ transition is defined as

$$f_{k,a} = \frac{2m^*}{3\hbar^2}(E_b - \varepsilon_k)|<k|\vec{r}|a>|^2. \tag{4.8}$$

This quantity is convenient since it satisfies the sum rule $\sum_k f_{k,a} = 1$. By substituting the transition matrix in Eq. (4.1) with the oscillator strength and multiplying by the effective number of available states, Eq. (4.7), the dielectric function, in the absence

of electron-phonon coupling, can be expressed as

$$\epsilon_2^o(\omega', T) = \frac{2\pi^2 N_A e^2}{m^* \omega'} \Gamma(\omega') \times \left[\frac{2}{e^{\beta(\mu - E_b)} + 2} - \frac{1}{e^{\beta(\hbar\omega' - E_b + \mu)} + 1} \right], \tag{4.9}$$

where

$$\Gamma(\omega') = \sum_k f_{k,a}\, \delta(\omega' - (E_b - \varepsilon_k)/\hbar) \tag{4.10}$$

and $\omega' = \omega - n\omega_o$. Here $\Gamma(\omega')$ is the conductivity spectrum one would have seen at zero temperature if there were no electron-phonon coupling. By applying the sum rule $\sum_k f_{k,a} = 1$ we find that the integrated conductivity is conserved, $\int \Gamma(\omega')\, d\omega' = 1$, consistent with the definition of effective number of carriers, N^*_{eff}, given in Eq. (1.1).

The temperature dependence is dominated by the carrier occupation in the acceptor band given by the first term in the square bracket. The second term is the occupation of free carriers in the valence band which gives rise to induced emission. We model the change in the position of the Fermi level as a function of temperature by using a simple compensated acceptor-band model. The behavior of the chemical potential is determined by requiring that the total number of localized and free carriers is constant, thus

$$\frac{1}{V} \sum_k p_v(\varepsilon_k) + N_A\, p_a(E_b) = N_A - N_D \tag{4.11}$$

where N_D is the density of compensating donor states. The presence of compensating donors is demonstrated experimentally as discussed in section 1.1. The first term on the left side represents the density of holes thermally excited into the valence band at a temperature T. It is determined by adding up all the states in the valence band weighted by their occupation number. For a 2D band edge assuming $k_B T \ll \mu \simeq E_b$

Eq. (4.11) reduces to

$$\frac{m^* k_B T}{\pi L_z \hbar^2} e^{-\beta\mu} + \frac{2 N_A}{e^{\beta(\mu - E_b)} + 2} = N_A - N_D, \tag{4.12}$$

where L_z is the lattice spacing in the third direction.

4.4 Modeling the Impurity Absorption Spectrum

The model can best be compared to the data by studying the difference $\epsilon_2(\omega, T) - \epsilon_2(\omega, 238K)$ displayed in Fig. 4-4. The reflectivity data in Fig. 4-1(a) show a decrease in the strength of the 0.5 eV band between 238 K and 295 K whereas it appears to be independent of T at lower temperatures. Thus we use the 238 K scan to subtract off the 0.5 eV absorption. The resulting peak at ~ 0.13 eV has a half-width of ~ 0.07 eV. The long high energy tails may result from a weak temperature dependence of the 0.5 eV band. The dominant response to increasing temperature is a reduction in the overall oscillator strength in the 0.13 eV band with little change in shape as the localized carriers are thermally ionized.

In order to apply Eqs. (4.3), (4.4), (4.9) and (4.12) to the data we use $E_b = 0.035$ eV, $\hbar\omega_0 = 0.043$ eV and $N_A - N_D = 0.008$ per Cu ion. The last number, based on an extrapolation of the Hall density data in Fig. 1-4 to infinite temperature, is only accurate to a factor ~ 2. This uncertainty has no impact upon our analysis since the T-dependence of ϵ_2 is only weakly dependent upon $N_A - N_D$. The compensation ratio N_D/N_A is determined from a fit to the T-dependence of the reflectivity as discussed below.

The peak position, the line width and the line shape are all properties determined solely by S in our model. For $S > 1$ the shift of the peak position and the broadening are only weakly dependent on the detailed form of $\Gamma(\omega')$. For convenience, we use $\Gamma(\omega')$ calculated for ionization of a hole bound in a Coulombic impurity potential[84];

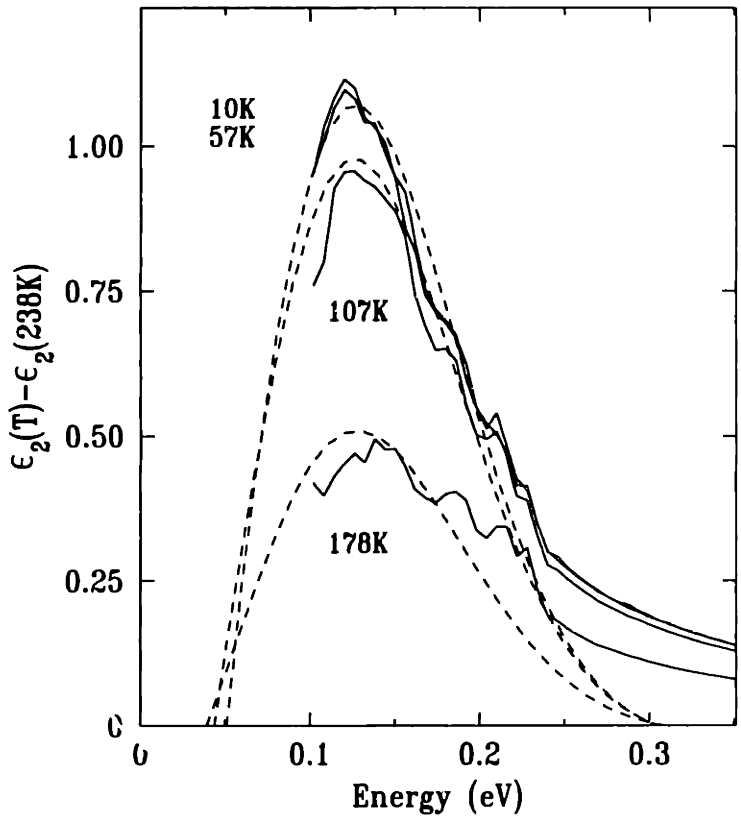

Figure 4-4: The in-plane difference spectrum $\epsilon_2(w,T) - \epsilon_2(\omega, 238K)$ for different temperatures. The broken lines represent best fits to the data using the model and parameters discussed in the text.

that is

$$\Gamma(\omega') = \frac{2^7}{3} \frac{E_b^3}{(\hbar\omega')^4} \frac{e^{-4n' \operatorname{arccot} n'}}{1 - e^{-2\pi n'}} \tag{4.13}$$

where $n' = \sqrt{E_b/(\hbar\omega' - E_b)}$. This spectral function decreases monotonically with increasing energy from a maximum at $\hbar\omega' = E_b$ with half-maximum at $\sim (4/3)E_b$. The best fit, displayed in Fig. 4-4, gives $S = 2.4$. The fit clearly recreates the position of the center frequency and the overall width as well as the general temperature dependence.

In La_2CuO_{4+y} the excess oxygen is believed to be positioned in between the CuO_2 planes while the hole is confined to the planes. The effective attractive potential will consequently not diverge as $r \to 0$ as for the Coulombic potential, but rather it

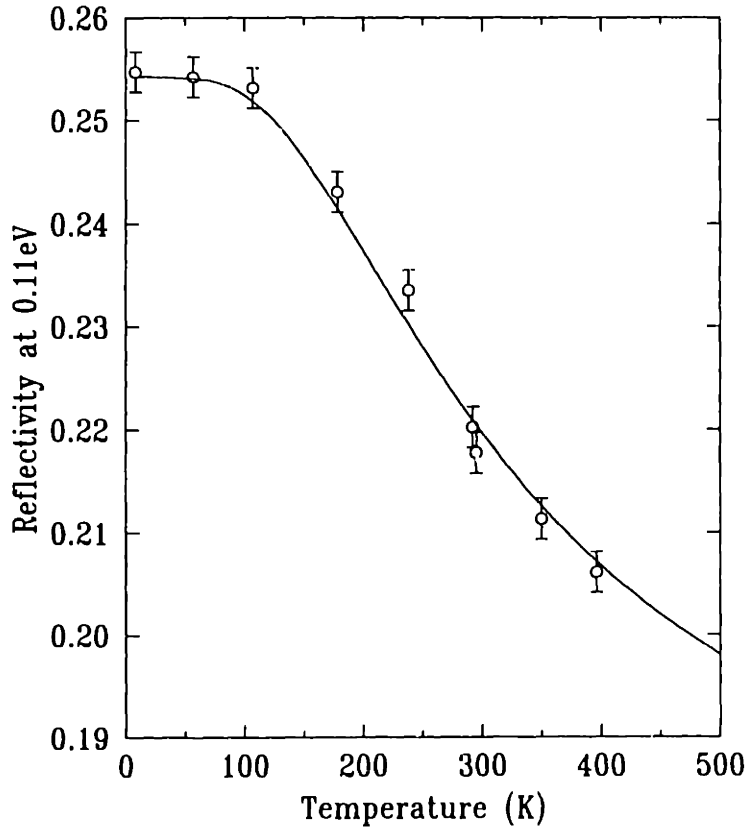

Figure 4-5: The temperature dependence of the in-plane reflectivity at 0.11 eV. The solid line represents the best fit to the data using the model and parameters discussed in the text.

will saturate at a negative value corresponding to the minimum distance between the excess oxygen and the hole. To qualitatively evaluate the effect on $\Gamma(\omega')$, consider the scattering cross section which can be approximated by the Fourier component of the scattering potential. By leveling the potential at small r, strength is transferred from high to low frequencies in the Fourier spectrum. Thus, to test the sensitivity to the choice of $\Gamma(\omega')$ we tried an extremely narrow electronic cross section, $\Gamma(\omega') = \delta(\hbar\omega' - E_b)$. The best fit for the latter yields $S = 2.7$ with a line shape indistinguishable from the Coulombic fit. Thus, independent of the details, we find $S = 2.5 \pm 0.2$.

To study the temperature dependence in more detail we compare in Fig. 4-5 the in-plane reflectivity at 0.11 eV as a function of temperature with that calculated from our model. The real part of the dielectric response, $\epsilon_1(\omega)$, is extracted from the calculated

$\epsilon_2(\omega)$ using the Kramer-Kronig relations given in appendix B. The reflectivity is then calculated from the total complex dielectric response, $\epsilon(\omega) = \tilde{\epsilon_o} + \epsilon_1(\omega) + i\epsilon_2(\omega)$. Using $\Gamma(\omega')$ from the Coulombic model, with $S = 2.4$, we vary the compensation ratio N_D/N_A and the effective dielectric constant $\tilde{\epsilon_o}$. The fit, displayed as a solid line in Fig. 4-5, gives $\tilde{\epsilon_o} = 5.7$ and $N_D/N_A = 0.5$. The activated T-dependencies in Eqs. (4.9) and (4.12) make the fit insensitive to $N_A - N_D$ and N_D/N_A as long as N_D is not much smaller than N_A. Good fits are found for $N_D/N_A = 0.5 \pm 0.1$ for a reasonable range of $N_A - N_D$. The reflectivity is temperature independent below $\sim 100\,\mathrm{K}$ reflecting the negligible fraction of carriers thermally excited from the localized states. At higher temperatures this fraction increases, decreasing the strength of the 0.13 eV band.

The optimized effective dielectric constant $\tilde{\epsilon_o} = 5.7$ should be compared with the high frequency dielectric constant in the undoped sample, $\epsilon_\infty = 4.8$. The slight difference probably results from a small contribution to the dielectric constant at low energies from the 0.5eV absorption band in the doped sample.

We have no independent measure of the compensation ratio. However, from transport measurements we know that the Fermi level is pinned in the impurity band over the entire temperature range of activated conductivity. Applying Eq. (4.12) this requires the compensation ratio to be larger than 0.3, consistent with our value 0.5 ± 0.1.

The Huang-Rhys factor S is a direct measure of the number of phonons involved in the ionization. Thus, contrary to the polaronic coupling constant α_p introduced in chapter 3, S is a relative measure between two states. Since the transitions correspond to excitations between two polaron states, S is generally smaller than the number of phonons S' involved in the localized polaron. Optimally, if the lattice displacement associated with the localized and free holes have the same structure $S = S' - \alpha_p$. On the other hand, if their structures are very different $S = S'$. Thus the measured Huang-Rhys factor satisfies the inequality $S' - \alpha_p < S < S'$. In addition, only in the strong coupling limit will the Frank-Condon principle be fully satisfied. For weaker coupling, the lattice will partly relax during the excitation process. For both of these

reasons the measured coupling constant, $S = 2.5$, is only a lower bound on the true coupling constant for the localized polaron, and we do not therefore consider the difference between $\alpha_p = 5.7$ and $S = 2.5$ to be significant.

4.5 Polaronic Impurities - a Generic Feature of the Cuprates

The mid-infrared absorption is a common feature of the cuprates. In Fig. 4-6 we display the conductivity spectra of Thomas *et al.*[47] for several oxygen doped oxides. In La_2CuO_{4+y}, Nd_2CuO_{4-y} as well as $YBa_2Cu_3O_{6+y}$ two infrared absorption peaks become stronger with doping, one in the energy range $0.5 - 0.75\,eV$ and the other in the range $0.13 - 0.16\,eV$. It would be quite remarkable if the origin of these absorption processes were fundamentally different for the different materials. Thus, we expect our results to be a general feature of the high-T_c cuprates. In Nd_2CuO_{4-y} the low-energy absorption centered at $0.16\,eV$ has been found to broaden with increasing temperature in a linear fashion[47], but no decrease in oscillator strength has been observed up to $300\,K$. This behavior can easily be explained within the framework of our model if the binding energy of the donor impurity in the sample studied is $\geq 0.09\,eV$. In this case the fraction of thermally ionized holes is neglectable below room temperature and the temperature dependence is dominated by broadening of the phonon sidebands. By measuring the temperature dependent conductivity of several as-grown Nd_2CuO_{4-y} crystals, we observed activated behavior with activation energies up to $0.080\,eV$, suggestive of such a large donor binding energy.

The doping enhanced mid-infrared absorption bands have also been studied in photo-induced optical absorption spectra. In Fig. 4-7 we display the photoinduced absorption spectra of Kim *et al.*[43] for both La_2CuO_4 and Nd_2CuO_4. Two absorption band appear as peaks in the range $0.13 - 0.16\,eV$ and $0.5 - 0.75\,eV$ with excitation energies in close agreement with the doping induced mid-infrared bands observed

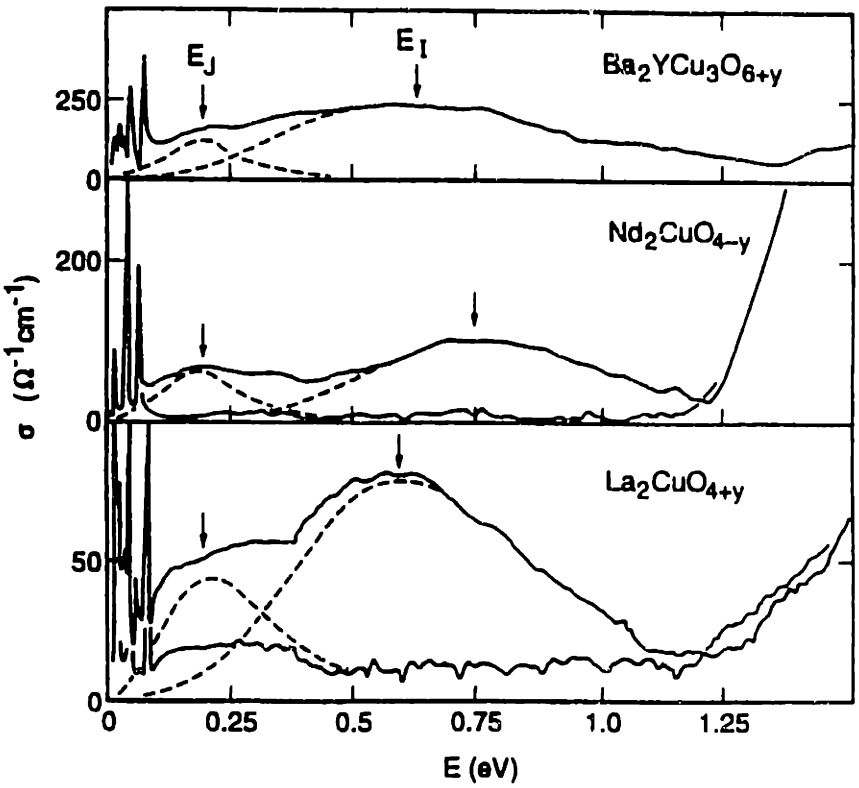

Figure 4-6: Optical conductivity in the mid-infrared region in lightly oxygen doped $YBa_2Cu_3O_{6+y}$, Nd_2CuO_{4-y} and La_2CuO_{4+y} (from Ref. [47]).

in Fig. 4-6. The same correlations between doping induced and photoinduced mid-infrared excitations are also observed in $YBa_2Cu_3O_6$[42] implying that photo carriers and carriers induced by doping have the same effect upon the optical spectrum. In Fig. 4-8 we show the temperature dependence of the mid-infrared photoinduced excitations for both La_2CuO_4 and Nd_2CuO_4 as measured by Kim *et al.*. In both La_2CuO_4 and Nd_2CuO_4 the strength of the 0.13 - 0.16 eV excitation is exhausted by increasing the temperature above $\sim$ 20 K. The high-energy band, on the other hand, does not display any temperature dependence up to 295 K. Kim *et al.* also observe an increase in the photoinduced free carrier conductivity ($<$ 0.06 eV) with increasing temperature suggesting a transfer of oscillator strength between free carrier conductivity and a photo-ionization band of localized photo carriers.

This is qualitatively the same behavior as we observe in the reflectivity spectrum

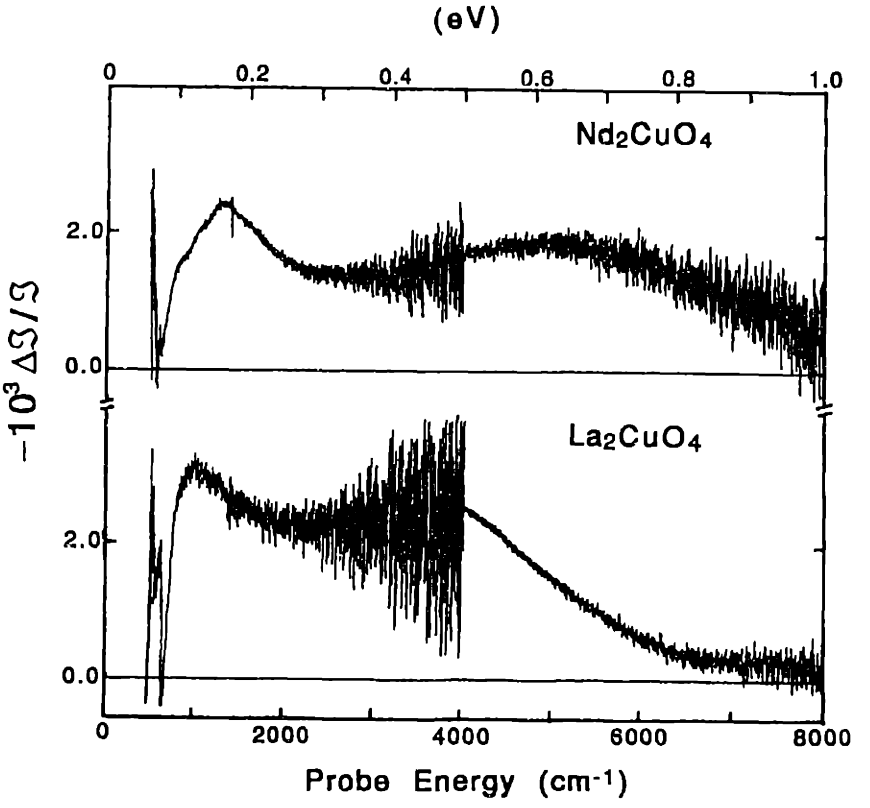

Figure 4-7: Photoinduced absorption spectra measured at $T = 4.2\,\mathrm{K}$. The laser pump intensity was $30\,\mathrm{mW/cm^2}$ at 2.7 eV (from Ref. [43]).

for La_2CuO_{4+y} but at lower temperatures for the photo-induced spectrum. The temperature dependence of the low-energy band is consistent with photo-ionization of localized polarons with a binding energy of $\sim 6 - 7\,\mathrm{meV}$. The low binding energy possibly reflects the lack of oxygen impurities combined with the high photocarrier concentration in the CuO_2 planes. Kim *et al.*[43] estimate the photocarrier density in the CuO_2 planes to $\sim 2\%$ per Cu ion. The large difference between the optical and thermal ionization energy reflects that localized photocarriers form polarons. Finally, the behavior is observed for both an electron and hole doped system which suggest that polaronic impurity states are a generic feature of the High-T_c cuprates.

A related mechanism has been suggested as an explanation of the $0.13 - 0.16\,\mathrm{eV}$ photoinduced infrared absorption band in $YBa_2Cu_3O_{6+y}$[88]. By considering a transition from a defect level to a small-polaron band coupled to a 0.060 eV phonon, a

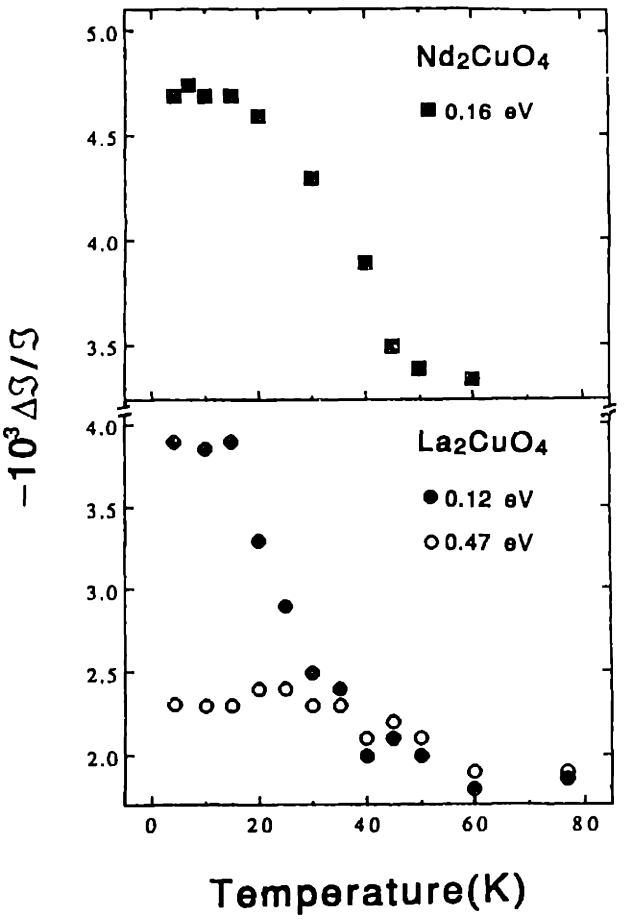

Figure 4-8: Temperature dependence of the photoinduced electronic excitations of Nd_2CuO_4 ($70\,mW/cm^2$) and La_2CuO_4 ($100\,mW/cm^2$) with 2.4 eV pump (from Ref. [43]).

defect binding energy of $\sim$ 0.01eV and a Huang-Rhys factor of $S = 2.57 \pm 0$ are extracted, in close proximity to our values.

Theoretical studies suggest that there is a strong tendency for dilute holes in an antiferromagnet to phase separate[89, 90]. Recently such phase separation has been observed in heavily oxygen doped La_2CuO_{4+y} with $y > 0.03$ which displays both superconductivity below $\sim$ 35 K and antiferromagnetic ordering[91]. The behavior of the Néel temperature and the magnetic susceptibility of the antiferromagnetic phase have been interpreted with a model that assumes segregation of the doped holes into walls of hole-rich material separating undoped domains. The macroscopic

phase separation is made possible by the high diffusivity of the excess oxygen counter charges allowing the system to settle in the most energetically favorable configuration. With the introduction of immobile Sr dopants, a static uniform charge distribution is added. This clearly reduces the energetic advantage of phase separation and hence reduces the ordering temperature, ultimately to a point where the oxygen as well as the Sr dopants cease to be mobile on laboratory time scales.

Like the oxygen ions, the photo-induced electron (hole) counter charges can easily move allowing for macroscopic phase separation. Several workers[43, 92, 90] have also argued that features in the photo-induced absorption spectra suggest the formation of local metallic domains. Specifically, in lightly doped $YBa_2Cu_3O_{6+y}$, Mihailivić *et al.*[93] find that the photo-induced infrared absorption is observed at phonon frequencies of the superconducting material $YBa_2Cu_3O_7$, while photo-induced bleaching (reduction in the absorption strength) is observed at phonon frequencies of the undoped insulating material $YBa_2Cu_3O_6$. With a photocarrier concentration of order 1%, the argument goes, a uniform distribution of the photo-generated holes at these densities could not cause the observed changes. Such changes are however consistent with a phase-separation picture. The photo-induced infrared absorption is in this model due to the metallic fraction of the material, and the bleaching is due to a photo-induced decrease of the insulating fraction.

In the most comprehensive study of the photo-induced vibrational excitation Ye *et al.*[80] find that all the phonon bleaching modes corresponds to in-plane LO E_u symmetric phonons. As we argued in section 3.4, this is consistent with polaron formation of photoexcited holes through a Fröhlich electron-phonon interaction. As far as the photo-induced absorption modes are concerned, Ye *et al.* find that in undoped $YBa_2Cu_3O_6$, the majority of these modes are Raman active phonons of the *undoped* material. In doped $YBa_2Cu_3O_{6.3}$ a shift is observed for Raman active modes of the metallic $YBa_2Cu_3O_7$, consistent with the result of Mihailivić *et al.*[93]. This behavior is hardly strong evidence for phase separation but suggests instead a non-Fröhlich

type interaction between photocarriers and the Raman active phonon modes. A linear coupling of charge carriers to Raman-active phonon modes of A_g symmetry is well known in organic semiconductors and causes structure in the optical conductivity at the phonon frequency. A discussion of such an electron-phonon coupling with respect to the copper oxides can be found in Ref. [52]. A strong interaction between certain A_g symmetric Raman modes and the charge carriers is theoretically predicted for metallic $La_{1.85}Sr_{0.15}CuO_4$[94]. In the end, the best argument against a phase separation interpretation of the photo-induced absorption data is the strong similarity between the photo-induced electronic absorptions and the electronic excitations in the lightly doped material both in spectral features and temperature dependence.

Chapter 5

The Charge Carrier Enhanced Infrared Excitations

In Chapter 4 we were able to identify the 0.13 eV excitation mainly through its characteristic temperature dependence. The 0.5 eV and 1.5 eV infrared absorption bands, on the other hand, are lacking both sharp spectral features and strong temperature dependence, and a similar identification is, therefore, not possible. In pursuit of the microscopic origin for these excitations we have two clear options. One possibility is to vary a parameter other than the temperature to distinguish different excitation mechanisms. Another possibility is to search for traces of spectral features with characteristic structure in the undoped crystals. Together, in the MIT collaboration have worked along both paths. While Perkins *et al.*[54] have measured weak sub-gap absorption in undoped crystals, Falck *et al.*[55] have studied how the absorption spectrum changes with an applied electric field. Together these measurements have deepened our understanding of the mid-infrared electronic excitations in undoped copper oxides with possibly important implications for the doped cuprates. It is interesting to note that while such a line of attack in retrospect appears natural, neither of these measurements were motivated by such a reasoning. Moreover, while the interpretation of the electroreflectance spectra builds on the results of the

transmission study of Perkins *et al.*, the modulation spectra were from measurements made three years earlier.

We start out in section 5.1 by reviewing the transmission measurements on undoped copper oxides by Perkins *et al.*. Charge-transfer excitations with multimagnon and phonon sidebands are observed near 0.5 eV and 1.5 eV. These excitation energies correspond to the mid-infrared absorption bands in doped crystals and provide a natural origin for the doping enhanced excitations. Based on these results we will in section 5.2 interpret electroreflectance spectra for La_2CuO_{4+y} crystals. Depending on the electrode structure, the most important consequence of the modulation is addition of charge carriers or variation of the electric field in the space charge region. By comparing the carrier modulation data with reflectivity of doped and undoped La_2CuO_{4+y}, we demonstrate that the observed doping enhanced mid-infrared absorption is primarily caused by the excess holes in the CuO_2 layer rather than by the increased impurity or defect concentration that induces them. In section 5.3 we show that the response of the 1.5 eV infrared band to electric field, both in strength and polarization dependence, is consistent with a $d_{x^2-y^2} \rightarrow d_{xy}$ transition. The response of the 0.5 eV band is found to be inconsistent with transitions to both d_{xy}, and d_{yz}, d_{zx} symmetry states, supporting a $d_{x^2-y^2} \rightarrow d_{z^2}$ interpretation. Both the energies and the symmetries of the doping enhanced excitations are in agreement with those of the crystal-field excitations and magnon sidebands observed in the undoped copper oxides. Hence excitons and sidebands emerge as natural candidates for the doping induced mid-infrared absorption.

5.1 Crystal-field Excitations in Undoped Cuprates

In Fig. 5-1 we display the absorption coefficient spectrum for undoped La_2CuO_4 measured by Perkins *et al.*[54]. A linear background is subtracted to enhance the spectral features. The dominant feature is the sharp low-energy line centered near

0.4 eV with a full width of order $\sim$ 0.05 eV. At higher energies, a set of broader bands is observed which extend up to $\sim$ 1.2 eV. The same spectral structure, a sharp low energy peak with a set of broader bands at higher energies, was observed for $Sr_2CuO_2Cl_2$. The sharp low energy peak and the first of the broad sidebands was also seen in Nd_2CuO_4 and Pr_2CuO_4. The structure is clearly common to the undoped copper oxides. Moreover, the authors find that the integrated strength of the low-energy peak only varies within a factor of three among the four different materials.

The transmission spectra were measured in α polarization (electric field $\vec{E} \parallel CuO_2$ layer and wavevector $\vec{k} \perp CuO_2$). On an additional La_2CuO_4 sample the (100) tetragonal surface was polished for measurements with wavevector $\vec{k}$ in the plane for both σ ($\vec{E} \parallel CuO_2$) and π ($\vec{E} \perp CuO_2$) polarizations. Identical spectra were obtained in α and σ polarization while all features were absent in π polarization. Thus the absorption bands only appear when the electric field vector lies in the CuO_2 layer consistent with electric dipole allowed excitations. Moreover, the absorption bands appear with the magnetic field vector pointing both parallel and perpendicular to the CuO_2 planes inconsistent with magnetic dipole allowed excitations.

The sharp feature clearly resembles an exciton. Perkins *et al.* speculate that this low-energy peak is a Frenkel exciton arising from transitions between the crystal-field split Cu 3*d* bands. Before we discuss the identity of this excitation we will first consider the sidebands.

We saw in chapter 4 how the electron-phonon coupling caused strong sidebands in the photo-ionization process. In fact, almost all of the oscillator strength was found to be in the sidebands corresponding to ionizing the localized hole and creating phonons in the same process. While the phonon sidebands were smeared and did not display any structure separating the different higher order phonon excitations, the sidebands in Fig. 5-1 do have some structure with the first sideband blue-shifted $\sim$ 0.15 eV relative to the low-energy exciton line. Such an energy shift is of order three times larger than the average optical phonon energy, ruling out any vibrational excitation.

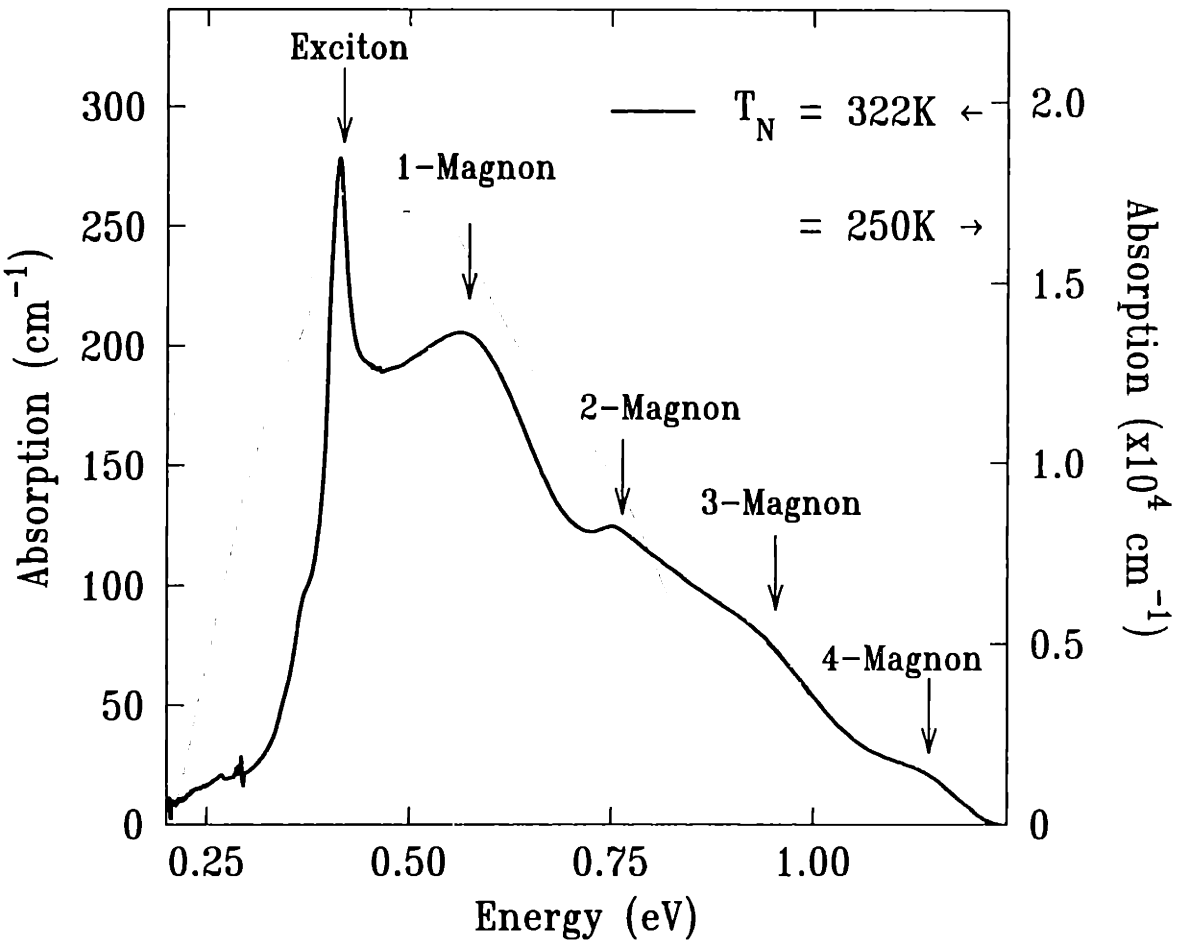

Figure 5-1: The in-plane absorption coefficients of La_2CuO_{4+y} for $y = 0$ and $y = 0.014$ at 10 K after subtracting a constant dielectric background. The undoped spectrum is from Perkins *et al.*[54]. The solid thin line corresponds to the conductivity spectrum in Fig. 1-7(c). For the broken thin line we have also subtracted the contribution from photo-ionization of polaronic impurities as discussed in the text.

Since all the four materials corresponds to 2D, S = $\frac{1}{2}$ Heisenberg antiferromagnets, it is natural to ask whether the broad features could result from simultaneous exciton-magnon absorption. With a zone-boundary excitation energy of $\sim 2J \simeq 0.26\,\mathrm{eV}$, such a mechanism is certainly compatible with the broad structure.

One can picture the exciton-magnon interaction as follows. With the hole in the $d_{x^2-y^2}$ ground state, the $d_{x^2-y^2}$ orbital has a large overlap with neighboring Cu ions through the bridging O p_σ orbitals, giving rise to the large superexchange energy J. If the hole is excited to a Cu d state with different symmetry, the overlap with

the bridging oxygen ions, and consequently the superexchange energy, is strongly reduced. Thus, the creation of a crystal-field exciton will obviously have an impact on the local magnetic order giving rise to a coupling between the exciton and the magnetic excitations.

While the electron-phonon excitation combines two electric dipole allowed excitations, impurity absorption and phonon creation, the effect of the exciton-magnon excitation is very different. For the crystal-field excitations, both the initial and final states have even parity, making the transition electric dipole forbidden. Creation of a magnon, on the other hand, requires a spin-flip. Since photons do not carry spin, this excitation is also electric-dipole forbidden. It turns out, however, that excitation of a magnon and an exciton combined is weakly electric dipole allowed[95]. Moreover, since the exchange integral in the excited state is much lower than J, the excess energy cost of creating one magnon in addition to the exciton is less than the zone-boundary magnon excitation energy $2J$. Perkins *et al.* find that the n-magnon sidebands should be located at $\sim 3nJ/2 = 0.19\,\mathrm{eV}$. The measured offset to the first peak in Fig. 5-1 is $\sim 0.15\,\mathrm{eV}$. The predicted positions for the 2−, 3− and 4−magnon peaks, assuming a constant energy difference of $3J/2 \simeq 0.19\,\mathrm{eV}$, are marked in the figure. Clearly the predicted 2−magnon position agrees very well with the observed second peak. There are also pronounced shoulders at the predicted 3−magnon and 4−magnon positions.

Perkins *et al.* show that not only the energy, but also the intensity of the one-magnon sideband is of the expected magnitude. Thus, they provide strong evidence for the identification of the sidebands as exciton-magnon excitations. Moreover, the magnon sideband, and by implication the exciton itself, is an intrinsic excitation of the CuO_2 layer. However, while identification of the sidebands seems unambiguous, the electronic origin of the exciton is somewhat more difficult to ascertain unambiguously. As illustrated in Fig. 1-6, cluster calculations[12] favor transitions to d_{z^2} state as the lowest energy excited state with d_{xy} and d_{zx}, d_{yz} states at successively higher energies.

As we will discuss in connection with the electroreflectance data in section 5.3, the lack of any structure in the out-of-plane π polarization rules out the d_{xz}, d_{yz} states. That leaves us with final states of d_{z^2} and d_{xy} symmetry. We will in the following sections show that both electroreflectance and Raman spectra are consistent with a $d_{x^2-y^2} \rightarrow d_{xy}$ transition near 1.5 eV. Perkins *et al.* find a weak absorption band near 1.5 eV in $Sr_2CuO_2Cl_2$ and assign this transition to the d_{xy} excitation. They assign the 0.4 eV exciton to the $d_{x^2-y^2} \rightarrow d_{z^2}$ transition. The energy, however, does not agree with cluster calculations[12] which predict an excitation energy in the range $0.9 - 1.6$ eV.

With final states of either d_{z^2} or d_{xy} symmetry Perkins *et al.* find that the polarization dependence is only consistent with an electric dipole allowed transition, inconsistent with both magnetic dipole and electric quadrupole transitions. One possible explanation for this behavior is that electric fields from impurities and defects break the inversion symmetry at the Cu site mixing even and odd parity states. In this case, the strength of the low-energy peak should be very sensitive to the impurity concentration. In contrast, Perkins *et al.* find the integrated strength of the low-energy peak to vary by less than a factor of ~ 3 for the four different materials. Moreover, measurements on crystals of different purity levels reveal 0.4 eV peaks of the same strength[96], making an impurity induced exciton mechanism quite unlikely.

If the absorption is not induced by impurities or defects, it must be intrinsic. Since the strength and excitation energy are roughly the same for four different materials, the mechanism is probably intrinsic to the CuO_2 layer. It is interesting to note that the energy of the exciton near 0.4 eV is almost equal to the energy of a peak in the Raman spectrum associated with 2-magnon Raman scattering. Moreover, both the $d_{x^2-y^2} \rightarrow d_{z^2}$ transition and 2-magnon Raman scattering have the same B_{1g} symmetry. In this case we expect these two excitations to interact as long as there exists an interaction that couples them. A strong exciton-magnon coupling is evident from the magnon sidebands. Thus the assignment of the low-energy excitor

to the $d_{x^2-y^2} \rightarrow d_{z^2}$ transition probably implies that the peak near 0.4 eV seen in both Raman scattering and infrared absorption is neither a pure 2-magnon peak nor a pure crystal-field exciton, but a novel hybrid of these two excitations.

The measurements of Perkins *et al.* provide an important contribution to our understanding of the low-energy electronic excitations in undoped copper oxides. An important aspect of this work is its implications for our understanding of the doped cuprates. Together with the mid-infrared absorption coefficient of undoped La_2CuO_4, in Fig. 5-1 we also display the mid-infrared absorption spectrum for lightly doped La_2CuO_{4+y}. The latter spectrum is extracted from reflectivity measurements and is derived from the $\sigma(\omega)$ spectrum shown in Fig. 1-7(c). To properly compare the doped with the undoped data we have subtracted a linear background $\omega\, b$ from the doped conductivity spectrum shown in Fig. 1-7(c) where $b = 0.55$ corresponds to the saturated ϵ_2 in the $1 - 2$ eV range as seen in Fig. 1-7(b). The thin solid line includes contributions from both the 0.13 eV and 0.5 eV band. To isolate the 0.5 eV absorption band, we have subtracted the photo-ionization spectrum calculated according to Eqs. (4.3)-(4.12) as discussed in chapter 4. The resulting spectrum is displayed as a broken line. We see in Fig. 5-1 that the envelope of the undoped spectrum is in good agreement with the doped spectrum, although the absorption coefficient in the doped crystal is two orders of magnitude stronger. The peak of the broad 0.5 eV band is positioned between the exciton and 1-magnon excitation. Centered around 0.75 eV, close to the 2-magnon excitation, we also find a pronounced shoulder resembling an additional sideband. These correlations suggest that the doped and the undoped spectra have the same origin. Thus excitons and sidebands present a natural explanation for the doping induced mid-infrared absorption. How these initially only weakly electric dipole allowed transitions can gain such strength with doping is presently unclear. Perkins *et al.* speculate that the addition of holes, which are known to modify strongly the magnetism in the ground state, is likely to introduce new matrix elements for dipole allowed exciton-magnon excitations. Further progress

in understanding the undoped mid-infrared absorption and the effect of doping will probably require a complete theoretical investigation.

Based on the work of Perkins *et al.*, an obvious next step is to try to prove or disprove that the doped and the undoped mid-infrared excitations have the same origin. As part of such an ongoing effort we will in the rest of this chapter discuss how an externally applied electric field can characterize the doping induced sub-gap absorptions. While these experiments do not provide a final proof, we will show that the carrier induced 1.5 eV excitation responds to an externally applied electric field in a way consistent with a $d_{x^2-y^2} \rightarrow d_{xy}$ transition.

5.2 The Modulated Reflectivity Spectra

The modulation experiment was performed in two different configurations, using either a metal-insulator-semiconductor or a metal-semiconductor structure as illustrated in Fig. 5-2. Both the single metal layer as well as the metal-insulator structure were transparent allowing us to probe the La_2CuO_{4+y} surface. A detailed account on both the fabrication of the devices and the experimental setup is given in chapter 2.

The modulated reflectivity spectra were measured on tetragonal (100) surfaces with an oscillating voltage applied between the metal electrode and the La_2CuO_{4+y}. The ac response in the photodetector signal was divided by the dc component giving $\Delta R/R$ directly. The two different electrode configurations were observed to create two very different modulation spectra. In the following we first discuss the spectrum for the metal-semiconductor configuration. We show that the dominant contribution, in this case, comes from changing the hole concentration at the metal-semiconductor interface. We then compare this result with the modulation spectrum for the metal-insulator-semiconductor configuration. For all spectra we adopt the sign convention that positive $\Delta R/R$ ($\Delta\epsilon_2$) is defined by an increase of reflectivity (ϵ_2) with increasing voltage of the semiconductor relative to the metal electrode. For a hole-doped semi-

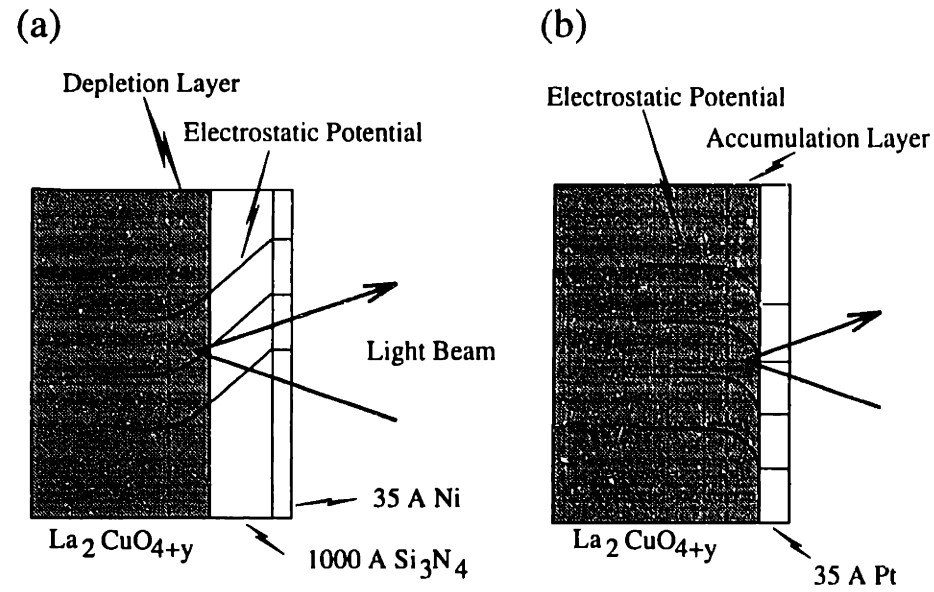

Figure 5-2: **(a)** The metal-insulator-semiconductor configuration used to modulate the electric field in a natural depletion layer. **(b)** The metal-semiconductor configuration used to modulate the hole concentration in a natural accumulation layer. The displayed ideal electrostatic potential equals the hole potential.

conductor this corresponds to increasing accumulation of carriers in an accumulation layer or a decreasing electric field in a depletion layer, that is, forward bias of the junction.

In Fig. 5-3(a) we display the modulation spectra at 10 K and 295 K for the metal-semiconductor configuration of Fig. 5-2(b) for La_2CuO_{4+y} with y=0.016. The out-of-plane reflectivity is only very weakly modulated by the applied voltage. The in-plane spectra, however, display strong modulation with pronounced peaks. Clearly, only excitation processes within the CuO_2 plane are observed. In Fig. 5-3(b) we show the corresponding change in the imaginary part of the dielectric constant, $\Delta\epsilon_2(\omega)$. The absorption in the charge-transfer gap is dominated by a peak at 0.5 eV with half-width $\sim$ 0.2 eV and a broad band between 1.0 and 2.0 eV, with a sharp cut-off near the gap. The structure is only weakly temperature dependent between 10 K and 295 K. For comparison we display in Fig. 5-3(c) the difference between $\epsilon_2(\omega)$ for lightly oxygen doped and undoped crystals, $\Delta_y\epsilon_2$, from spectra like those in Fig. 1-7(b).

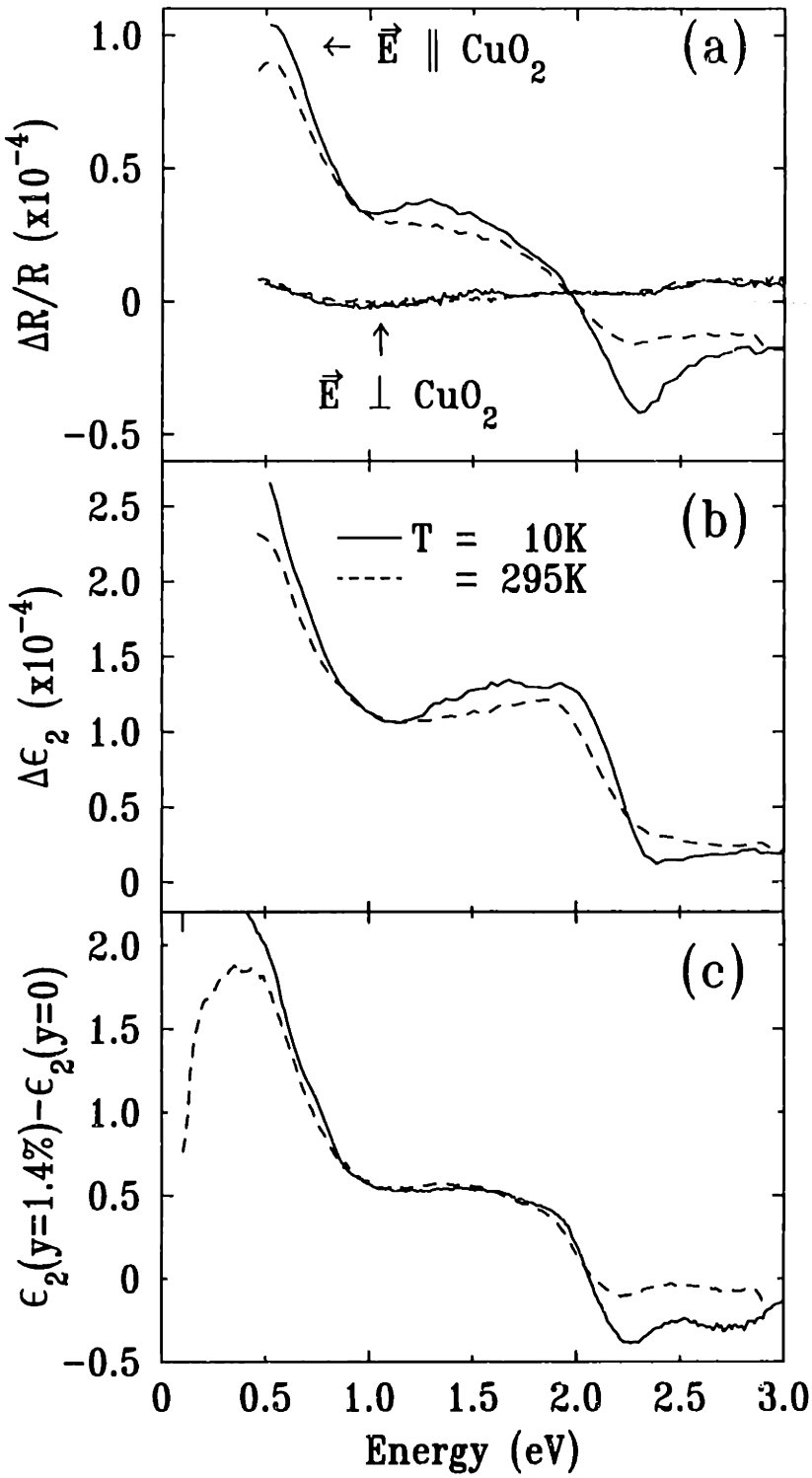

Figure 5-3: **(a)** Modulation reflectivity spectra of La_2CuO_{4+y} with $y = 0.016$ for the metal-semiconductor configuration. **(b)** The in-plane $\Delta\epsilon_2(\omega)$ corresponding to the $\Delta R/R$ spectra in panel (a). **(c)** The difference between the ϵ_2 spectra for lightly oxygen doped and undoped crystals like those displayed in Fig. 1-7(b).

The close similarity between the spectra in panels (b) and (c) suggests that the dominant effect of modulating the voltage across the metal-semiconductor structure is to vary the carrier density near the La_2CuO_{4+y} surface. The most likely explanation is that an accumulation layer is formed at the metal-semiconductor interface at zero-bias and that the applied field modulates the hole density in this layer. The similarity between $\Delta\epsilon_2$ and $\Delta_y\epsilon_2$ suggests that adding holes by means of an electric field or chemically by excess oxygen induces the same changes in the sub-gap absorption. This shows that the observed enhancement of the absorption bands upon chemical doping is primarily caused by the excess holes in the CuO_2 planes and not by the increased impurity or defect concentration that induces them. This conclusion is consistent with photoinduced absorption measurements[42, 43] where the photoexcited carriers induce changes in the absorption spectrum resembling the effect of doping.

We now turn to the modulation spectra for the metal-insulator-semiconductor configuration sketched in in Fig. 5-2(a). Such structures have been previously studied using both La_2CuO_{4+y} and $YBa_2Cu_3O_{6+y}$ as semiconductor with a variety of insulators[20, 60, 97]. In contrast to the metal-semiconductor structure, it is found that the holes are depleted near the semiconductor-insulator interface in all cases[20]. Because of the high density of surface states that causes the depletion layer, application of a voltage only modulates the thickness of the depletion region; it is not possible to drive the semiconductor surface from depletion to accumulation. By modulating the thickness of the depletion region one changes both the average electric field as well as the number of mobile or weakly bound charge carriers in the surface region. Which of these two effects gives the largest contribution to the modulated reflectivity depends on the depletion thickness.

In Fig. 5-4(a) we display the in-plane and out-of-plane $\Delta R/R$ spectra at room temperature for a doped (y=0.016) and an undoped (y=0) crystal. As before, only the in-plane spectra show strong modulation. The corresponding modulation of the imaginary part of the dielectric constant, $\Delta\epsilon_2$, is shown in Fig. 5-4(b) for the in-plane

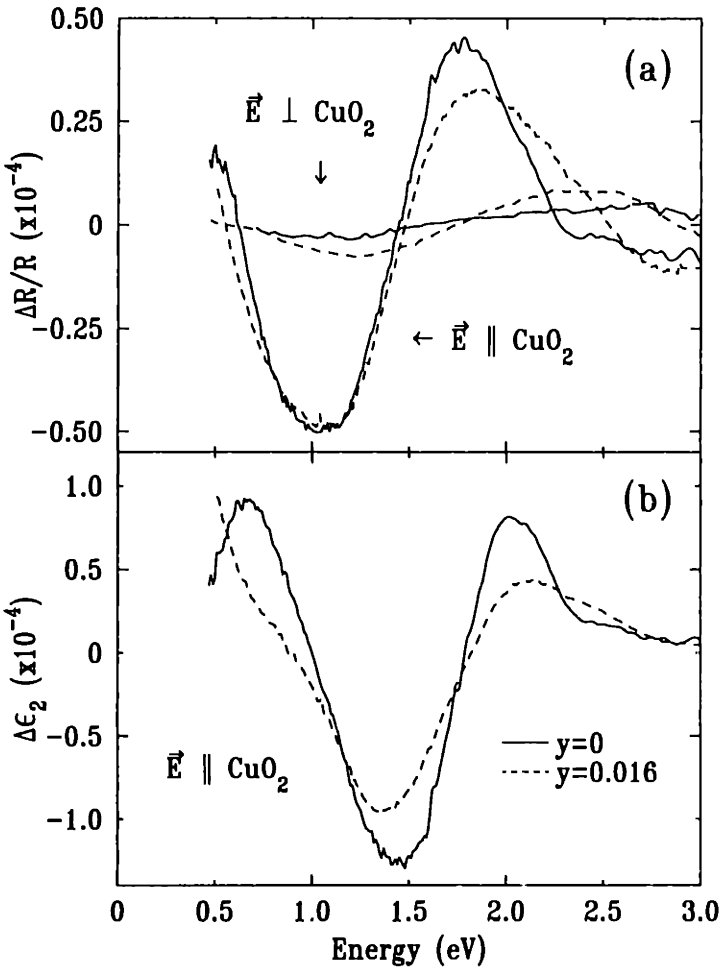

Figure 5-4: **(a)** Modulation reflectivity spectra of La_2CuO_{4+y} with $y = 0$ and $y = 0.016$ at 295 K for the metal-insulator-semiconductor configuration. **(b)** The in-plane $\Delta\epsilon_2(\omega)$ corresponding to the $\Delta R/R$ spectra in panel (a).

polarization. Three peaks are clearly distinguished, two positive peaks centered at $\sim 0.6\,\text{eV}$ and $\sim 2.0\,\text{eV}$ and a negative one at $\sim 1.5\,\text{eV}$. The full-widths of the peaks are all $\sim 0.4 - 0.5\,\text{eV}$.

The $\Delta\epsilon_2$ spectra in Fig. 5-4(b) are very different from those in Fig. 5-3(b) for the carrier modulation configuration. This shows that the change in reflectivity in the depletion region is dominated by electric field modulation rather than the change in the carrier concentration. The most important new feature seen in Fig. 5-4(b) is the strong negative peak at $\sim 1.5\,\text{eV}$. Since a positive voltage causes a decrease of the electric field in the space-charge region, this negative signal means that a $\sim 1.5\,\text{eV}$

sub-gap absorption is enhanced by an increasing field strength.

Electroreflectance has been studied in a variety of systems[61]. For covalent semiconductors the electric field modulation causes sharp resonances in the vicinity of critical points in the electronic density of states, the Franz-Keldysh effect. The width of these resonances scales with the dc electric field $\vec{E}$ as $(\hbar^2 e^2 E^2/2m^*)^{1/3}$ and lies typically in the energy range $0.001 - 0.01\,\mathrm{eV}$. For La_2CuO_{4+y} with $m^* \sim 2m_o$ peak-widths of order $0.5\,\mathrm{eV}$ correspond to electric fields of strength $\sim 1 \times 10^7\,\mathrm{Volt/cm.}$, almost two orders of magnitudes larger than those applied. Moreover, also the structure of the resonances is inconsistent with a Franz-Keldysh mechanism. Near a band edge, the main portion of the Franz-Keldysh resonance lies above the band gap, not far below as in Fig. 5-4(b). In semiconductors with large intrinsic electric fields, i.e. phonons or disorder, the band edge has an exponential tail induced by the internal electric fields. In these systems the effect of the applied electric field is to modulate the internal electric fields, effectively shifting the random-field-broadened band edge[99][61, p.265]. Such a mechanism does not explain the broad resonance far below the charge transfer edge observed in Fig. 5-4(b).

The usual mechanisms leading to electroreflectance cannot explain the broad features we observe. Based on our discussion of the crystal-field excitations in section 5.1 we will in the next section consider electric field induced hybridization between d and p symmetry states. The mixing of even and odd parity states increases with increasing electric field, making the crystal-field transitions weakly dipole allowed as well as weakening the strength of the charge-transfer excitation. As opposed to the more conventional mechanisms, electric field induced hybridization is compatible with the structure of the electroreflectance spectra. The positive $2.0\,\mathrm{eV}$ peak and the negative $1.5\,\mathrm{eV}$ peak observed in the $\Delta\epsilon_2(\omega)$ spectra in Fig. 5-4(b) are naturally explained as transfer of spectral weight from the charge-transfer band to the crystal-field excitations with increased hybridization.

5.3 Electric Field Enhanced Crystal-Field Excitations

The effect of the electric field is to destroy the inversion symmetry of the Cu site. With the crystal structure lacking inversion symmetry, parity is no longer a good quantum number and the electronic states transform as a combination of even and odd parity states. This hybridization is what gives rise to a transfer of strength from the charge-transfer excitation to the crystal-field excitations. Depending on the symmetry of the perturbing electric field, different sets of crystal-field excitations become possible.

5.3.1 Selection rules

Applying a tight-binding expansion of the wave functions we ignore next nearest neighbor interactions and only consider a CuO_6 cluster with two apical and four in-plane O ions positioned around the central Cu ion in a tetragonal D_{4h} symmetry as shown in Fig. 5-5. Within the cluster approximation, the undoped system corresponds to one hole per CuO_6 cluster. Optical excitations are described as transitions from the one-hole ground state to the one-hole excited states on the cluster. Counting three p states per oxygen ion and five d states for the central Cu ion, we have a total of 23 one-hole states. That makes 22 possible transitions to consider! In our discussion we are only interested to determine if a specific transition is dipole allowed; that is, we must find out if the corresponding transition matrix is zero or not. For this purpose it is enough to consider the symmetries of the different states and not the actual wave-functions. In this process we will express the respective symmetries with a representation. For example, the oxygen p_x orbital transforms as x; thus x is a representation of the symmetry of the true wave-function p_x. For the D_{4h} point group the representations of all possible wave-functions can be expressed as a sum over only

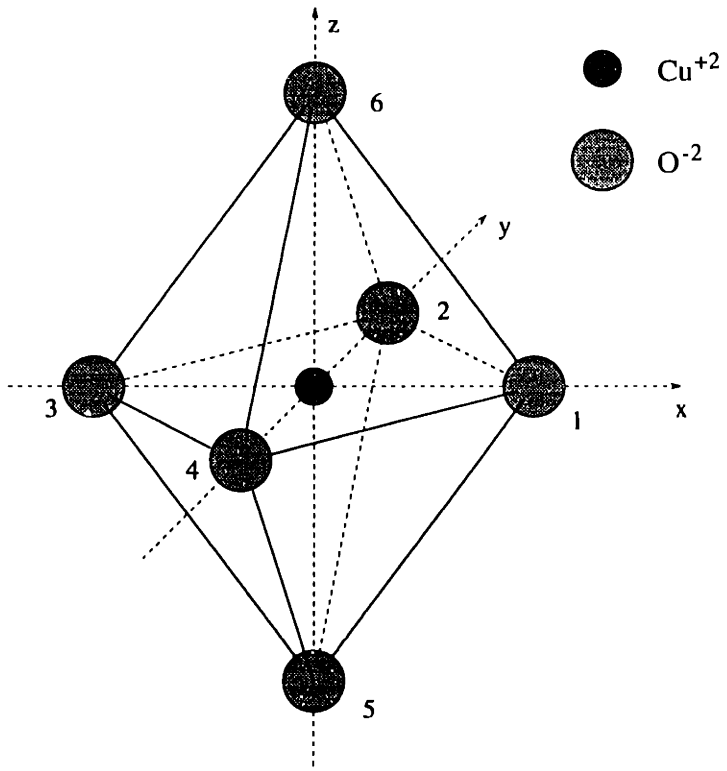

Figure 5-5: Schematic of the CuO_6 cluster with point group D_{4h}.

five different *irreducible* representations. Each irreducible representation can appear as both even (gerade) and odd (ungerade) under inversion. Thus the 23 different states transform in a maximum of ten different ways. In table 5.1 we have listed all the irreducible representations with the corresponding orthonormal basis set as given by Mila*et al.*[98]. We see that only eight of the irreducible representations are used. No states transform according to A_{1u} and B_{1u}. Note that the number of irreducible representations is solely determined by the symmetry of the crystal structure and is independent of the size of the cluster under consideration. For a true crystal with $\sim 10^{22}$ clusters, the $\sim 10^{23}$ different states will still transform in eight different ways.

The electric dipole transition matrix between an initial state $|i>$ and a final state $|f>$ is expressed as

$$M_{fi} = <\Psi_f|\vec{\eta}\cdot\vec{r}|\Psi_i> \tag{5.1}$$

		Cu states	O states
A_{1g}	z^2, x^2+y^2	d_{z^2}	$\frac{1}{2}(p_x^1+p_y^2-p_x^3-p_y^4)$, $\frac{1}{\sqrt{2}}(p_z^5-p_z^6)$
A_{2g}			$\frac{1}{2}(p_y^1-p_x^2-p_y^3+p_x^4)$
B_{1g}	x^2-y^2	$d_{x^2-y^2}$	$\frac{1}{2}(p_x^1-p_y^2-p_x^3+p_y^4)$
B_{2g}	xy	d_{xy}	$\frac{1}{2}(p_y^1+p_x^2-p_y^3-p_x^4)$
E_g	yz, zx	d_{yz}, d_{zx}	$\frac{1}{\sqrt{2}}(p_z^1-p_z^3)$, $\frac{1}{\sqrt{2}}(p_z^2-p_z^4)$ $\frac{1}{\sqrt{2}}(p_x^6-p_x^5)$, $\frac{1}{\sqrt{2}}(p_y^6-p_y^5)$
A_{2u}	z		$\frac{1}{\sqrt{2}}(p_z^5+p_z^6)$, $\frac{1}{2}(p_z^1+p_z^2+p_z^3+p_z^4)$
B_{2u}			$\frac{1}{2}(p_z^1-p_z^2+p_z^3-p_z^4)$
E_u	x, y		$\frac{1}{\sqrt{2}}(p_x^1+p_x^3)$, $\frac{1}{\sqrt{2}}(p_x^2+p_x^4)$ $\frac{1}{\sqrt{2}}(p_y^1+p_y^3)$, $\frac{1}{\sqrt{2}}(p_y^2+p_y^4)$ $\frac{1}{\sqrt{2}}(p_x^5+p_x^6)$, $\frac{1}{\sqrt{2}}(p_y^5+p_y^6)$

Table 5.1: Irreducible representations and basis functions for one hole in the CuO_6 cluster with D_{4h} symmetry. The numbering notation is defined in Fig. 5-5. (After [98])

where $\vec{\eta}$ is the polarization vector. In order to show that a specific matrix element $< f|\vec{\eta}\cdot\vec{r}|i >$ is non-zero, it is enough to show that $\vec{\eta}\cdot\vec{r}|i>$ and $|f>$ have common irreducible representations. Let $\Gamma^{(i)}$ and $\Gamma^{(\vec{\eta})}$ represent the symmetries of the initial state $|i>$ and the operator $\vec{\eta}\cdot\vec{r}$ respectively. The symmetry of $\vec{\eta}\cdot\vec{r}|i>$ is then given by the direct product representation $\Gamma^{(\vec{\eta})}\otimes\Gamma^{(i)}$. The direct product multiplication table for the D_{4h} point group is given in Table 5.2. Thus, the matrix element $< f|\vec{\eta}\cdot\vec{r}|i >= 0$ unless the direct product representation $\Gamma^{(\vec{\eta})}\otimes\Gamma^{(i)}$ contains the irreducible component $\Gamma^{(f)}$.

As a warm up let us first find the electric-dipole allowed transitions in an unperturbed crystal. In the initial state the hole is in the $d_{x^2-y^2}$ (B_{1g}) symmetry state. To obtain the electric-dipole allowed final states we must first find the representations

	A_1	A_2	B_1	B_2	E
A_1	A_1	A_2	B_1	B_2	E
A_2	A_2	A_1	B_2	B_1	E
B_1	B_1	B_2	A_1	A_2	E
B_2	B_2	B_1	A_2	A_1	E
E	E	E	E	E	$A_1 + A_2 + B_1 + B_2$

Table 5.2: Direct product multiplication table for the D_4 point group

according to which $\vec{\eta} \cdot \vec{r}$ transforms. From Table 5.1 we find that the two in-plane coordinates x, y transform according to E_u while the out-of-plane coordinate z transforms according to the A_{2u} representation. For polarization parallel to the CuO_2 planes the direct product representation is $\Gamma^{(\vec{\eta})} \otimes \Gamma^{(i)} = E_u \otimes B_{1g} = E_u$. The final state must therefore have E_u symmetry. This includes the six wave-functions listed in Table 5.1. The dominant charge-transfer excitations are transitions to the $(p_x^2 + p_x^4)$ and $(p_y^1 + p_y^3)$ states since these are the only E_u states for which the surrounding p orbitals point towards the central Cu ion and have consequently the largest overlap with the Cu d orbitals. For polarization perpendicular to the CuO_2 planes, the direct product representation is $\Gamma^{(\vec{\eta})} \otimes \Gamma^{(i)} = A_{2u} \otimes B_{1g} = B_{2u}$. In Table 5.1 we find only one state with this symmetry. The corresponding basis function is a sum over the p_z orbitals for the four in-plane oxygen ions and has consequently negligible overlap with the Cu d orbitals. This effect is reflected in the absence of out-of-plane absorption. Thus applying symmetry considerations alone we can understand the strong anisotropy observed in the charge-transfer excitation.

Consider now the effect of an applied uniform electric field. We start with a set of eight unperturbed states $|\Psi_n^0>$ transforming according to the eight inequivalent irreducible representations in table 5.1. In the presence of a constant electric field $\vec{E}$

the perturbed wave function $|\Psi_n>$ can to first order be written as

$$|\Psi_n> = |\Psi_n^0> + \sum_{m\neq n} \frac{<\Psi_m^0|V|\Psi_n^0>}{\varepsilon_n^0 - \varepsilon_m^0} |\Psi_m^0> \tag{5.2}$$

where $V = -e\vec{E}\cdot\vec{r}$. We are interested in the electric field induced transition matrix elements between two nominally even parity states. By inserting Eq. (5.2) into the electric dipole transition matrix Eq. (5.1), the first non-vanishing terms are

$$\begin{aligned} M_{fi} &= e\sum_{n\neq i} \frac{<\Psi_f^0|\vec{\eta}\cdot\vec{r}|\Psi_n^0><\Psi_n^0|\vec{E}\cdot\vec{r}|\Psi_i^0>}{\varepsilon_i^0 - \varepsilon_n^0} \\ &+ e\sum_{n\neq f} \frac{<\Psi_f^0|\vec{E}\cdot\vec{r}|\Psi_n^0><\Psi_n^0|\vec{\eta}\cdot\vec{r}|\Psi_i^0>}{\varepsilon_f^0 - \varepsilon_n^0} \end{aligned} \tag{5.3}$$

The electric field induced electric dipole transitions can be viewed as a two-step process where the transition from the ground state to a final state of equal parity goes through an intermediate state of opposite parity. Considering the first term in Eq. (5.3), the intermediate state $|\Psi_n^0>$ must transform according to the direct product representation $\Gamma^{(\vec{E})}\otimes\Gamma^{(i)}$ for $<\Psi_n^0|\vec{E}\cdot\vec{r}|\Psi_i^0> \neq 0$. Here $\Gamma^{(\vec{E})}$ represents the irreducible representation of the operator $\vec{E}\cdot\vec{r}$. The electric dipole allowed final states will be those where $<\Psi_f^0|\vec{\eta}\cdot\vec{r}|\Psi_n^0> \neq 0$. The final state must consequently transform according to $\Gamma^{(\vec{\eta})}\otimes\Gamma^{(n)} = \Gamma^{(\vec{\eta})}\otimes(\Gamma^{(\vec{E})}\otimes\Gamma^{(i)})$. Similarly, the second term in Eq. (5.3) is non-zero only if the final state transform according to $\Gamma^{(\vec{E})}\otimes\Gamma^{(n)} = \Gamma^{(\vec{E})}\otimes(\Gamma^{(\vec{\eta})}\otimes\Gamma^{(i)})$. Thus the electric field induced matrix element M_{fi} is non-zero only if the irreducible representation for the final state $\Gamma^{(f)}$ is included in either of the two direct product representations

$$\begin{gathered} \Gamma^{(\vec{\eta})}\otimes(\Gamma^{(\vec{E})}\otimes\Gamma^{(i)}) \\ \Gamma^{(\vec{E})}\otimes(\Gamma^{(\vec{\eta})}\otimes\Gamma^{(i)}). \end{gathered} \tag{5.4}$$

From Eq. (5.4) we recognize that the set of direct product representations is in-

variant with respect to interchanging the electric field and the polarization vectors. Consequently, we only need to consider six different electric field and polarization configurations.

Consider first the situation in which the electric field and the polarization vector both are perpendicular to the CuO_2 planes. That is, consider the $(E\hat{z}, \hat{z})$ configuration where the first vector is the electric field $\vec{E}$ and the second vector is the polarization $\vec{\eta}$. In this configuration both $\vec{E} \cdot \vec{r}$ and $\vec{\eta} \cdot \vec{r}$ transform according to $\Gamma^{(\vec{E})} = \Gamma^{(\vec{\eta})} = A_{2u}$. The initial state $d_{x^2-y^2}$ transforms according to $\Gamma^{(i)} = B_{1g}$. By applying Eq. (5.4) the final state must transform according to

$$A_{2u} \otimes (A_{2u} \otimes B_{1g}) = A_{2u} \otimes B_{2u} = B_{1g}. \tag{5.5}$$

Only final states of B_{1g} symmetry are electric dipole allowed. In other words, with the applied electric field and the polarization vector both perpendicular to the CuO_2 planes, the only electric field induced crystal-field excitation corresponds to a transition from the Cu based to the O based B_{1g} symmetry state. However, this field induced transition will be vanishingly small since the intermediate state B_{2u} has a negligible overlap with the Cu d orbitals.

Consider now the situation where the electric field vector and the polarization vector both are parallel to the CuO_2 plane. Thus both $\vec{E} \cdot \vec{r}$ and $\vec{\eta} \cdot \vec{r}$ transform according to E_u and the set of direct product representations in Eq. (5.4) reduces to

$$E_u \otimes (E_u \otimes B_{1g}) = A_{1g} + A_{2g} + B_{1g} + B_{2g}. \tag{5.6}$$

Final states which transform according to any of these four irreducible representations are electric dipole allowed. Three different configurations have the electric field and the polarization vector parallel to the CuO_2 plane: $(E\hat{x}, \hat{x})$, $(E\hat{y}, \hat{y})$ and $(E\hat{x}, \hat{y})$. To determine the final states corresponding to the different configurations we consider $\hat{x}$ and $\hat{y}$ separately.

Both x and y are irreducible representations transforming according to E_u as seen from Table 5.1. Specifically, $x \otimes B_{1g} = x$, $y \otimes B_{1g} = y$, $x \otimes x = x^2$, $y \otimes y = y^2$ and $x \otimes y = xy$. From this we find that the set of direct-product representations in Eq. (5.4) reduces to x^2 for the $(E\hat{x}, \hat{x})$ configuration and y^2 for the $(E\hat{y}, \hat{y})$ configuration. Neither x^2 nor y^2 are irreducible representations, as seen from Table 5.1, but transform according to $A_{1g} + B_{1g}$ and $A_{1g} - B_{1g}$, respectively. Thus for $(E\hat{x}, \hat{x})$ and $(E\hat{y}, \hat{y})$ final states of both A_{1g} and B_{1g} symmetry are dipole allowed. For the $(E\hat{x}, \hat{y})$ configuration, Eq. (5.4) reduces to xy. This is an irreducible representation and transforms according to B_{2g}.

The two final configurations to consider are $(E\hat{x}, \hat{z})$ and $(E\hat{y}, \hat{z})$. For these the electric field vector lies in the CuO_2 plane and transforms as E_u while the polarization vector points perpendicular to the plane and transforms as A_{2u}. By inserting these irreducible representations in Eq. (5.4) the final state is found to transform according to E_g. Alternatively, by treating $\hat{x}$ and $\hat{y}$ separately as in the previous paragraph, the electric dipole allowed final states for the configurations $(E\hat{x}, \hat{z})$ and $(E\hat{y}, \hat{z})$ are found to transform according to zx and yz, respectively. As seen from Table 5.1, these are both irreducible representations and transform according to E_g.

In Table 5.3 we have summarized the above results indicating the symmetries of the electric dipole allowed final states for all possible combinations of polarization of light and electric-field vectors. In this table d_{zx} and d_{yz} represent both Cu and O states which transform according to the representations zx and yz, respectively. The excitation energies for transitions from the $d_{x^2-y^2}$ symmetric ground state to other copper based states will in general be much smaller than excitation energies to even parity oxygen states since the latter are charge transfer excitations which include the energy cost of a fully occupied Cu $3d$ shell. The lowest-energy transitions, expected to be excitations of holes to the d_{z^2} and d_{xy} states[12], are predicted only for the in-plane spectra whereas transitions to the d_{yz} and d_{zx} states are possible for all polarizations.

For the field-modulation spectra in Fig. 5-4 the uniform electric field is parallel

Electric	Polarization		
Field	$\hat{x}$	$\hat{y}$	$\hat{z}$
E_x	A_{1g}, B_{1g}	B_{2g}	d_{zx}
E_y	B_{2g}	A_{1g}, B_{1g}	d_{yz}
E_z	d_{zx}	d_{yz}	(B_{1g})

Table 5.3: Symmetries of the final states in dipole-allowed crystal-field transitions for different combinations of polarization and electric-field. Here $\hat{x}$ and $\hat{y}$ are the in-plane lattice vectors. Brackets indicate that this transition is very weak.

to the CuO_2 plane and normal to the polarization direction of the incoming light. From Table 5.3 we find that in this configuration the only in-plane transition affected is $d_{x^2-y^2} \rightarrow d_{xy}$. In the electroreflectance spectra, only the 1.5 eV absorption is enhanced by the electric field. Thus, the 1.5 eV band is consistent with transitions to states of d_{xy} symmetry while the 0.5 eV band is not. Furthermore, since no structure is observed in the out-of-plane polarization, the 0.5 eV band is also inconsistent with transitions to states of d_{yz},d_{zx} symmetry. Among the Cu based crystal-field excitations, we are then left with a final state of d_{z^2} symmetry. This is certainly consistent with the interpretation of Perkins *et al.*[54] as well as with cluster calculations favoring d_{z^2} and d_{xy} as the two lowest energy excited states[12]. The observation of a positive peak at 0.5 eV in Fig. 5-4(b) probably results from the small change in the carrier concentration.

5.3.2 Oscillator strength

As an independent check on the validity of the electric field induced hybridization picture, consider the expected oscillator strength for such a mechanism. The oscillator strength associated with an excitation, defined in Eq. (4.8), depends on the matrix element M_{fi}, the excitation energy $\varepsilon_f - \varepsilon_i$ as well as the effective mass

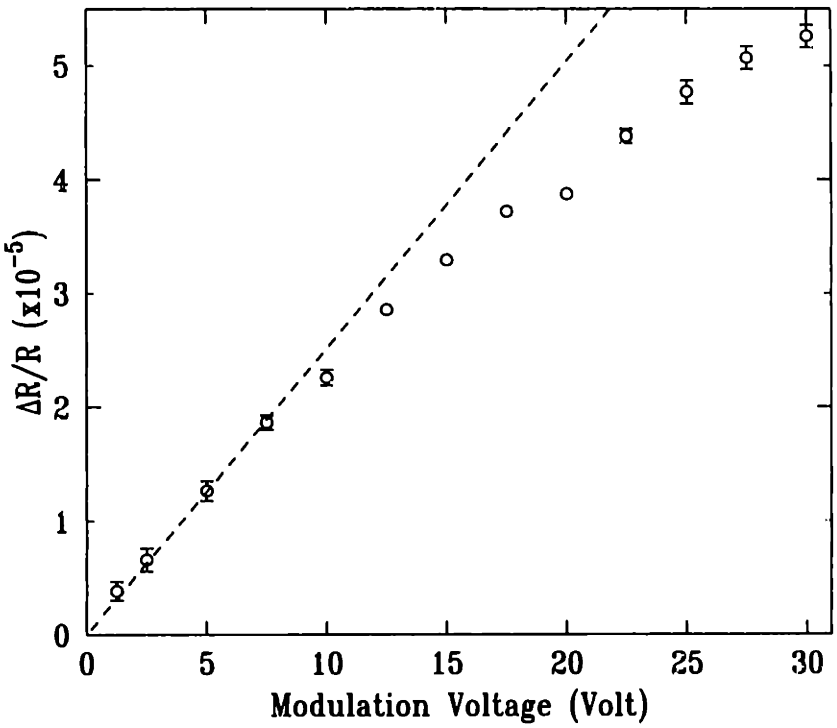

Figure 5-6: Strength of the electroreflectance signal at the primary modulation frequency ν as a function of the peak-to-peak voltage applied across the metal-insulator-semiconductor structure.

m^*. From Eq. (5.3) we see that the strength of the matrix element M_{fi} is of order $M_{fi} \sim (2\,e\,E\,a^2/\Delta\varepsilon_{p,d})^2$ where a is the effective exciton radius and $\Delta\varepsilon_{p,d}$ is the energy difference between the hybridized p and d symmetry states, typically of order the charge-transfer gap. By substituting this expression for the matrix element M_{fi} in Eq. (4.8), the effective number of carriers involved in an electric field induced crystal-field excitation is of order

$$N^*_{eff} \sim \frac{2m^*}{3\hbar^2}\left(\frac{2\,e\,E\,a^2}{\Delta\varepsilon_{p,d}}\right)^2 (\varepsilon_f - \varepsilon_i). \tag{5.7}$$

Here N^*_{eff} is expressed in units of the Cu ion density. The modulated electric field within the insulating Si_3N_4 layer corresponds to $20\cos(\nu t)$ V applied across 1000 Åwith frequency ν. The static dielectric constants in Si_3N_4 and La_2CuO_4 are 4.2 and 30, respectively, yielding an effective modulated electric field within the depletion

region of order $\Delta E = (4.2/30) \times (20V/1000\text{Å}) = 2.8 \times 10^5$ V/cm peak-to-peak. The applied electric field comes in addition to a static electric field E_s present within the depletion layer. The total electric field is then $E = E_s + \frac{1}{2}\Delta E \cos(\nu t)$ and

$$E^2 = E_s^2 + E_s \Delta E \cos(\nu t) + \frac{1}{8}(\Delta E)^2(1 + \cos(2\nu t)) \tag{5.8}$$

The $\Delta R/R$ spectra displayed in Fig. 5-4 were measured at the primary modulation frequency ν with a strength sublinear in ΔE as seen in Fig. 5-6. No signal was detected above the $\sim 1\%$ noise level at the double frequency 2ν implying that $E_s/\Delta E \geq 10$. The modulated oscillator strength of the crystal-field excitation is then given by Eq. (5.7) by substituting E^2 with $E_s \Delta E/\sqrt{2}$. The factor of $\sqrt{2}$ in the denominator reflects that the measured modulation signals are RMS, not peak-to-peak values. With $\Delta\epsilon_{p,d} \sim 2\,\text{eV}$, an excitation energy $\epsilon_f - \epsilon_i \sim 1.5$ and an effective ionic radius of order $a \simeq 1$ Å, the expected number of carriers involved in the 1.5 electroreflectance band is of order $N^*_{eff}\, m_o/m^* \sim 3E_s/(4\Delta E) \times 10^{-6}$ per Cu ion. With $E/\Delta E \sim 10$ we find $N^*_{eff}\, m_o/m^* \sim 7 - 8 \times 10^{-5}$ per Cu ion.

The experimental oscillator strength is determined by integrating the undoped $\Delta\epsilon_2$ spectrum in Fig. 5-4(b) according to Eq. (1.1). This procedure gives a total oscillator strength for the 1.5 eV excitation of $N^*_{eff}\, m_o/m^* = 3.9 \times 10^{-6}$ per Cu ion. Given the uncertainty related to the strength of the static electric field E_s, the crystal-field estimate agrees with the experimental oscillator strength within a factor of 2-5. This close agreement supports the applicability of the electric-field induced hybridization picture.

5.3.3 Discussion

Both $d_{x^2-y^2} \rightarrow d_{z^2}$ and $d_{x^2-y^2} \rightarrow d_{xy}$ are Raman allowed transitions with B_{1g} and A_{2g} symmetry, respectively. An A_{2g} symmetric Raman excitation centered around 1.5 eV has recently been observed in $YBa_2Cu_3O_6$, $PrBa_2Cu_3O_6$ and Gd_2CuO_4 [100],

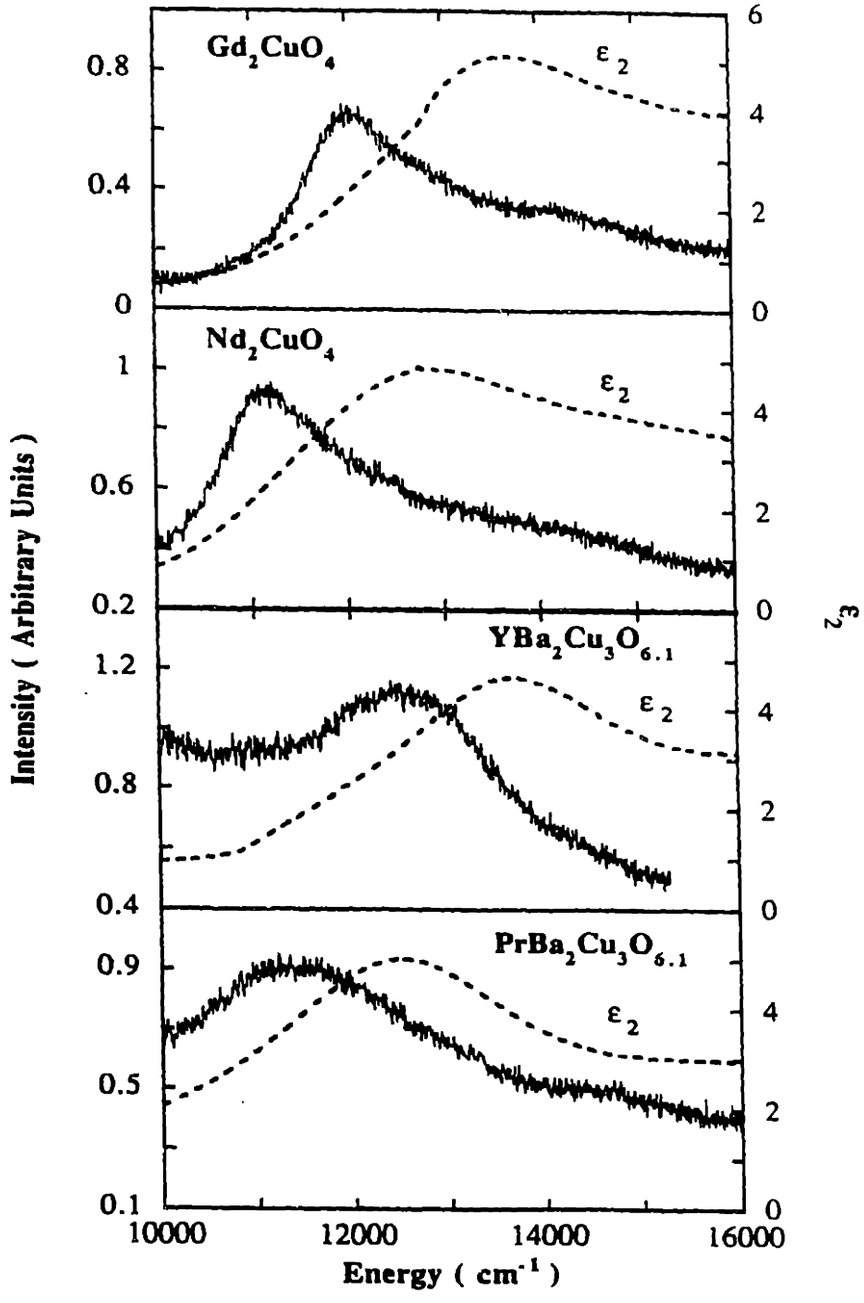

Figure 5-7: Raman spectra (in relative cm^{-1} shift) and ϵ_2 (in absolute cm^{-1}) for four different insulating cuprates. The Raman spectra where taken in A_{2g} geometry with 3.81 eV excitation (From [100]).

suggesting that this excitation is universal for the insulating copper oxides. Both the symmetry and the excitation energy are in agreement with our electroreflectance data. Raman studies also reveal a B_{1g} symmetric excitation centered at 0.4 eV in the copper oxides, commonly interpreted as a two-magnon excitation[101]. The line-shape, however, is much wider than expected for such an excitation and is presently not understood. As we discussed in section 5.1, the B_{1g} symmetric crystal-field exciton and the two-magnon excitation are expected to interact implying that the 0.4 eV peak seen in Raman scattering is neither a pure two-magnon excitation nor a pure crystal-field exciton, but a hybrid of these two excitations.

Excitations of holes to the degenerate d_{xz}, d_{yz} states should be seen in the out-of-plane electric field modulation spectra with a strength of the same order as the $d_{x^2-y^2} \rightarrow d_{xy}$ transition. The absence of such features in Fig. 5-4 suggests that these transitions lie outside our spectral range. This conclusion is supported by Geserich *et al.*[102] who associated these transitions with an absorption peak at 3.0 eV.

Cluster calculations[12] predict the lowest-energy crystal-field transition to be excitation of holes to the d_{z^2} state with the d_{xy} state and the degenerate d_{yz}, d_{xz} states at successively higher energies. Although our electroreflectance spectra support this energy-level scheme, calculations predict a minimum excitation energy in the range $0.9 - 1.6$ eV. Moreover, the cluster calculations also find a splitting between the d_{xy} and d_{yz}, d_{xz} states of only ~ 0.1 eV. These estimates are of order 1 eV smaller than the value consistent with our data.

Part of the oscillator strength of the crystal-field excitations is expected to come from the charge-transfer excitation. Transfer of oscillator strength from the charge transfer band to the mid-infrared absorption bands is seen in both electron- and hole doped copper oxides[52, 35]. The effect is clearly demonstrated for the field modulation spectra in Fig. 5-4(b) by the positive 2.0 eV peak accompanying the negative 1.5 eV peak.

The field modulation spectrum for the undoped crystal (Fig. 5-4(b)) does not dis-

play the sharp structure observed in the crystal-field excitation spectrum[54] measured by transmission through $\sim 100\,\mu$m thick undoped crystals. Since the band width we observe (Fig. 5-4(b)) is only weakly dependent upon chemical doping, the broadening is probably not caused by defects. A more likely scenario is that the broadening is caused by the strong non-uniform electric field present within the depletion layer.

Chapter 6

Conclusion

6.1 Syntheses of the Results

We have in this thesis studied the optical and infrared electronic excitations in undoped and lightly oxygen doped La_2CuO_{4+y} by means of polarization and temperature dependent reflectivity and electroreflectance measurements. In particular, we have demonstrated that both free and localized holes interact with optical phonon modes and form large polarons.

The charge-transfer excitation

The lowest energy electronic excitation in undoped La_2CuO_4 is the charge transfer excitation. We showed that the charge-transfer excitation spectrum and its temperature dependence can be understood if both Fröhlich electron-phonon interaction and electron-hole correlation is taken into account. Only a short range electron-hole interaction is found to be consistent with the charge-transfer spectrum. The integrated strength of the short-range electron-hole potential is of the order expected from parameters of the extended Hubbard model. The measured polaron coupling constant $\alpha_p = 5.7$ is consistent with the dielectric properties of La_2CuO_4. The photoexcited carriers are confined to the CuO_2 planes and can consequently only couple

to LO phonon modes of E_u symmetry. The measured averaged excitation energy $\hbar\omega_0 = 0.043\,\mathrm{eV}$ of the interaction phonons was found to be consistent with a dominant coupling to two LO E_u Cu-O bond-bending modes at 0.034 and 0.057 eV, respectively. We also discussed additional evidence for such polaron formation of photo-excited carriers provided by photo-induced absorption and Raman scattering.

Impurity absorption

Upon doping three mid-infrared absorption bands appear within the charge-transfer gap at 0.13, 0.5 and 1.5 eV respectively. We have shown that spectral weight is transferred between free carrier conductivity and a photo-ionization band of impurity-bound carriers. Thus the lowest energy electronic excitation in lightly doped La_2CuO_{4+y} corresponds to photo-ionization of localized holes. The large difference between the optical 0.13 eV and the thermal 0.035 eV ionization energy indicates that the impurity states are stabilized by lattice distortion. We have demonstrated that the line shape as well as the temperature dependence is consistent with absorption from polaronic impurities. Similar behavior seen in photo-induced absorption spectra of both electron and hole doped copper-oxides suggest that photo-ionization of localized polarons is a general feature of the insulation copper oxides.

Crystal-field excitations

While we were able to identify the 0.13 eV absorption band mainly through its characteristic temperature dependence, the 0.5 and 1.5 eV infrared absorption bands lack both sharp spectral features and strong temperature dependence. In pursuit of the microscopic origin for these excitations we measured the reflectivity spectrum with respect to a modulated external electric field. The electroreflectance spectra were measured in two different configurations. Depending on the electrode structure, the modulation resulted in addition of charge or variation of the electric field in the space charge region. By comparing the carrier modulation data with reflectivity of

doped and undoped La_2CuO_{4+y}, we found that the observed doping enhanced mid-infrared absorption is primarily caused by the excess holes in the CuO_2 layer rather than by the increased impurity or defect concentration that induces them. We found that the response of the 1.5 eV infrared band to electric field, both in strength and polarization dependence, is consistent with a $d_{x^2-y^2} \rightarrow d_{xy}$ transition. The response of the 0.5 eV band was found to be inconsistent with transitions to both d_{xy}, and d_{yz}, d_{zx} symmetry states, supporting a $d_{x^2-y^2} \rightarrow d_{z^2}$ interpretation. Both the energies and the symmetries of these excitations are in agreement with those of the crystal-field excitations and magnon sidebands observed in transmission through $\sim 100\,\mu$m thick undoped crystals[54]. Hence, excitons and sidebands emerge as natural candidates for the doping induced mid-infrared absorption.

6.2 Connections to the Superconducting State

The nature and origin of the mid-infrared absorption bands have been a topic of great interest. This interest is particularly fueled by optical conductivity spectra on metallic crystals which indicate the presence of a mid-infrared band even in the superconducting state. At high doping levels the term "mid-infrared band" refers to what is left of the optical conductivity spectrum in the normal state after a free carrier (Drude) component is subtracted off. This spectrum resembles a broad temperature independent absorption band with a peak in the energy range $0.1 - 0.2$ eV[52]. This in contrast to the three, clearly separated, bands at $0.13, 0.5$ and 1.5 eV in the insulating phase. One possible interpretation is [52] that the mid-infrared band in the insulating and superconducting phase have the same origin, and is simply broadened and shifted to lower energies with the introduction of carriers. An alternative approach questions the presence of a mid-infrared absorption band in the normal state and describes, instead, the infrared absorption as entirely due to free carriers with energy dependent scattering rate and effective mass. Such behavior is observed in a

variety of conducting systems and is caused by interaction of the free carriers with optically inactive excitations. An example of such an interaction is inelastic scattering from acoustical phonons in conventional metals. Single-component analyses of the optical conductivity for $YBa_2Cu_3O_{6+y}$[8, 9] with $y \geq 0.6$ and optimally doped $La_{2-x}Sr_xCuO_4$[10] find an effective scattering rate which scales like $\hbar/\tau^* \sim k_BT + \hbar\omega$ at low frequencies with a temperature and frequency dependent mass enhancement of order ~ 2. This behavior is in qualitatively agreement with expected behavior for free charge carriers interacting with spin-fluctuations[33, 34]. The observed features are also consistent with predictions for nested Fermi liquids[56] and marginal Fermi liquids[57].

In the overdoped regime no trace of a separate mid-infrared band remains [35] and the electronic excitations acquire the nature of a Fermi liquid. Thus in the overdoped region both intrinsic and doping induced carriers seem to occupy states of the same character. This stands in sharp contrast to the insulating limit where the intrinsic and extrinsic carriers occupy states of very different character. The intrinsic holes are localized on the Cu ions in a strongly correlated antiferromagnetic ground state. The doping induced holes, on the other hand, occupy oxygen derived states where Coulomb correlations are unimportant.

Due to the strong correlation effects, the insulating copper oxides have two types of electronic excitations, charged and neutral respectively. We have in this thesis shown that the charged electronic excitations (i.e. charge-transfer excitation and photoionization) display a predominant coupling to vibrational excitations. The neutral excitations, however, display a predominant coupling to magnetic excitations. In the insulating phase these two types of electronic excitations are clearly distinct. In the superconducting regime their presence is much more illusive. To understand the nature of the normal state and the superconductivity it may be necessary to understand what happens with these excitations upon doping as the copper and oxygen derived states hybridize and merge until they eventually become indistinguishable in

the overdoped phase.

Appendix A

Optical Components

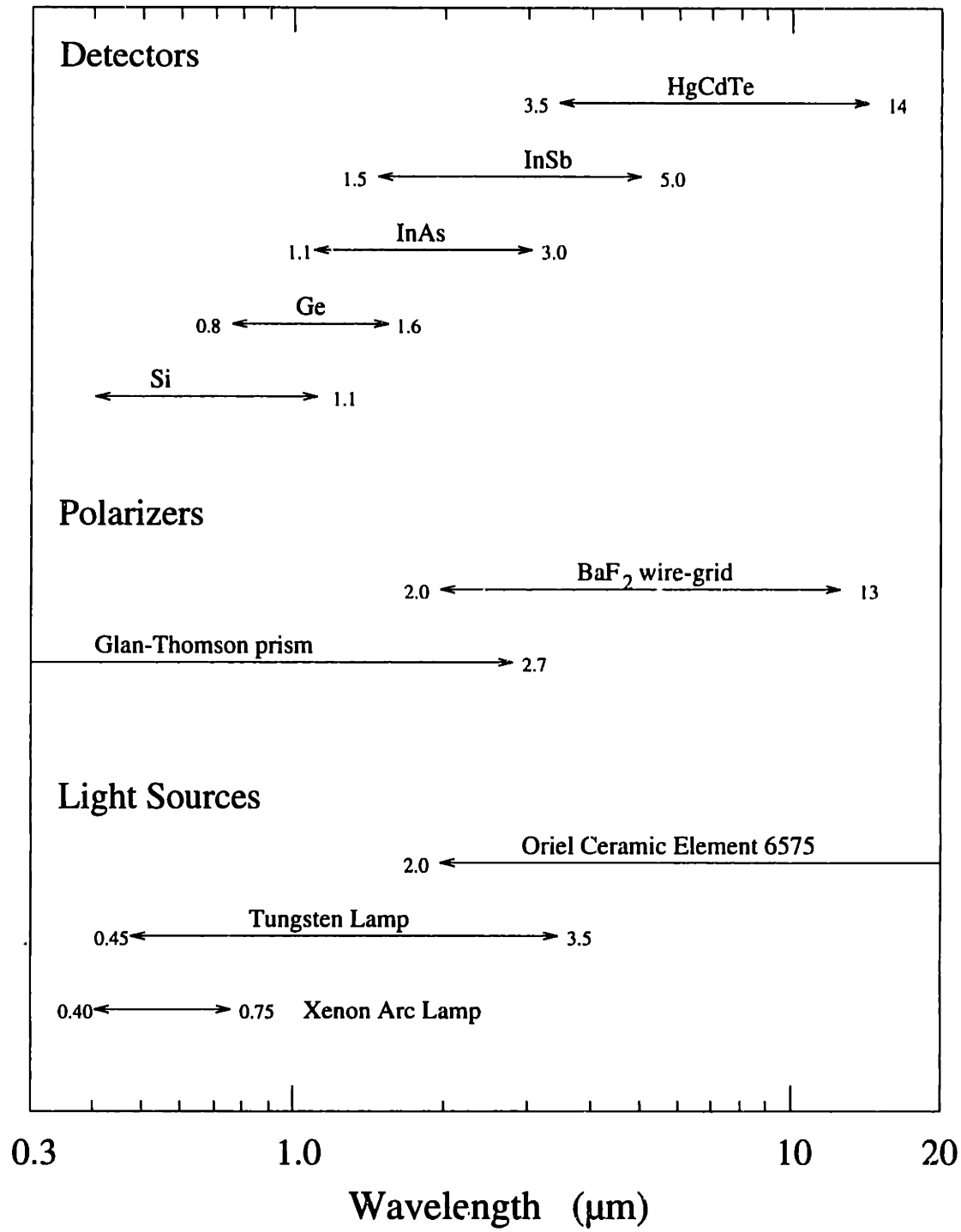

Figure A-1: Selection of detectors, polarizers and light sources as a function of wavelength. The Glan-Thomson prism polarizer has an average extinction ratio of $\sim 1 \times 10^5$. The double BaF_2 wire-grid polarizer has an average combined extinction ratio of $\sim 1 \times 10^4$. The high-wavelength limit for each photodetector corresponds to the band gap of the respective semiconductor. The low-wavelength limits, on the other hand, are not so well defined and the listed values are only approximate.

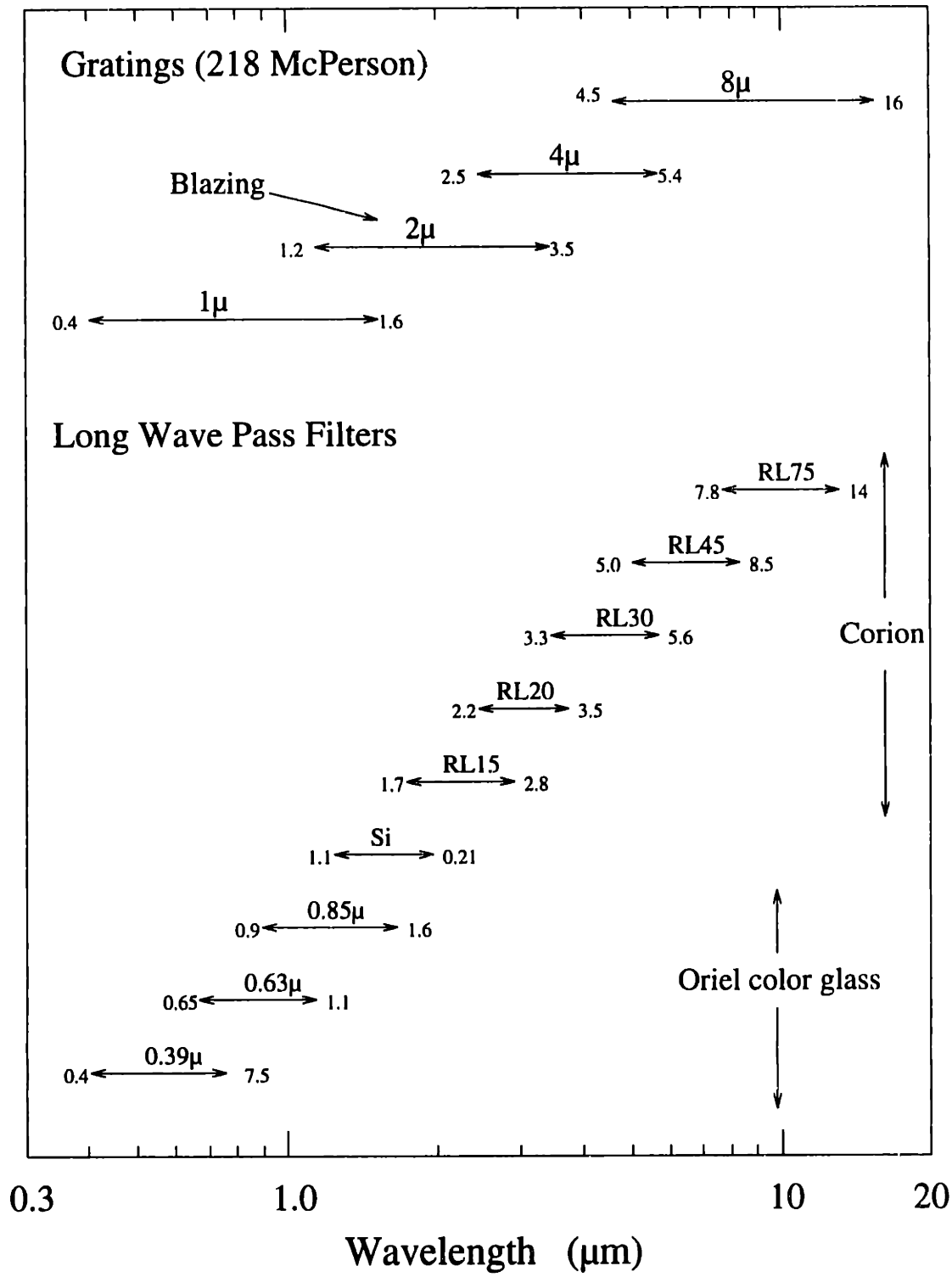

Figure A-2: Selection of gratings for the 218 McPerson monochromator and long wave pass filters as a function of wavelength. Oriel supplies a larger selection of glass filters in the $0.39 - 0.85\,\mu$m range than those listed.

Appendix B

Kramer-Kronig Transformations

The Kramer-Kronig transformations relate the real and the imaginary part of the dielectric function $\epsilon = \epsilon_1 + i\epsilon_2$:

$$\epsilon_1(\omega) - 1 = \frac{2}{\pi} P \int_0^\infty \frac{\omega' \epsilon_2(\omega)}{\omega'^2 - \omega^2} d\omega' \tag{B.1}$$

$$\epsilon_2(\omega) = -\frac{2\omega}{\pi} P \int_0^\infty \frac{\epsilon_1(\omega') - 1}{\omega'^2 - \omega^2} d\omega'. \tag{B.2}$$

A similar set of equations also applies to the reflectivity amplitude relating the phase θ with the absolute magnitude R. Specifically we write

$$\theta(\omega) = -\frac{\omega}{\pi} P \int_0^\infty \frac{\ln R(\omega')}{\omega'^2 - \omega^2} d\omega'. \tag{B.3}$$

The reflective amplitude is a function of the dielectric function given as

$$\sqrt{R}\, e^{i\theta} = \frac{n_r - 1 + i\, n_i}{n_r + 1 + i\, n_i}, \tag{B.4}$$

where the real and imaginary part of the refractive index is given as $\sqrt{\epsilon} = n_r + i\, n_i$.

In transforming the measured reflectivity to the real and imaginary part of the

dielectric function one first applies Eq. (B.3) to extract the phase of the reflectivity amplitude. Knowing both the magnitude and the phase of the reflectivity, the dielectric function is uniquely determined through Eq. (B.4). By inverting the the real and imaginary part of Eq. (B.4), the complex dielectric function can be expressed as

$$\epsilon_1 = n_r^2 - n_i^2 \tag{B.5}$$

$$\epsilon_2 = 2\, n_r\, n_i \tag{B.6}$$

where

$$n_r = \frac{1-R}{1+R-2\sqrt{R}\cos\theta} \tag{B.7}$$

$$n_i = \frac{2\sqrt{R}\sin\theta}{1+R-2\sqrt{R}\cos\theta}. \tag{B.8}$$

The Kramer-Kronig analysis of the modulated reflectivity spectrum $\Delta R/R$ is performed in a similar way by first obtaining the modulation $\Delta\theta$ in the phase angle θ. Since $\Delta\theta$ is small, we use the differential form of Eq. (B.3),

$$\Delta\theta(\omega) = -\frac{\omega}{\pi} P\int_0^\infty \frac{\Delta R(\omega')}{R(\omega')}\frac{d\omega'}{\omega'^2-\omega^2}. \tag{B.9}$$

The corresponding changes in the dielectric function can be obtained by differentiate the dielectric function as expressed in Eqs. (B.5 - B.8) with respect to R and θ. To first order one finds

$$\Delta\epsilon_1 = \frac{n_r}{2\,n_L}\left(n_r^2 - n_L^2 - 3\,n_i^2\right)\frac{\Delta R}{R} - \frac{n_i}{n_L}\left(3\,n_r^2 - n_L^2 - n_i^2\right)\Delta\theta \tag{B.10}$$

$$\Delta\epsilon_2 = \frac{n_i}{2\,n_L}\left(3\,n_r^2 - n_L^2 - n_i^2\right)\frac{\Delta R}{R} + \frac{n_r}{n_L}\left(n_r^2 - n_L^2 - 3\,n_i^2\right)\Delta\theta, \tag{B.11}$$

where n_L is the real refractive index of the transparent medium surrounding the

sample. In the metal-semiconductor configuration air is in direct contact with the reflective surface and $n_L = 1$. For the metal-insulator-semiconductor configuration, however, amorphous Si_3N_4 is the effective surrounding medium with $n_L = 2.05$.

The Kramer-Kronig relations Eqs. (B.1)-(B.3) and (B.9) are principle-part integrals. These integrals cannot be directly numerically evaluated since the integrands diverge at $\omega' = \omega$. Depending on if the singularity is approached from either the negative $\omega' \to \omega^-$ or the positive $\omega' \to \omega^+$ limit, the diverging integrands have opposite signs. Thus by adding the positive and negative limit, the diverging integrands cancel and the Kramer-Kronig integrals are well defined. Specifically we write

$$\begin{aligned} \theta(\omega) &= -\frac{\omega}{\pi} P \int_0^\infty \frac{\ln R(\omega')}{\omega'^2 - \omega^2} d\omega' \\ &= -\frac{\omega}{\pi} \lim_{\epsilon \to 0} \int_0^{\omega-\epsilon} + \int_{\omega+\epsilon}^{2\omega} + \int_{2\omega}^\infty \frac{\ln R(\omega')}{\omega'^2 - \omega^2} d\omega'. \end{aligned} \tag{B.12}$$

We apply the substitution $\omega' = 2\omega - \omega''$ to the second integral which yields

$$\begin{aligned} \int_{\omega+\epsilon}^{2\omega} \frac{\ln R(\omega')}{\omega'^2 - \omega^2} d\omega' &= - \int_{\omega-\epsilon}^0 \frac{\ln R(2\omega - \omega'')}{(2\omega - \omega'')^2 - \omega^2} d\omega'' \\ &= \int_0^{\omega-\epsilon} \frac{\ln R(2\omega - \omega')}{(2\omega - \omega')^2 - \omega^2} d\omega' \end{aligned} \tag{B.13}$$

By substituting the second integral in Eq. (B.12) with Eq. (B.13) the phase θ of the reflectivity amplitude can be expressed as

$$\theta(\omega) = -\frac{\omega}{\pi} \int_0^\omega \left\{ \frac{\ln R(\omega')}{\omega'^2 - \omega^2} + \frac{\ln R(2\omega - \omega')}{(2\omega - \omega')^2 - \omega^2} \right\} d\omega' - \frac{\omega}{\pi} \int_{2\omega}^\infty \frac{\ln R(\omega')}{\omega'^2 - \omega^2} d\omega'. \tag{B.14}$$

In this expression the integrand goes to zero as $\omega' \to \omega$ and the integral is easily evaluated by any standard integration algorithm.

Appendix C

Edge Shift within the Debye Model

In section 3.2 we found that in covalent semiconductors the shift of the band edge with respect to temperature scales like

$$E_g \propto |\mathcal{V}(\vec{K})|^2 \, e^{-<[\vec{K}\cdot\vec{u}]^2>}, \tag{C.1}$$

where $\mathcal{V}(\vec{K})$ is the Fourier component of the lattice-periodic potential $V(\vec{r})$, $\vec{K}$ the reciprocal-lattice vector and $<u^2>$ the mean square ionic displacement. By differentiating both sides with respect to temperature under constant volume we find

$$\frac{1}{E_g}\left(\frac{\delta E_g}{\delta T}\right)_V \propto K^2 \, \frac{\delta <u^2>}{\delta T}. \tag{C.2}$$

By using the Debye model to describe the density of states for the acoustical phonons, the only parameter influencing the temperature dependence of $<u^2>$ is the the Debye temperature, Θ_D. It is shown in [74] that in the Debye approximation, assuming one

atom per basis, the mean square lattice displacement can be expressed as

$$\frac{\delta < u^2 >}{\delta T} = \left(\frac{9\,h^2}{M\,k_B\,T^2} \right) \; F\left(\frac{\Theta_D}{T} \right) \tag{C.3}$$

where

$$F(x) = \frac{1}{x^2} \left(\frac{2}{x} \int_0^x \frac{y\,dy}{e^y - 1} \; - \; \frac{x}{e^x - 1} \right). \tag{C.4}$$

In section 3.2 we have numerically solved this differential equation for $\Theta_D = 400\,\mathrm{K}$ with the $F(x)$ prefactor and the overall scaling as fitting parameters as shown in Fig. 3-3. In the limit of $x \gg 1$, $F(x)$ scales like $1/x^3$ yielding $E_g(T) = E_g(0)(1 - \mathrm{Const}\,(T/\Theta_D)^2)$.

Bibliography

[1] J.G.Bednorz and K.A.Müller, Z.Phys.B **64**, 189 (1986)

[2] C.E.Gough *et al.*, Nature **326**, 855 (1987)

[3] For recent review on evidence for d-wave symmetry see Physics Today, May , 17 (1993)

[4] W.N.Hardy, D.A.Bonn, D.C.Morgan, R.Liang, K.Zhang, submitted to Phys.Rev.Lett.

[5] B.O.Wells, Z.X.Shen, D.S.Dessau, W.E.Spicer, D.B.Mitzi, L.Lombardo, A.Kapitulnik, A.J.Arko, Phys.Rev.B **46**, 11830 (1992)

[6] Z.X.Shen, D.S.Dessau, B.O.Wells, D.M.King, W.E.Spicer, A.J.Arko, D.Marshall, L.W.Lombardo, A.Kapitulnik, P.Dickinson, S.Doniach, J.DiCarlo, T.Loeser, C.H.Park, Phys.Rev.Lett. **70**, 1553 (1993)

[7] H.Takagi, B.Batlogg, H.L.Kao, J.Kwo, R.J.Cava, J.J.Krajewski, W.F.Peck,Jr, Phys.Rev.Lett. **69**, 2975 (1992)

[8] Z.Schlesinger, R.T.Collins, F.Holtzenberg, C.Field, S.H.Blanton, U.Welp, G.W.Crabtree, Y.Fang, J.Z.Liu, Phys.Rev.Lett. **65**, 801 (1990)

[9] S.L.Cooper, A.L.Kotz, M.A.Karlow, M.V.Klein, W.C.Lee, J.Giapintzakis, D.M.Ginsberg, Phys.Rev.B **45**, 2549 (1992)

[10] F.Gao, D.B.Romero, D.B.Tanner, J.Talvacchio, M.G.Forrester, Phys.Rev.B **47**, 1036 (1993)

[11] K.Tamasaku, Y.Nakamura, S.Uchida, Phys.Rev.Lett. **69**, 1455 (1992)

[12] H.Eskes *et al.*, Phys.Rev.B **41**, 288 (1990); J.F.Annett *et al.*, Phys.Rev.B **40**, 2620 (1989); A.K.McMahan *et al.*, Phys.Rev.B **38**, 6650 (1988)

[13] A.J.Freeman, J.Yu, C.L.Fu, Phys.Rev.B **36**, 7111 (1987)

[14] A.K.McMahan, R.M.Martin, S.Satpathy, Phys.Rev.B **38**, 6650 (1988)

[15] J.B.Grant, A.K.McMahan, Phys.Rev.Lett. **66**, 488 (1991); J.B.Grant, A.K.McMahan, Phys.Rev.B **46**, 8440 (1992);

[16] See for example A.Fujimori, E.Takayama-Muromachi, Y.Uchida, B.Okai., Phys.Rev.B **35**, 8814 (1987)

[17] G.Aeppli *et al.*, Phys.Rev.Lett. **62**, 2052 (1989); R.R.P.Singh *et al.*, Phys.Rev.Lett. **62**, 2736 (1989)

[18] For a review see E.Manousakis, Reviews of Modern Physics **63**, 1 (1991)

[19] N.W.Preyer, R.J.Birgeneau, C.Y.Chen, D.R.Gabbe, H.P.Jenssen, M.A.Kastner, P.J.Picone, T.Thio, Phys.Rev.B **39**, 11563 (1989)

[20] A.Levy, J.P.Falck, M.A.Kastner, R.J.Birgeneau, A.T.Fiory, A.F.Hebard, W.J.Gallagher, A.W.Kleinsasser, A.C.Anderson, Phys.Rev.B **46**, 520 (1992)

[21] C.Y.Chen *et al.*, unpublished

[22] C.Y.Chen, N.W.Preyer, P.J.Picone, M.A.Kastner, H.P.Jenssen, D.R.Gabbe, A.Cassanho, R.J.Birgeneau, Phys.Rev.Lett. **63**, 2307 (1989); C.Y.Chen, R.J.Birgeneau, M.A.Kastner, N.W.Preyer, T.Thio, Phys.Rev.B **43**, 392 (1991)

[23] N.W.Preyer, M.A.Kastner, C.Y.Chen, R.J.Birgeneau, Y.Hidaka, Phys.Rev.B **44**, 407 (1991)

[24] For a review on weak-localization see P.A.Lee, T.V.Ramakrishnan, Reviews of Modern Physics **57**, 287 (1985)

[25] C.T.Chen. L.H.Tjeng, J.Kwo, H.L.Kao, P.Rudolf, F.Sette, R.M.Flemming, Phys.Rev.Lett. **68**, 2543 (1992)

[26] D.M.King *et al.*, Phys.Rev.Lett. **70**, 3159 (1993)

[27] For a review see W.E.Pickett, H.Krakauer, R.E.Cohen, D.J.Singh, Science **255**, 46 (1992)

[28] B.Keimer, N.Belk, R.J.Birgeneau, A.Cassanho, C.Y.Chen, M.Greven, M.A.Kastner, A..Aharony, Y.Endoh, R.W.Erwin, G.Shirane, Phys.Rev.B **46**, 14034 (1992);

[29] T.Thurston, R.J.Birgeneau, M.A.Kastner, N.W.Preyer, G.Shirane, Y.Fujii, K.Yamada, Y.Endoh, K.Kakurai, M.Matsuda, Y.Hidaka, T.Murakami, Phys.Rev.B **40**, 4585 (1989)

[30] S.W.Cheong, G.Aeppli, T.E.Mason, H.Mook, S.M.Hayden, P.C.Canfield, Z.Fisk, K.N.Clausen, J.L.Martinez, Phys.Rev.Lett. **67**, 1791 (1991)

[31] F.C.Chou, F.Borsa, J.H.Cho, D.C.Johnston, D.R.Torgenson, J.Ziolo, submitted to Phys.Rev.Lett. (1993)

[32] T.Thio *et al.*, Phys.Rev.B **38**, 905 (1988)

[33] T.Moriya, Y.Takahashi, K.Ueda, J.Phys.Soc.Jpn. **59**, 2905 (1990)

[34] B.Keimer, R.J.Birgeneau, A.Cassanho, Y.Endoh, R.W.Erwin, M.A.Kastner, G.Shirane, Phys.Rev.Lett. **67**, 1930 (1991)

[35] S.Uchida, T.Ido, H.Takagi, T.Arima, Y.Tokura, S.Tajima, Phys.Rev.B **43**, 7942 (1991)

[36] M.Reedyk, T.Timusk, Phys.Rev.Lett. **69**, 2705 (1992)

[37] B.H. Toby, T.Egami, J.D.Jorgensen, M.A.Subramanian, Phys.Rev.Lett. **64**, 2414 (1990)

[38] H.Takagi, R.J.Cava, M.Marezio, B.Batlogg, J.J.Krajewski, W.F.Peck,Jr, P.Bordet, D.E.Cox, Phys.Rev.Lett. **68**, 3777 (1992)

[39] See for example V.J.Emery, G.Reiter, Phys.Rev.B **38**, 4547 (1988)

[40] N.Nücker, J.Fink, B.Renker, D.Ewert, C.Politis, P.J.W.Weijs, J.C.Fuggle, Z.Phys.B **67**, 9 (1987); N.Nücker, J.Fink, J.C.Fuggle, P.J.Durham, W.M.Temmerman, Phys.Rev.B **37**, 5158 (1988);

[41] J.A.Yarmoff, D.R.Clarke, W.Drube, U.O.Karlsson, A.Taleb-Ibrahimi, F.J.Himpsel, Phys.Rev.B **36**, 3967 (1987)

[42] J.M.Ginder, M.G.Roe, Y.Song, R.P.McCall, J.R.Gaines, E.Ehrenfreund, Phys.Rev.B **37**, 7506 (1988)

[43] Y.H.Kim, S-W.Cheong, Z.Fisk, Phys.Rev.Lett. **67**, 2227 (1991)

[44] J.Humliček,M.Garriga,M.Cardona, Solid State Comm. **67**, 589 (1988)

[45] T.Thio *et al.*, Phys.Rev.B **42**, 10800 (1990)

[46] J.P.Falck, A.Levy, M.A.Kastner, R.J.Birgeneau, Phys.Rev.Lett. **69**, 1109 (1992)

[47] G.A.Thomas *et al.*, Phys.Rev.B **45**, 2474 (1992); G.A.Thomas *et al.*, Phys.Rev.Lett. **67**, 2906 (1991)

[48] A.J.Millis, B.J.Shraiman, Phys.Rev.B **46** 14834 (1992)

[49] Y.H.Kim, A.J.Heeger, L.Acedo, G.Stucky, F.Wudl, Phys.Rev.B **36**, 7252 (1987)

[50] C.M.Foster, A.J.Heeger, G.Stucky, N.Herron, Solid State Comm. **71**, 945 (1989); C.M.Foster, A.J.Heeger, Y.H.Kim, G.Stucky, N.Herron, Synthetic Metals **33**, 171 (1989)

[51] J.P.Falck, A.Levy, M.A.Kastner, R.J.Birgeneau, Phys.Rev.B **47**, (1993)

[52] For a resent review see D.B.Tanner and T.Timusk in *Physical Properties of High Temperature Superconductors III*, edited by D. Ginsberg (World Scientific, Singapore 1992)

[53] S.L.Cooper, G.A.Thomas, J.Orenstein, D.H.Rapkine, A.J.Millis, S-W.Cheong, A.S.Cooper, Z.Fisk, Phys.Rev.B **41**, 11605 (1990)

[54] J.D.Perkins, J.M.Graybeal, M.A.Kastner, R.J.Birgeneau, J.P.Falck, M.Greven, submitted to Phys.Rev.Lett. (1993)

[55] J.P.Falck, J.D.Perkins, A.Levy, M.A.Kastner, J.M.Graybeal, R.J.Birgeneau, submitted to Phys.Rev.B (1993)

[56] A.Virosztek, J.Ruvalds, Phys.Rev.B **42**, 4046 (1990); J.Ruvalds, A.Virosztek, Phys.Rev.B **43**, 5498 (1991)

[57] C.M.Varma, P.B.Littlewood, S.Schmitt-Rink, E.Abrahams, A.Ruckenstein, Phys.Rev.Lett. **63**, 1996 (1989); *ibid*, **64**, 497 (1990)

[58] P. J. Picone, H. P. Jensen, D. R. Gabbe, J. Cryst Growth **85**, 576 (1987)

[59] D.C.Johnston, S.K.Sinha, A.J.Jacobson, J.M.Newsam, Physica C **153-155**, 572 (1988); private communication

[60] A.Levy, M.J.Lercel, J.P.Falck, M.A.Kastner, A.A.Bright, A.W.Kleinsasser, J.Appl.Phys. **71**, 1764 (1992)

[61] For a review see M.Cardona *Modulation Spectroscopy*, Solid State Physics, Suppl. II (Academic, New York, 1969)

[62] B.Esser, Phys.stat.sol. (b) **51**, 735 (1972)

[63] J.Orenstein *et al.*, in "Novel Superconductivity" eds,. S.A.Wolf, V.Z.Dresin, (Plenum,New York,1987), p.693; S.Tajima *et al.*, J.Opt.Soc.Am. B **6**, 475 (1989); S.L.Cooper *et al.*, Phys.Rev.B **42** (1990)

[64] B.Velický, J.Sak, Phys.stat.sol. **16**, 147 (1966)

[65] R.J.Elliott, Phys.Rev. **108**, 1384 (1957)

[66] F.Lederman, J.D.Dow, Phys.Rev.B **13**, 1633 (1976)

[67] J.Hermanson, Phys.Rev. **166**, 893 (1968)

[68] P.Y.Yu, M.Cardona, Phys.Rev.B **2**, 3193 (1970)

[69] R.M.Candea, C.M.Gee, S.J.Hudgens, M.Kastner, Phys.Rev.B **16**, 2657 (1977)

[70] R.P.Feynman, Phys.Rev. **97**, 660 (1955)

[71] J.Appel, "Polarons", Solid State Physics **21**, 193-391 (Academic, New York, 1968)

[72] H.Y.Fan, Phys.Rev. **82**, 900 (1951)

[73] H.Fröhlich, H.Pelzer, S.Zienau, Phil.Mag. **41**, 221 (1950)

[74] J.M.Ziman, *Principles of the Theory of Solides* (Cambridge University, Cambridge, England, 1965)

[75] S.J.Collocott *et al.*, Phys.Rev.B **36**, 5684 (1987)

[76] R.E.Cohen, W.E.Pickett, H.Krakauer, L.L.Boyer, Physica B&C **150** (1988)

[77] L.Pintschovius, N.Pyka, W.Reichardt, A.Yu.Rumiantsev, N.L.Mitrofanov, A.S.Ivanov, G.Collin, P.Bourges, Physica B **174**, 323 (1991)

[78] E.T.Heyen, J.Kircher, M.Cardona, Phys.Rev.B **45**, 3037 (1992)

[79] I.Ohana, D.Heiman, M.S.Dresselhaus, P.J.Picone, Phys.Rev.B **40**, 2225 (1989)

[80] H.J.Ye, R.P.McCall, W.E.Farneth, E.M.McCarron III, A.J.Epstein, Phys.Rev.B **43**, 10574 (1991)

[81] M.Ueta, H.Kanzaki, K.Kobayashi, Y.Toyozawa, E.Hanamura, *Excitonic Processes in Solids*, (Springer, New York 1986)

[82] D.Emin, T.Holstein, Phys.Rev.Lett. **36**, 323 (1976)

[83] J.Bourgoin and M.Lannoo,*Point Defect in Semiconductors*, (Springer, New York 1983)

[84] H.Bethe, Handbuch der Physik, **24/1**, Ziff 47, (Julius Spriger, Berlin 1933)

[85] A.O.Gogolin, A.S.Ioselevich, JETP Lett. **51**, 532 (1990)

[86] A.H.Wilson, *The Theory of Metals*, (Cambridge University Press, Cambridge 1958)

[87] O.Madelung, *Introduction to Solid-State Theory*, (Springe-Verlag, Berlin 1981)

[88] D.M.Eagles, Solid State Comm. **76**, 715 (1990)

[89] V.J.Emery, S.A.Kivelson, H.Q.Lin, Phys.Rev.Lett. **64**, 475 (1990)

[90] V.J.Emery, S.A.Kivelson, Physica C **209**, 597 (1993)

[91] J.H.Cho, F.C.Chou, D.C.Johnston, Phys.Rev.Lett. **70**, 222 (1993)

[92] Y.H.Kim, S-W.Cheong, Z.Fisk, Submitted to Phys.Rev.Lett. (1993)

[93] D.Mihailović, C.M.Foster, K.F.Voss, T.Mertelj, I.Poberaj, N.Herron, Phys.Rev.B **44**, 237 (1991)

[94] H.Krakauer, W.E.Pickett, R.E.Cohen, Phys.Rev.B **47**, 1002 (1993)

[95] Y.Tanabe, T.Moriya, S.Sugano, Phys. Rev. Lett. **15**, 1023 (1965)

[96] J.D.Perkins, private communication (1993)

[97] A.Levy, J.P.Falck, M.A.Kastner, W.J.Gallagher, A. Gaupta, A.W.Kleinsasser, J.Appl.Phys. **69**, 4439 (1991)

[98] F.Mila, Phys.Rev.B **38**, 11358 (1988)

[99] B.Esser, Phys.stat.scl. (b) **51**, 735 (1972)

[100] R.Liu, D.Salamon, M.V.Klein, S.L.Cooper, W.C.Lee, S.W.Cheong, D.M.Ginsberg, Submitted to Phys.Rev.Lett.

[101] See for example K.B.Lyons *et al.*, Phys.Rev.B **39**, 9693 (1989)

[102] H.P.Geserich *et al.*, Europhys. Lett. **6**, 277 (1988)